REPORT DOCUMENTATION PAGE	Form Approved OMB NO. 0704-0188

1. REPORT DATE (DD-MM-YYYY)	2. REPORT TYPE	3. DATES COVERED (From - To)
05-12-2013	Final Report	1-Oct-2009 - 3-Sep-2013

4. TITLE AND SUBTITLE
Manufacturing Science of Improved Molded Optics - Final Report

5a. CONTRACT NUMBER
W911NF-09-1-0536

5b. GRANT NUMBER

5c. PROGRAM ELEMENT NUMBER
106011

6. AUTHORS
Paul F. Joseph, Kathleen C. Richardson, Igor Luzinov, Vincent Blouin

5d. PROJECT NUMBER

5e. TASK NUMBER

5f. WORK UNIT NUMBER

7. PERFORMING ORGANIZATION NAMES AND ADDRESSES
Clemson University
Office of Sponsored Programs
300 Brackett Hall, Box 345702
Clemson, SC   29634 -5702

8. PERFORMING ORGANIZATION REPORT NUMBER

9. SPONSORING/MONITORING AGENCY NAME(S) AND ADDRESS (ES)
U.S. Army Research Office
P.O. Box 12211
Research Triangle Park, NC 27709-2211

10. SPONSOR/MONITOR'S ACRONYM(S)
ARO

11. SPONSOR/MONITOR'S REPORT NUMBER(S)
56858-MS-DPS.36

12. DISTRIBUTION AVAILIBILITY STATEMENT
Approved for Public Release; Distribution Unlimited

14. ABSTRACT
Computational mechanics and glass science have been applied to the study of precision glass molding (PGM). Early in the study a coupled thermo-mechanical finite element model was rigorously validated and then used in a detailed sensitivity analysis to identify important material and process behaviors. This experience led to a detailed investigation to characterize friction and determine viscosity in the important range of $10^{7.5} - 10^9$ Pa•s. Viscosity is the primary behavior that allows shape change in glass forming processes and as such must be characterized very accurately. Furthermore, in the viscosity range of interest friction complicates approaches used

15. SUBJECT TERMS
Precision Glass Molding, Friction, Structural Relaxation, Stress Relaxation, Surface Coating

16. SECURITY CLASSIFICATION OF:			17. LIMITATION OF ABSTRACT	15. NUMBER OF PAGES	19a. NAME OF RESPONSIBLE PERSON
a. REPORT	b. ABSTRACT	c. THIS PAGE	UU		Paul Joseph
UU	UU	UU			19b. TELEPHONE NUMBER
					864-656-0545

Report Title

Manufacturing Science of Improved Molded Optics - Final Report

ABSTRACT

Computational mechanics and glass science have been applied to the study of precision glass molding (PGM). Early in the study a coupled thermo-mechancial finite element model was rigorously validated and then used in a detailed sensitivity analysis to identify important material and process behaviors. This experience led to a detailed investigation to characterize friction and determine viscosity in the important range of $10^{7.5} – 10^9$ Pa•s. Viscosity is the primary behavior that allows shape change in glass forming processes and as such must be characterized very accurately. Furthermore, in the viscosity range of interest friction complicates approaches used to obtain viscosity such as parallel plate viscometry. In addition stress relaxation was identified as a very difficult behavior to characterize and a special no-slip glass specimen was designed to obtain it. The most important behavior revealed in the sensitivity analysis was structural relaxation, the characterization of which was a focus in the last year of the project. In addition extensive work was done developing analytical processes to evaluate mold tooling-glass material interaction tendencies in PGM. This provides the "know-how" needed in both research and development to successfully refine the PGM process through both computational mechanics and glass science.

Enter List of papers submitted or published that acknowledge ARO support from the start of the project to the date of this printing. List the papers, including journal references, in the following categories:

(a) Papers published in peer-reviewed journals (N/A for none)

Received   Paper

12/05/2013 28.00   Balajee Ananthasayanam, Paul F. Joseph, Dhananjay Joshi, Scott Gaylord, Laeticia Petit, Vincent Y. Blouin, Kathleen C. Richardson, Daniel L. Cler, Matthew Stairiker, Matthew Tardiff. Final Shape of Precision Molded Optics: Part I—Computational Approach, Material Definitions and the Effect of Lens Shape,
Journal of Thermal Stresses, (06 2012): 0. doi: 10.1080/01495739.2012.674830

12/05/2013 29.00   Dhananjay Joshi, Paul F. Joseph, Scott Gaylord, Laeticia Petit, Vincent Y. Blouin, Kathleen C. Richardson, Daniel L. Cler, Matthew Stairiker, Matthew Tardiff, Balajee Ananthasayanam. Final Shape of Precision Molded Optics: Part II—Validation and Sensitivity to Material Properties and Process Parameters,
Journal of Thermal Stresses, (07 2012): 0. doi: 10.1080/01495739.2012.674838

12/05/2013 30.00   Dhananjay Joshi, Peiman Mosaddegh, J. David Musgraves, Kathleen C. Richardson, Paul F. Joseph. Thermo-mechanical characterization of glass at high temperature using the cylinder compression test. Part I: Viscoelasticity, friction, and PPV,
Journal of Rheology, (08 2013): 0. doi: 10.1122/1.4817434

12/05/2013 31.00   Dhananjay Joshi, Peiman Mosaddegh, J. David Musgraves, Kathleen C. Richardson, Paul F. Joseph. Thermo-mechanical characterization of glass at high temperature using the cylinder compression test. Part II: No-slip experiments, viscoelastic constants, and sensitivity,
Journal of Rheology, (08 2013): 0. doi: 10.1122/1.4817435

12/05/2013 32.00   Peter Wachtel, Peiman Mosaddegh, Benn Gleason, J. David Musgraves, Kathleen Richardson. Performance Evaluation of a Bench-Top Precision Glass Molding Machine,
Advances in Mechanical Engineering, (04 2013): 0. doi: 10.1155/2013/178680

12/05/2013 33.00   Erick Koontz, Vincent Blouin, Peter Wachtel, Kathleen Richardson, J. David Musgraves. Prony Series Spectra of Structural Relaxation in N-BK7 for Finite Element Modeling,
The Journal of Physical Chemistry A, (12 2012): 0. doi: 10.1021/jp307717q

12/05/2013 34.00   Balajee Ananthasayanam, Dhananjay Joshi, Matthew Stairiker, Matthew Tardiff, Kathleen C. Richardson, Paul F. Joseph. High temperature friction characterization for viscoelastic glasscontacting a mold,
Journal of Non-Crystalline Solids, (01 2014): 100. doi:

TOTAL: **7**

Number of Papers published in peer-reviewed journals:

(b) Papers published in non-peer-reviewed journals (N/A for none)

<u>Received</u>   <u>Paper</u>

12/05/2013 35.00 Benn Gleason, Peter Wachtel, J. David Musgraves, Kathleen Richardson. Using design of experiments to
improve precisionglass moulding,
Int. J. Experimental Design and Process Optimisation, (06 2013): 263. doi:

   TOTAL: **1**

Number of Papers published in non peer-reviewed journals:

(c) Presentations

E. Koontz, P. Wachtel, J. David Musgraves, K. Richardson, "Characterization of structural relaxation in As2Se3 for analysis of lens shape change in glass press mold cooling and post-process annealing", SPIE Optifab 2013 Conference, Rochester, NY October 14-17 2013.

E. Koontz, P. Wachtel, J. David Musgraves, K. Richardson, S. Mourad, M. Huber, A. Kunz, M. Forrer, "Interaction of N-FK5 and L-BAL35 optical glass with various carbide and other precision glass mold tooling", SPIE Optifab 2013 Conference, Rochester, NY October 14-17 2013.

S. Danto, E. Koontz, Y. Zou, T. Ogbuu, B. Gleason, Peter Wachtela,b, J. D. Musgraves, J. Hu, K. Richardson, "Nanoscale optical features via hot-stamping of As2Se3 glass", SPIE Optifab 2013 Conference, Rochester, NY October 14-17 2013.

Number of Presentations: 3.00

Non Peer-Reviewed Conference Proceeding publications (other than abstracts):

<u>Received</u>   <u>Paper</u>

12/04/2013 25.00 E. Koontz, P. Wachtel, J. David Musgraves, K. Richardson, S. Mourad, M. Huber, A. Kunz, M. Forrer.
Interaction of N-FK5 and L-BAL35 optical glass with various carbide and other precision glass mold
tooling,
SPIE Optifab 2013 Conference. 14-OCT-13, . : ,

12/04/2013 24.00 Peter Wachtel, Erick Koontz, J. David Musgraves, Kathleen Richardson. Characterization of structural
relaxation in As2Se3 for analysis of lens shape change in glass press mold cooling and post-process
annealing,
SPIE Optifab 2013 Conference. 14-OCT-13, . : ,

   TOTAL: **2**

Number of Non Peer-Reviewed Conference Proceeding publications (other than abstracts):

Peer-Reviewed Conference Proceeding publications (other than abstracts):

<u>Received</u>   <u>Paper</u>

TOTAL:

Number of Peer-Reviewed Conference Proceeding publications (other than abstracts):

(d) Manuscripts

Received   Paper

02/04/2013 18.00   Dhananjay Joshi, Peiman Mosaddegh, J. David Musgraves, Kathleen Richardson, Paul Joseph. Thermo-Mechanical Characterization of Glass at High Temperature Using the Cylinder Compression Test: Part I – Viscoelasticity, Friction and PPV,
Journal of Rheology (01 2013)

02/04/2013 19.00   Dhananjay Joshi, Peiman Mosaddegh, J. David Musgraves, Kathleen Richardson, Paul Joseph. Thermo-Mechanical Characterization of Glass at High Temperature Using the Cylinder Compression Test: Part II – No-Slip Experiments, Viscoelastic Constants and Sensitivity,
Journal of Rheology (01 2013)

06/14/2012   9.00   Balajee Ananthasayanam, Paul F. Joseph, Dhananjay Joshi, Scott Gaylord, Laeticia Petit, Vincent Y. Blouin, Kathleen C. Richardson, Daniel L. Cler, Matthew Stairiker, Matthew Tardiff. Final Shape of Precision Molded Optics: PartI—Computational Approach, Material Definitions andthe Effect of Lens Shape,
Journal of Thermal Stresses (04 2011)

06/15/2012 10.00   Balajee Ananthasayanam, Paul F. Joseph, Dhananjay Joshi, Scott Gaylord, Laeticia Petit, Vincent Y. Blouin, Kathleen C. Richardson, Daniel L. Cler, Matthew Stairiker, Matthew Tardiff. FINAL SHAPE OF PRECISION MOLDED OPTICS: PART II—VALIDATION ANDSENSITIVITY TO MATERIAL PROPERTIES AND PROCESS PARAMETERS,
Journal of Thermal Stresses (04 2011)

07/19/2013 20.00   Balajee Ananthasayanam, Dhananjay Joshi, Matthew Stairiker, Matthew Tardiff, Kathleen C. Richardson, Paul F. Joseph. High Temperature Friction Characterization for Viscoelastic Glass Contacting a Mold,
International Journal of Engineering Science (07 2013)

08/31/2012 13.00   Dhananjay Joshi, Matthew Stairiker, Matthew Tardiff, kathleen Richardson, Paul Joseph, Balajee Ananthasayanam. Friction characterization at a glass-mold interface using the ring compression test,
Journal of Materials Processing Technology (08 2012)

08/31/2012 17.00   Peter Wachtel, Peiman Mosaddegh, Benn Gleason, J. David Musgraves, Kathleen Richardson. PERFORMANCE EVALUATION OF A BENCH-TOP PRECISION GLASS MOLDING MACHINE,
Precision Engineering (08 2012)

08/31/2012 16.00   Peter Watchel, J. David Musgraves, Benn Gleason, Kathleen Richardson. UsingDesignofExperimentstoImprovePrecisionGlassMolding,
Precision Engineering (07 2012)

08/31/2012 14.00   Erick Koontz, Vincent Blouin, Peter Wachtel, J. David Musgraves, Kathleen Richardson. Prony series spectra of structural relaxation in N-BK7 for finite element modeling,
Journal of Physical Chemistry (08 2012)

09/09/2011   8.00   Christopher Ostrouchov, Peiman Mosaddeg, John Ziegert, J. David Musgraves, Paul Joseph, Dhananjay Joshi, Peter Wachtel, Kathleen Richardson. A Combined Numerical and Experimental Approach to Measuring Gap Conductance for Precision Glass Molding,
Journal for Undergraduate Materials Research (09 2011)

12/03/2013 21.00   Balajee Ananthasayanama, Dhananjay Joshi, Matthew Stairiker, Matthew Tardiff, Kathleen C. Richardson, Paul F. Joseph. High temperature friction characterization for viscoelastic glasscontacting a mold,
Journal of Non-Crystalline Solids (09 2013)

12/03/2013 22.00 Dhananjay Joshi, Paul F. Joseph. Parallel Plate Viscometry for Glass at High Viscosity,
Journal of the American Ceramic Society (09 2013)

12/04/2013 23.00 Peter Wachtel, J. David Musgraves, Kathleen Richardson, Benn Gleason. Using design of experiments to
improve precisionglass moulding,
Int. J. Experimental Design and Process Optimisation (08 2012)

12/04/2013 26.00 Peiman Mosaddegh, Benn Gleason, J. DavidMusgraves, PeterWachtel, Kathleen Richardson.
Performance Evaluation of a Bench-Top PrecisionGlass Molding Machine,
Advances in Mechanical Engineering (08 2012)

12/04/2013 27.00 Erick Koontz, Vincent Blouin, Peter Wachtel, J. David Musgraves, Kathleen Richardson. Prony Series
Spectra of Structural Relaxation in N?BK7 for FiniteElement Modeling,
Journal of Physical Chemistry A (08 2012)

TOTAL: **15**

Number of Manuscripts:

Books

Received   Paper

TOTAL:

Patents Submitted

Patents Awarded

Awards

None

Graduate Students

NAME	PERCENT_SUPPORTED	Discipline
Mohamed Trabelssi	1.00	
Dhananjay Joshi	1.00	
Erick Koontz	1.00	
FTE Equivalent:	**3.00**	
Total Number:	**3**	

Names of Post Doctorates

NAME	PERCENT_SUPPORTED
FTE Equivalent:	
Total Number:	

Names of Faculty Supported

NAME	PERCENT_SUPPORTED	National Academy Member
Paul F. Joseph	0.17	
FTE Equivalent:	**0.17**	
Total Number:	**1**	

Names of Under Graduate students supported

NAME	PERCENT_SUPPORTED
FTE Equivalent:	
Total Number:	

Student Metrics
This section only applies to graduating undergraduates supported by this agreement in this reporting period

The number of undergraduates funded by this agreement who graduated during this period: 0.00

The number of undergraduates funded by this agreement who graduated during this period with a degree in science, mathematics, engineering, or technology fields:...... 0.00

The number of undergraduates funded by your agreement who graduated during this period and will continue to pursue a graduate or Ph.D. degree in science, mathematics, engineering, or technology fields:...... 0.00

Number of graduating undergraduates who achieved a 3.5 GPA to 4.0 (4.0 max scale):...... 0.00

Number of graduating undergraduates funded by a DoD funded Center of Excellence grant for Education, Research and Engineering:...... 0.00

The number of undergraduates funded by your agreement who graduated during this period and intend to work for the Department of Defense 0.00

The number of undergraduates funded by your agreement who graduated during this period and will receive scholarships or fellowships for further studies in science, mathematics, engineering or technology fields:...... 0.00

Names of Personnel receiving masters degrees

NAME
Total Number:

Names of personnel receiving PHDs

NAME
Total Number:

Names of other research staff

NAME	PERCENT_SUPPORTED
FTE Equivalent:	
Total Number:	

Sub Contractors (DD882)

Inventions (DD882)

Scientific Progress

Scientific progress and accomplishments

Details of scientific progress and accomplishments are provided in the journal papers published (see next page) and in Appendices A-D. The most important findings and/or accomplishments are listed below.

•	Publication of a combined validation and sensitivity study for the simulation of the final size and shape of a molded lens. This set of two journal papers covers in great detail the effects of material and process parameters on the final molded lens.

•	Completion of a combined experimental and computational procedure to determine the viscosity and viscoelastic behavior of a molding glass within the molding temperature range, which has resulted in three journal papers in the last year. A key development was the ability to have a cylindrical glass specimen stick to two surfaces.

•	The experimental procedure to form a uniform carbon coating on the objects of complex geometry (like glass preforms) was developed. Carbon coatings prepared from polycarbonate have been successfully applied to glass samples. Polycarbonate was tested as a protective coating for chalcogenide glass and was shown to successfully prevent direct glass-mold contact. Because of soft/fluid nature of polycarbonate at the temperatures of molding no cracking issue was observed. Thus, polycarbonate and polycarbonate derived carbon materials can cover wide range of glasses used in molding process. See Appendix D for a paper draft.

•	Completion of the baseline characterization of the GP5000-HT benchtop PGM press was made. A Design of Experiments (DOE) approach based on the Taguchi method was employed to create a set of experiments that determine the impact of process parameters such as temperature (viscosity), heating rate, pressing force and cooling rate on the accuracy and repeatability of the Precision Glass Molding (PGM) process. Such capability enables the identification of the most significant process parameters and their effects on the post-molded part. A journal paper was published.

•	A procedure to precisely obtain a prony series was developed and is described in a journal paper that applies the procedure to structural relaxation.

•	A procedure to determine friction at the glass/mold interface was described in a journal paper published at the end of the project. This paper thoroughly demonstrates that the (ring compression test) procedure is independent of the material properties of glass, which allows an experimentalist to apply the method without the need for computational mechanics. Two other papers on this topic will soon be submitted (see Appendix C for paper drafts).

Journal papers

C. Ostrouchov, P. Mosaddegh, J. Ziegert, D. Musgraves, P. Joseph, D. Joshi, P. Wachtel, K. Richardson, "A combined numerical and experimental approach to measuring gap conductance for precision glass molding," Materials Science and Technology Conference and Exhibition 2011, MS and T'11, v 2, pp. 1729-1736, 2011.

B. Ananthasayanam, P.F. Joseph, D. Joshi, S. Gaylord, L. Petit, V.Y. Blouin, K.C. Richardson, D.L. Cler, M. Stairiker, M. Tardiff, "Final shape of precision molded optics: Part I – Computational approach, material definition and the effect of lens shape" J. Thermal Stresses 35, pp. 550-578, 2012.

B. Ananthasayanam, P.F. Joseph, D. Joshi, S. Gaylord, L. Petit, V.Y. Blouin, K.C. Richardson, D.L. Cler, M. Stairiker, M. Tardiff, "Final shape of precision molded optics: Part II – Validation and sensitivity to material properties and process parameters," J. Thermal Stresses 35, pp. 614-636, 2012.

E. Koontz, V. Blouin, P. Wachtel, J. D. Musgraves, K. Richardson, "Prony Series Spectra of Structural Relaxation in N-BK7 for Finite Element Modeling," Journal of Physical Chemistry A, 116, pp. 12198-12205, 2012.

B. Gleason, P. Wachtel, J.D. Musgraves, K. Richardson, "Using design of experiments to improve precision glass molding," International Journal of Experimental Design and Process Optimisation (IJEDPO), 3, pp. 263-275, 2013.

P. Wachtel, P. Mosaddegh, B. Gleason, J.D. Musgraves, K. Richardson, "Performance evaluation of a bench-top precision glass molding machine," Advances in Mechanical Engineering, 2013, Article ID 178680, 12 pages, 2013.

D. Joshi, P. Mosaddegh, J. D. Musgraves, K. C. Richardson, P. F. Joseph, "Thermo-Mechanical Characterization of Glass at High Temperature Using the Cylinder Compression Test: Part I –Viscoelasticity, Friction and PPV," J. Rheol., 57 1367-1389, 2013.

D. Joshi, P. Mosaddegh, J. D. Musgraves, K. C. Richardson, P. F. Joseph, "Thermo-Mechanical Characterization of Glass at High Temperature Using the Cylinder Compression Test: Part II – No-Slip Experiments, Viscoelastic Constants and Sensitivity," J. Rheol., 57, 1391-1410, 2013.

B. Ananthasayanam, D. Joshi, M. Stairiker, M. Tardiff, K.C. Richardson, P. F. Joseph, "High Temperature Friction Characterization for Viscoelastic Glass Contacting a Mold," J. Non-Cryst. Solids, 385, 100-110, 2014.

D. Joshi and P.F. Joseph, "Parallel Plate Viscometry for Glass at High Viscosity," to appear, Journal of the American Ceramic Society.

Technology Transfer

Scientific progress and accomplishments

Details of scientific progress and accomplishments are provided in the journal papers published (see next page) and in Appendices A-D. The most important findings and/or accomplishments are listed below.

- Publication of a combined validation and sensitivity study for the simulation of the final size and shape of a molded lens. This set of two journal papers covers in great detail the effects of material and process parameters on the final molded lens.

- Completion of a combined experimental and computational procedure to determine the viscosity *and viscoelastic behavior* of a molding glass within the molding temperature range, which has resulted in three journal papers in the last year. A key development was the ability to have a cylindrical glass specimen stick to two surfaces.

- The experimental procedure to form a uniform carbon coating on the objects of complex geometry (like glass preforms) was developed. Carbon coatings prepared from polycarbonate have been successfully applied to glass samples. Polycarbonate was tested as a protective coating for chalcogenide glass and was shown to successfully prevent direct glass-mold contact. Because of soft/fluid nature of polycarbonate at the temperatures of molding no cracking issue was observed. Thus, polycarbonate and polycarbonate derived carbon materials can cover wide range of glasses used in molding process. See Appendix D for a paper draft.

- Completion of the baseline characterization of the GP5000-HT benchtop PGM press was made. A Design of Experiments (DOE) approach based on the Taguchi method was employed to create a set of experiments that determine the impact of process parameters such as temperature (viscosity), heating rate, pressing force and cooling rate on the accuracy and repeatability of the Precision Glass Molding (PGM) process. Such capability enables the identification of the most significant process parameters and their effects on the post-molded part. A journal paper was published.

- A procedure to precisely obtain a prony series was developed and is described in a journal paper that applies the procedure to structural relaxation.

- A procedure to determine friction at the glass/mold interface was described in a journal paper published at the end of the project. This paper thoroughly demonstrates that the (ring compression test) procedure is independent of the material properties of glass, which allows an experimentalist to apply the method without the need for computational mechanics. Two other papers on this topic will soon be submitted (see Appendix C for paper drafts).

Journal papers

C. Ostrouchov, P. Mosaddegh, J. Ziegert, D. Musgraves, P. Joseph, D. Joshi, P. Wachtel, K. Richardson, "A combined numerical and experimental approach to measuring gap conductance for precision glass molding," *Materials Science and Technology Conference and Exhibition 2011,* MS and T'11, v 2, pp. 1729-1736, 2011.

B. Ananthasayanam, P.F. Joseph, D. Joshi, S. Gaylord, L. Petit, V.Y. Blouin, K.C. Richardson, D.L. Cler, M. Stairiker, M. Tardiff, "Final shape of precision molded optics: Part I – Computational approach, material definition and the effect of lens shape" *J. Thermal Stresses* 35, pp. 550-578, 2012.

B. Ananthasayanam, P.F. Joseph, D. Joshi, S. Gaylord, L. Petit, V.Y. Blouin, K.C. Richardson, D.L. Cler, M. Stairiker, M. Tardiff, "Final shape of precision molded optics: Part II – Validation and sensitivity to material properties and process parameters," *J. Thermal Stresses* 35, pp. 614-636, 2012.

E. Koontz, V. Blouin, P. Wachtel, J. D. Musgraves, K. Richardson, "Prony Series Spectra of Structural Relaxation in N-BK7 for Finite Element Modeling," *Journal of Physical Chemistry A,* 116, pp. 12198-12205, 2012.

B. Gleason, P. Wachtel, J.D. Musgraves, K. Richardson, "Using design of experiments to improve precision glass molding," *International Journal of Experimental Design and Process Optimisation (IJEDPO),* 3, pp. 263-275, 2013.

P. Wachtel, P. Mosaddegh, B. Gleason, J.D. Musgraves, K. Richardson, "Performance evaluation of a bench-top precision glass molding machine," *Advances in Mechanical Engineering,* 2013, Article ID 178680, 12 pages, 2013.

D. Joshi, P. Mosaddegh, J. D. Musgraves, K. C. Richardson, P. F. Joseph, "Thermo-Mechanical Characterization of Glass at High Temperature Using the Cylinder Compression Test: Part I –Viscoelasticity, Friction and PPV," *J. Rheol.,* 57 1367-1389, 2013.

D. Joshi, P. Mosaddegh, J. D. Musgraves, K. C. Richardson, P. F. Joseph, "Thermo-Mechanical Characterization of Glass at High Temperature Using the Cylinder Compression Test: Part II – No-Slip Experiments, Viscoelastic Constants and Sensitivity," *J. Rheol.,* 57, 1391-1410, 2013.

B. Ananthasayanam, D. Joshi, M. Stairiker, M. Tardiff, K.C. Richardson, P. F. Joseph, "High Temperature Friction Characterization for Viscoelastic Glass Contacting a Mold," *J. Non-Cryst. Solids*, 385, 100-110, 2014.

D. Joshi and P.F. Joseph, "Parallel Plate Viscometry for Glass at High Viscosity," to appear, *Journal of the American Ceramic Society*.

Table of Contents

Appendix A. Materials development and interaction studies: workpiece and mold materials.
Erick Koontz and Kathleen Richardson

Structural relaxation in glasses is a topic of much study in glass science [1-3]. Relaxations occur in almost all hot forming processes either intentionally or unintentionally. For example when a bulk glass is cast from a molten melt, it is typically annealed afterwards to relieve stresses from quenching and from extreme structural disequilibrium. This annealing is achieved through intended structural relaxation. In the case of precision glass molding (PGM) structural relaxation can occur during cooling or subsequent annealing. In the case of a lens this shape change will alter the optical properties of intended optic and can cause difficulty in achieving the necessary optical tolerances. For this reason GPCL has been studying glass relaxation behavior extensively. The initial work with oxide glasses, transitioning into Infrared (IR) glasses targets research tasks (A.1, A.3, a spin off B.2, and aspects of C.2).

Structural relaxation measurements

Structural relaxation measurements have classically been done using (Differential Scanning Calorimetry) DSC experiments tracking and characterizing enthalpy relaxations [3]. Tool, Narayanaswamy, and Moynihan did extensive work in this area. However, for the specific application of PGM, it was decided to characterize the structural relaxation using length dilatometry. A comparison of relaxation characterized using length dilatometry and relaxation characterized using DSC showed significant differences in overall behavior. Due to the fact that the crux of the PGM structural question is directly related to volume change, the characterization of that relaxation using the direct method of length dilatometry was chosen as the path to follow.

The measurements were carried out on a thermo mechanical analyzer (TMA). The ~ 3mm x 3mm cross section samples range in height from 10 -25 mm. These samples are placed in the TMA as seen in Figure 1.
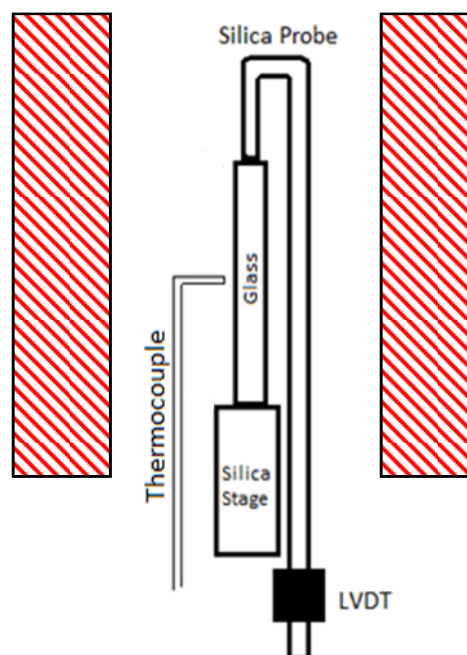

Figure 1: TMA schematic

The samples were heated from room temperature at a moderate rate (typically 5 °C/min) to ~ 10 °C above the glass transition temperature (T_g). This was done to reset the thermal history of the glass, this step occurs before every measurement. Structural equilibrium, or the condition in which all structural relaxation had ceased was defined by the linearity of change in length vs. temperature curve. Once the samples had reached structural equilibrium at the reset temperature, they were dropped to the initial test temperature at 1 °C/min. After holding at this temperature until structural relaxation ceased, the temperature was decreased some ΔT, which was varied throughout the study. The resulting change in length due to this temperature change is the data that is of interest in this study. Full explanations of the operations touched on here can be found in the paper we published on this topic [4]. The specific study was done on N-BK7, a Schott oxide, optical glass. However, the method is the same, excepting temperature, as the non-oxide section of the study.

An unprocessed change in length vs. time curve is represented by the black curve in Figure 2. There are coefficient of thermal expansion (CTE) effects that have to be removed from the beginning of the relaxation because they are instantaneous and not part of the time dependent structural relaxation that we aimed to characterize. The other aspect of data processing is the removal of the constant linear portion at the end of the relaxation. This is due to viscous contraction as the glass very slowly "slumps" under its own weight. Once these effects were removed, we were left with the red curve seen in Figure 2.

These experiments were carried out for ΔTs from 5 °C to 20 °C for temperatures ranging from above to more than 40 °C below T_g. This tested a wide range of temperatures and behaviors spanning the transition region in the glasses tested. A plot of the relaxation versus temperature behavior for N-BK7 glass can be seen in Figure 3. The latest glass to be characterized was As_2Se_3, a paper on that work is currently being written.
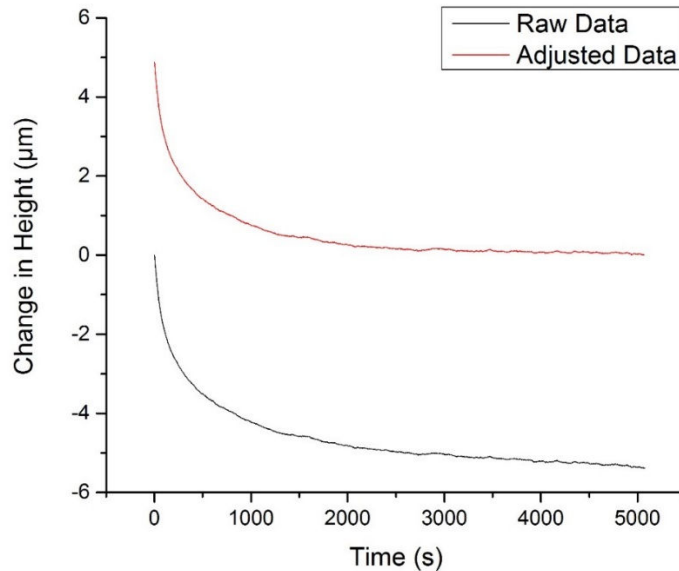

Figure 2: Change in length (μm) versus time (s) typical plot of relaxation, processed and unprocessed cures
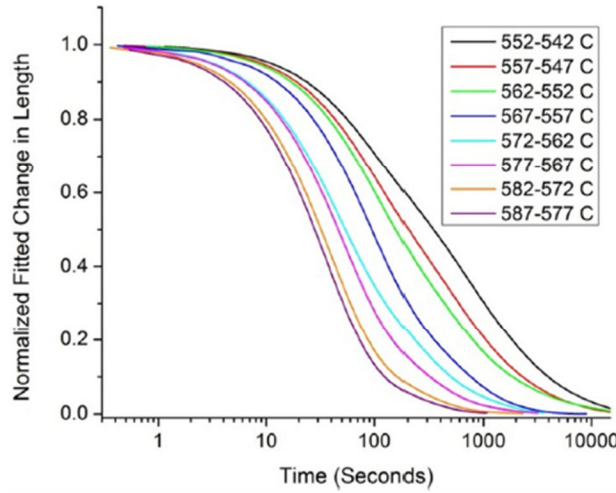
Figure 3: Relaxation change in length versus seconds on a log scale for N-BK7 oxide glass

Structural relaxation modeling

Following the measurement of structural relaxation using length dilatometry, the curve fitting of the various experiments commenced. There are a number of general functions used for describing relaxation behaviors in materials. Almost all of them are based on some sort of exponential. Often the word decay is used to describe the same phenomenon. From dielectric relaxation to stress and structural relaxation the most common element in any model is the exponential function. In the case of glass in the transition region, the relaxation behavior is indeed exponential, however it is not strictly so.

In glass science literature up to this point there are two main functions used to describe glass relaxations, whether those be dilatometric or enthalpic or otherwise. The first, used by Phillips in his Diffusion Trap Theory [5] and Mauro in his modeling of structural relaxations [6] is the stretched exponential in Equation 1.

$$\phi(t) = exp[(-t/\tau)^{\beta}]$$ **Equation 1**

This function is also referred to as the Kohlrausch-Williams-Watts function (KWW), it uses the exponential β to modify the shape of the base exponential function. If $\beta=1$, the exponential is a pure exponential, if $\beta>1$ the exponential is considered a "compressed" exponential, and the typical case for material relaxations, if $\beta<1$ the exponential is known as "stretched". This function in conjunction with the TNM equation is used to characterize enthalpic structural relaxation [7].

The other function typically seen in relaxation modeling of glass is a function known as a Prony series. The Prony series is a series of weighted exponential which can approximate a stretched exponential. The form of the Prony series is

$$\delta(t) = \sum_{i=1}^{N} w_i * e^{\left(\frac{-t}{\tau_i}\right)}$$ **Equation 2**

Aside from being used as a solver-friendly alternative to the KWW function, Prony series are the mathematical solution to the Generalized Maxwell Equation which is widely used in stress relaxation and creep modeling in glasses. After some initial research it was determined that the stretched exponential function did not model the experimental data that was collected. The Prony series, however, proved adept at modeling the experimental data collected as described above.

The method for fitting the experimental curves with a Prony series representation is fairly straightforward. After processing the data to isolate only the configurational component, the data is input to a custom tailored Matlab fitting routine. The method used here is not strictly new, although this is the first time it has been used in this context [8]. The general method is to input a vector of τ_i values into the solver as constants and allow the solver to return which of those τ values are weighted significantly non-zero. The result of this fitting is a "relaxation spectrum" that consists of a number of peaks, an example can be seen in Figure 4. There are various parameters with which to optimize the solving process, varying the τ step-size, for instance, changes the resolution of your spectra. A typical step size is 5 s.
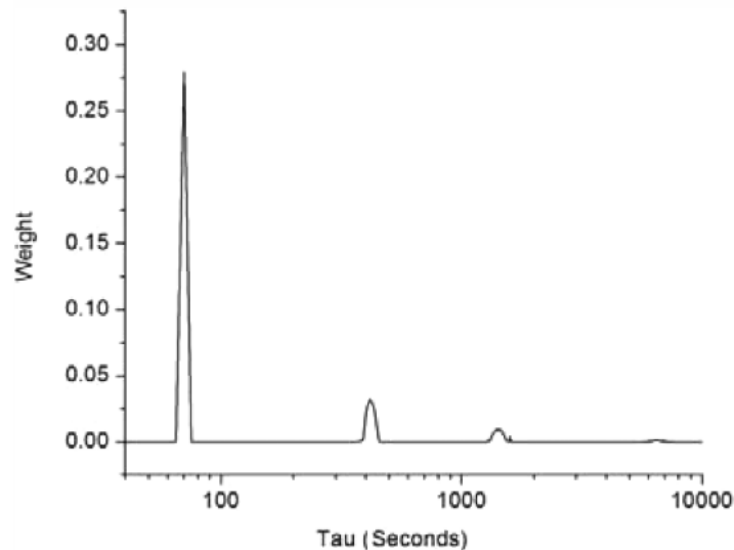

Figure 4: Prony series spectrum of structural relaxation from 552 to 542 °C in N-BK7

In the case of N-BK7, the relaxation spectra at low temperature show a set of four distinct distributions of significantly weighted relaxation times. As the temperature of the relaxations is increased, the number of peaks diminishes. The most helpful way to plot the overall relaxation behavior of N-BK7 is to plot the w_i term versus temperature. It turns out that the tau values do not vary significantly in this oxide glass, however the weight trends versus temperature are well defined and able to be mathematically explained for future use in modeling. The nearly linear trends are shown in Figure 5.
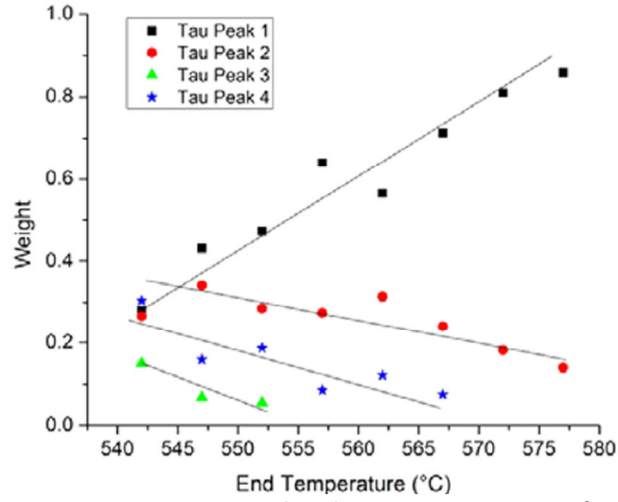
7

Figure 5: Prony series weight values versus temperature for N-BK7 relaxations from 542-577 °C

The linear trends are easily quantified mathematically and detailed in Table 1. These values can be input into a Prony series, simply modifying the weights with a temperature dependence. This allows the change in height to be characterized across the entire measurement range. This is a precursor to finite element modeling (FEM) of the relaxation in this system.

Table 1: Weight versus temperature trends for relaxation spectra of N-BK7

Table 3. Weight Linear Fit Parameters

	slope (m)	intercept (b)	R^2
peak 1	0.0157	−8.1739	0.94
peak 2	−0.0042	2.6196	0.6
peak 3	−0.0084	4.826	0.85
peak 4	−0.0095	5.29	0.85

Applying the change in height equation to the linear weight trends allows us to complete Equation 3. This gives a first approximation of relaxation behavior over the entire range of temperature measured.

$$\frac{dh}{h_i} = \sum_{4}^{i=1} (m_i T + b_i)\exp^{[-t/\tau_i]}$$

Equation 3

The relaxation behavior for arsenic selenide glass is markedly different than that of the oxide. The most notable difference is the evolution of peak weight over temperature. In the case of N-BK7, which has a T_g of 557 °C, the peaks decay as the temperature increases. However, the 2nd peak does not fully decay until well above T_g. It is anticipated that there will be a single exponential relaxation at high temperatures in glasses. According to a corresponding plot in Figure 6, $As_{40}Se_{60}$ also has four relaxation modes at lower temperatures. The number of relaxation modes decreases as the temperature increases towards T_g. In contrast to the oxide glass, the number of modes are reduced to a single exponential before T_g (196 °C for $As_{40}Se_{60}$).
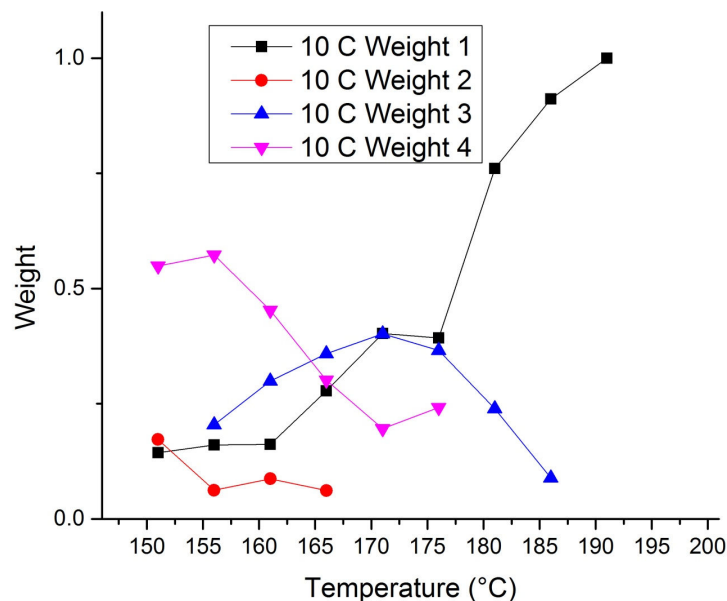
Figure 6: Weight versus temperature of $As_{40}Se_{60}$ for a temperature jump of 10 °C

The other stark difference between the chalcogenide and oxide glass is the shape of the weight versus temperature curve, the trend seen in the oxide glass was linear but the trend in this particular non-oxide glass is anything but linear. The longer time peaks (higher number peaks) show a near exponential decay towards dissolution.

These experiments and subsequent modeling allow us to characterize structural relaxation in a glass over a given temperature range of interest. Further study is now looking into the identification of these peaks and association of them with specific structures in glasses. The characterization of relaxation behavior as a function of composition in the arsenic-selenium-germanium system is ongoing and is parallel to the studies seeking to identify the structures in the glass that correspond to the observed relaxation features.

Precision Glass Molding (Mold-Oxide Glass Interaction)

In addition to a heavily glass science based approach with regards to structural relaxation in both oxides and chalcogenides, GPCL has been active in technological development towards the goal of refined precision glass molding as well. The following study involved molding and analysis of two commercially available oxide glasses. The goal was to mold these two glasses (L-BAL35 and N-FK5) using different mold tool materials and study the interactions on a chemical and mechanical level. The following pages detail the initial characterization of the glasses as well as the molding and post-mold analysis.

Viscosity characterization
Viscosity in glasses can be measured using several different instruments and methods. In order to characterize the viscosity of glasses to be molded, GPCL standard procedure is to use a Beam

Bending Viscometer (BBV) for the viscosities near T_g and Parallel Plate Viscometer (PPV) for viscosities that are much lower than those at T_g (higher temperature). Molding viscosities are typically considered to be 6.5-9.0 log (Pa*s) although the range can vary. The BBV is most accurate when used to measure viscosities between 10 and 13 log (Pa*s) while the PPV is most accurate in the 3-6 log (Pa*s) range. Seeing as none of these instruments directly overlaps the molding region it is necessary to interpolate, the measurement process as well as this interpolation is detailed in this section.

The BBV utilizes a 3 mm square cross-section glass beam that is ~55 mm long. A silica hook is suspended on the beam so that a hanging mass may be added at the appropriate time. This can be seen in Figure 7.
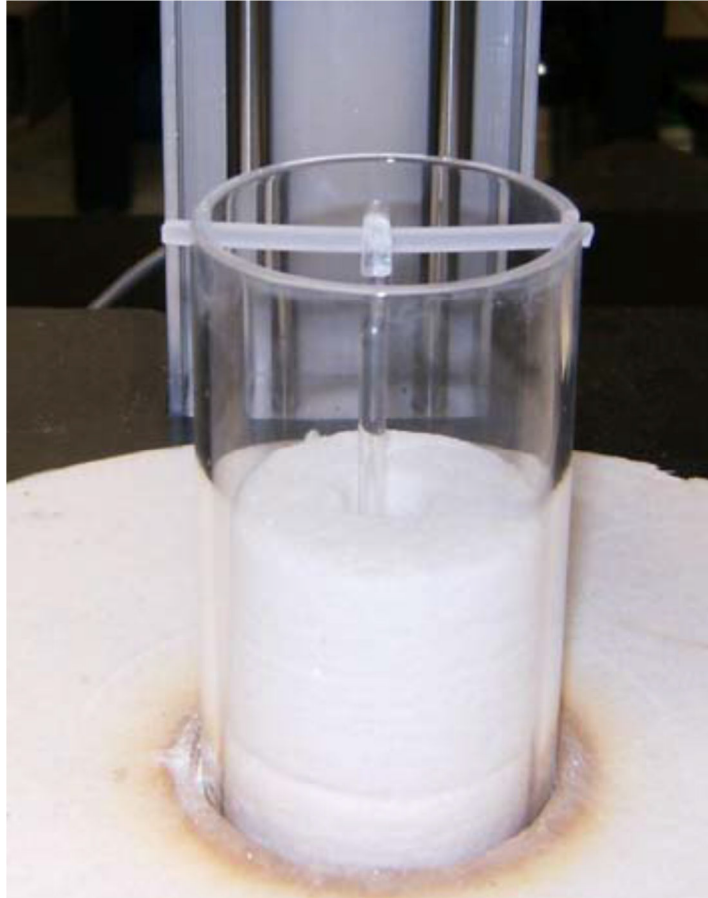

Figure 7: BBV experimental setup

The sample is heated via an enclosed furnace to a set of 2 or 3 temperatures just above and below T_g and the isothermal deflection rate of the beam under a given hanging mass is measured. The standard equation (Equation 4) for calculating the viscosity from measured BBV data is

Equation 4

$$\eta = \frac{g * L^3}{1440 I_c * \left(\frac{dh}{dt}\right)} * \left(M + \frac{\rho AL}{1.6}\right)$$

where L is the sample length, A is the cross-sectional area, ρ is the density, M is the applied mass, g is the gravitational constant, I_c is the moment of inertia and $\frac{dh}{dt}$ is the deflection rate. This operation is done for 2-3 temperatures and viscosities around T_g to obtain the high viscosity end of the curve.

The PPV utilized a 5 mm high by 10 mm diameter glass cylinder polished at both ends to measure viscosity. The cylinder is placed between 2 Inconel plates with a specific mass on top weighting down the sample. The instrument is then ramped from room temperature to the max temperature which is typically defined as the temperature at which the glass has achieved a predetermined percent reduction in height. An example of the setup can be seen in Figure 8.
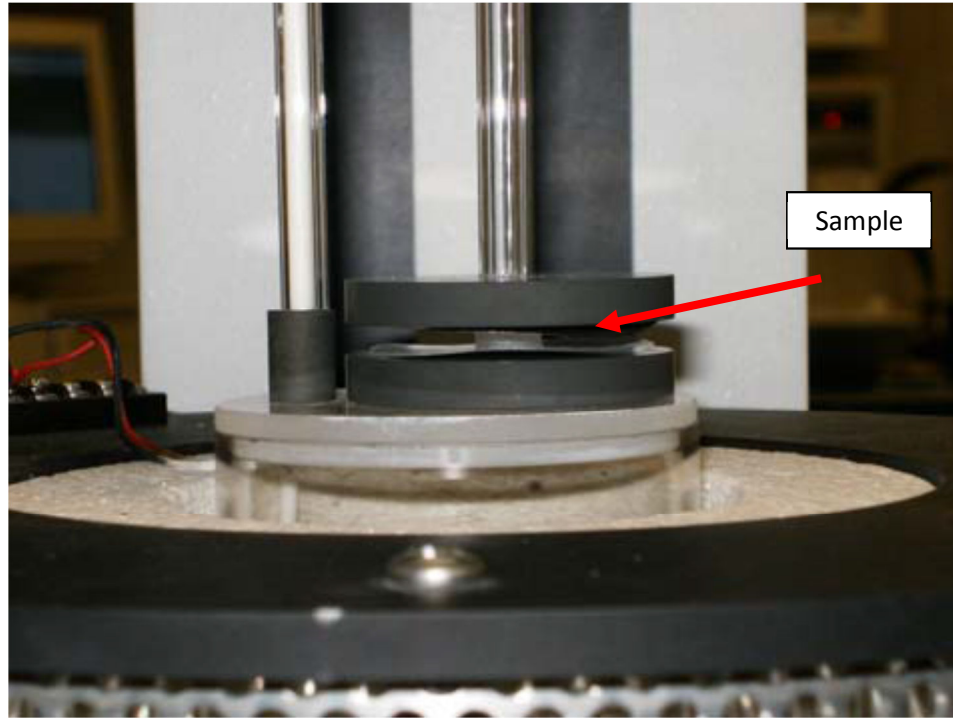

Figure 8: PPV experimental setup

The viscosity calculation using PPV data is carried out in much the same way as the BBV.

Equation 5

$$\eta = 2\pi \frac{M * g * h^5}{30V \left(\frac{dh}{dt}\right)(2\pi h^3 + V)}$$

In Equation 5 *M* is the applied mass, *h* is the original height, *V* is the glass volume; the rest of the parameters are the same as Equation 4. Whereas the BBV produced 2 or 3 high viscosity data points, the PPV produces a large number of data points in a lower viscosity range.

In order to create the full curve from the viscosity data gathered the Vogel-Fulcher-Tammann (VFT) equation is applied to the experimental data. The VFT equation is

Equation 6

$$\log(\eta) = A + \frac{B}{T - T_0}$$

where η is the viscosity, *A*, *B*, and T_0 are constant fitting parameters and *T* is the temperature. The data was input into Origin and the data points were fitted for both N-FK5 and L-BAL35. The data points as well as the resulting VFT fit is shown in Figure 9. The VFT parameters are shown in Table 2. From Figure 9 it is evident that N-FK5 has a shallower viscosity curve than L-BAL35 which should make it easier to control from a viscosity/temperature standpoint during molding.

Table 2: VFT parameters for N-FK5 and L-BAL35

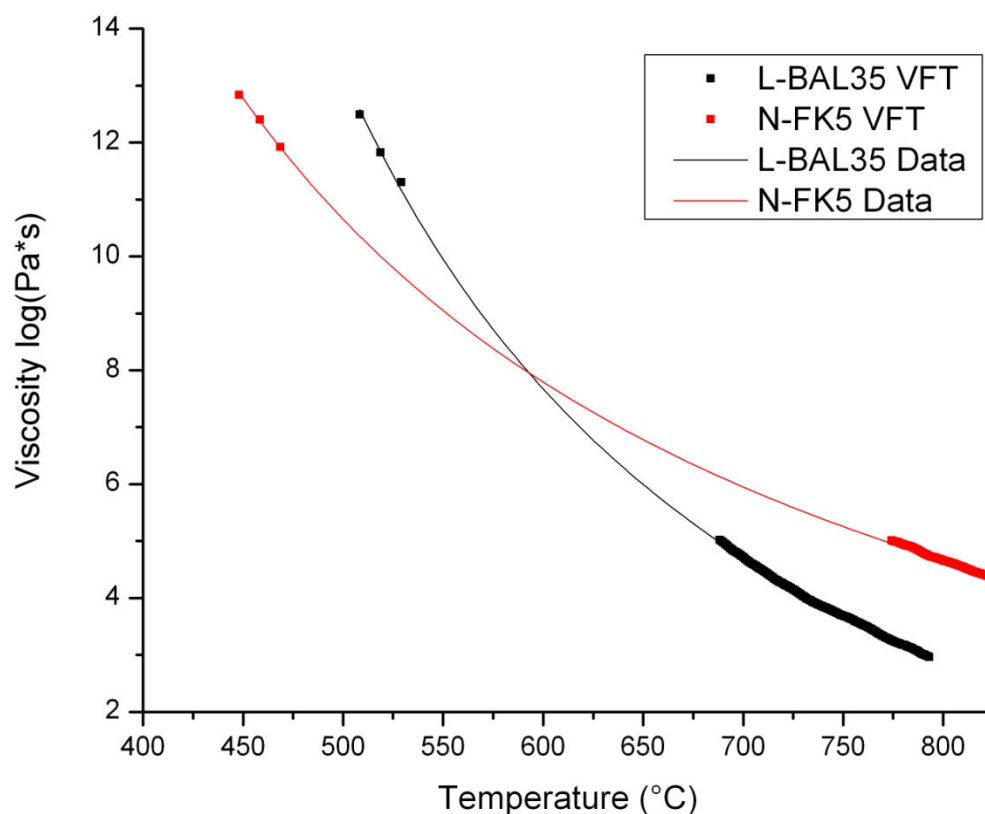|	L-BAL35	N-FK5
A	-5.113	-2.528
B	4227	4753
T_0 (°C)	269.4	139.4

Figure 9: N-FK5 and L-BAL35 viscosity curves

Weight loss and decomposition

Before carrying out the remaining thermal analysis it is necessary to define an upper working temperature for the glasses in question. To do this a thermo-gravimetric analyzer (TGA) was used. The TGA heats the glass sample at a given ramp rate while constantly sampling the mass of the sample. When the mass of the glass remaining is <99% of the initial mass the test is stopped and the temperature at which the target was reached can be termed the 1% weight loss temperature. Weight loss measurements were made for both L-BAL35 and N-FK5 ramping at 10 °C/min to 1200 °C. A weight loss value was not found for L-BAL35 because it did not lose weight by the 1200°C instrument limit, N-FK5 was found to have a 1% at loss at (1060 ± 10) °C. There is no reason to believe that either of these weight loss temperatures will hamper the study in anyway, those temperatures are far above any reasonably expected use temperature.

Glass transition, crystallization, and melting temperatures

The key thermal properties are determined using a Differential Scanning Calorimeter (DSC) and Differential Thermal Analyzer (DTA). The DSC upper temperature is considered to be ~600 °C

while the DTA upper temperature is between ~1200 °C. Therefore it was expected that T_g would be able to be determined by DSC while the peak crystallization temperature (T_x) would be determined by DTA.

Annealed glass samples were ground into a powder and sealed in aluminum pans in the DSC with a ramp rate of 10 °C/min. The temperature range of the DSC turned out to be just high enough to capture the T_g of both glasses as was expected. The resulting heat flow versus temperature graphs can be seen in Figure 10. Similarly processed glass powder was run in the DTA to assess the T_x of the glasses. The standard ramp rate of 10 °C/min was used. L-BAL35 was run up to 1200 °C in platinum pans without any sign of crystallization while N-FK5, due to its upper operating temperature of ~ 1060 °C, was limited to 1000 °C. Neither glass showed signs of crystallization or proper melting features up to these temperatures. It is important to note that T_g can be determined in one of three ways. The onset, inflection point, and offset methods. It was chosen to record both the onset and inflection T_g values since they are the most accepted.

Coefficient of thermal expansion and dilatometric softening point

The next round of thermal evaluations was done using a Thermo-Mechanic Analyzer (TMA). A TMA uses a silica glass probe to measure the mechanical expansion behavior of a material when subjected to changes in temperature. In this study 3mm square cross section samples of ~ 25 mm in height were placed vertically in the instrument and ramped at 10 °C/min to their final temperatures. Most materials, including the glasses in question, have a region in which they behave like a solid and expand more or less linearly in that temperature space. It is this linear region that is used to compute the Coefficient of Thermal Expansion (CTE). Figure 11 shows one of the TMA plots in question. The slope of the linear region is taken and that is applied in Equation 7

Equation 7

$$\alpha_g = \frac{1}{L_i}\left(\frac{\Delta L}{\Delta T}\right)$$

where α_g is the CTE of the glass, L_i is the initial length or height of the sample, ΔL is the change in sample length or height, and ΔT is the change in temperature. Three runs were done on each glass and the average CTE was calculated. In industry there is no set convention as to the ranges of temperature in which the CTE is measured. For this study the CTE was calculated in the 100-300 °C range which is most common, the 100 °C-Tg range which is most useful, as well as the > T_g range which is known as the liquid expansion.
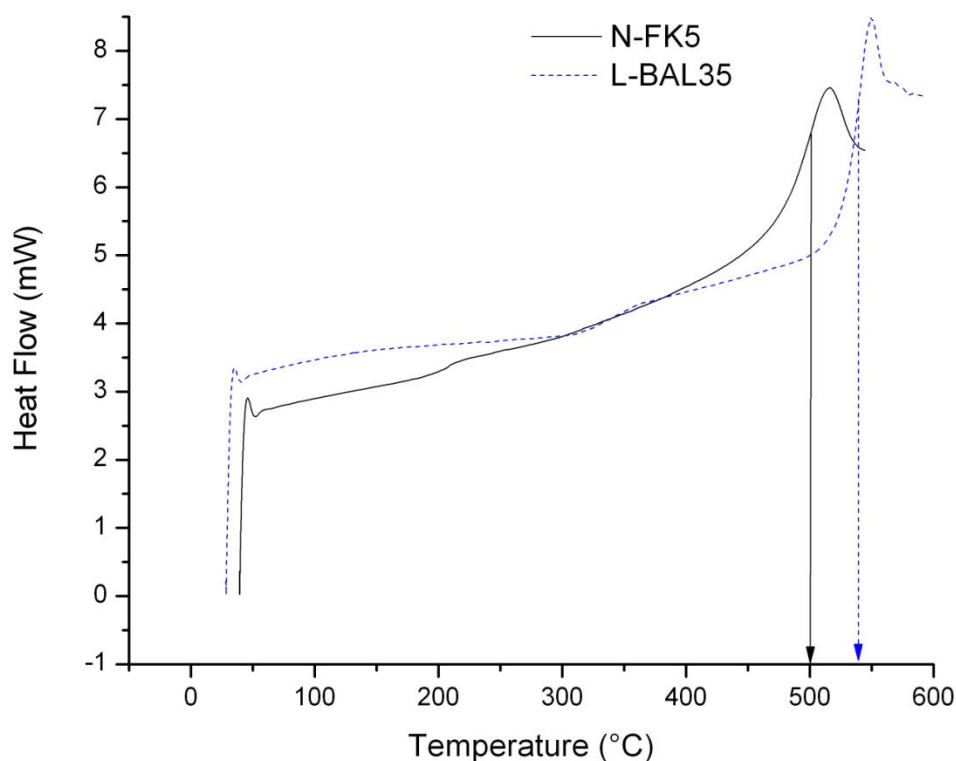
Figure 10: DSC curve of heat flow versus temperature for N-FK5 and L-BAL35

Another important thermo-mechanical property that was determined by TMA was the dilatometric softening point (T_D). This characterizes the temperature at which the glass begins to "deform under its own weight" consequently this is a useful value as far as molding is concerned because it gives a starting point for glass deformation. T_D is simply defined as the temperature at which the curves in Figure 11 reach a maximum and begin to drop. As it turns out the viscosity curves of L-BAL35 and N-FK5 intersect in the molding region and both their T_D values are between 570 and 575 °C.
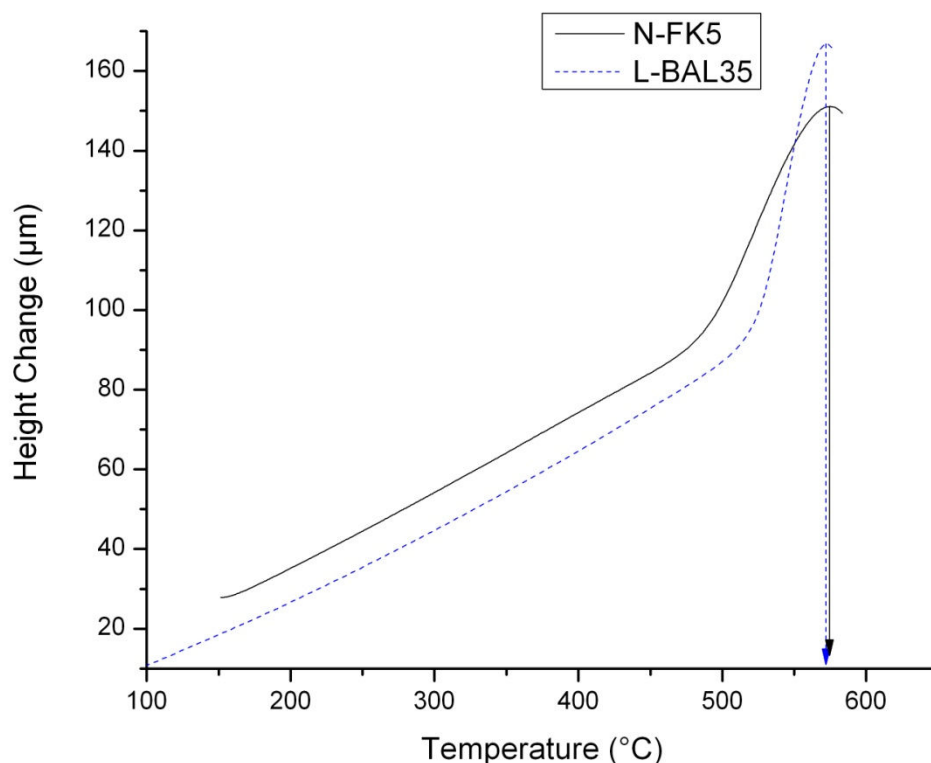
Figure 11: TMA plot of height change versus temperature for N-FK5 and L-BAL35

Chemical analysis

The final phase of initial characterization in module 1 was the determination of chemical constituents in the glasses. This was done using Energy Dispersive X-ray Spectroscopy (EDS). A TM-3000 Hitachi Scanning Electron Microscope (SEM) with an on-board EDS was used for this characterization. The instrument was calibrated with a copper standard. N-FK5 and L-BAL35 glass samples were cleaned with acetone and ethanol, then placed on the SEM pedestal using double sided carbon tape and the exposed surface was cleaned again with ethanol. The pedestal height was adjusted to ensure optimum EDS accuracy and the sample holder was placed in the instrument and vacuumed down. Several EDS measurements were taken, typically 3 groups of 3 spectra. Note that in the L-BAL35 raw data sodium and chlorine are shown to be present but they are believed to be contamination from human touch and were disregarded as components of the glass.

The raw data was inferred into composition data using known stoichiometric compounds. As an example, if silicon and oxygen are present in a material, then it was assumed that they are present in the form of SiO_2. Using that reasoning it is possible to assess the chemical makeup of the glass. This was done on the data from L-BAL35 and N-FK5 and the results of that process are listed in Table 3. The data shows that N-FK5 is heavily fluorinated while L-BAL35 has a larger number of constituents.

Table 3: Calculated glass compositions of L-BAL35 and N-FK5

Composition		
	Measured	
	L-BAL35	N-FK5
SiO_2 (At.%) ± 1	70.95	61.50
CaO (At.%) ± 1	10.13	-
Al_2O_3 (At.%) ± 1	1.84	-
ZnO (At.%) ± 1	4.27	-
SrO (At.%) ± 1	12.81	-
K_2O (At.%) ± 1	-	11.07
F (At.%) ± 1	-	27.43

Module 3: Raw mold tooling material

Module 3 contains the pressing of raw WC and coated SiC, this is the experimental bulk of the study. It was decided that a 2^x method would be a meaningful way to gather data as a snapshot of the degradation behavior. For that reason, the following procedure was carried out on each mold and sample after press 0 (pre-pressing) and after presses 1, 2, 4, and 8. The characterization instruments and pressing procedures will be described in detail below and then the results will be explained and discussed.

Characterization and pressing protocols

White light interferometry

The first analysis done on both glass and mold inserts was the measuring of surface roughness using a Zygo White light interferometer. With the exception of the N-FK5 pressed with raw WC test a stitch method was used to characterize the roughness of each mold inserts before and after each press. Glass roughness was measured pre-pressing for a number of samples to establish a constant accepted pre-mold roughness and then roughness was measured after each relevant press. Due to the stitching method used the Root-Mean-Square (RMS) roughness is the best number with which to judge the evolution of mold roughness. The Peak-to-Valley (PV) roughness values are warped by the drop-off at the edges of the inserts. Roughness values measured by interferometry were not understood to be strictly accurate roughness values, although they are consistent in this study they are best judged in a qualitative rather than quantitative light.

Scanning electron microscopy

A Hitachi TM-3000 SEM was used to view the surface of the inserts and samples. These images were valuable in "visually" determining the extent of the degradation and understanding some of the degradation mechanisms that contributed to a reduction in mold insert lifetimes. Each area of interest, either of interest due to a specific feature notices or of interest as a matter of procedure, was imaged at ~ 40x zoom and then at 2500x zoom to obtain a complete picture of the feature. These images will be of use in the coming sections

Energy dispersive x-ray spectroscopy

An EDS, which was an integrated feature of the Hitachi TM-3000 SEM, was used to characterize the chemical makeup on the surface of mold inserts and glass pieces. Similar to the SEM, certain areas were targeted due to visibly interesting features and some were targeted as a matter of procedure. The EDS returns atomic % values for chemicals detected at the surface. Note, an EDS does not calculate compositions or compounds, only elemental species. The EDS was calibrated using a copper standard before each set of tests, consisting of no more than 4 hours between calibrations. The error was considered to be ±2%. Data obtained by EDS was used to show progressive oxidation of mold surfaces and transfer of chemical species from glass to mold and vice versa.

Molding protocol

This section details the molding protocol used in all of these studies:
- Glass and inserts cleaned with acetone then isopropyl alcohol before and after each press and measurement
- The odd numbered insert of each pair was the top insert and even numbered was the bottom
- Force controlled pressing
- Ultra-High Purity (UHP) Nitrogen atmosphere throughout entire process
- Effective soaking and pressing temperature 576-592 °C
- Soak force 100 N
- Press force 500 N
- Final end temperature 240 °C
- Cooling rate from press temperature .45 °C/min.
- Target thickness .6-.9 mm

Raw WC with N-FK5

The first mold-glass combination that was studied was N-FK5 pressed with raw WC. The format of this section and those to follow will be step-wise. The properties obtained through the analysis described above will be presented at the crucial junctures, aka before molding then after molds 1, 2, 4, and 8.

Note for the pressing of N-FK5 with raw WC stitch Zygo images were not taken for any except the final press (#8) so 5x magnification single shots will be used to inform the reader of surface

roughness values. Also a high quality camera was available only for the N-FK5 with raw WC study, therefore the stitched Zygo images will be used to show "visual" surface qualities on all but this first pressing survey. After the first examples of mold insert SEM images, only the bottom mold insert will be shown to conserve space. The bottom insert always showed degradation equal to or greater than the top mold insert. The effective average molding temperature as calculated by using the PPV in Equation 5 and VFT in Equation 6 was 576 °C, full table in the appendix
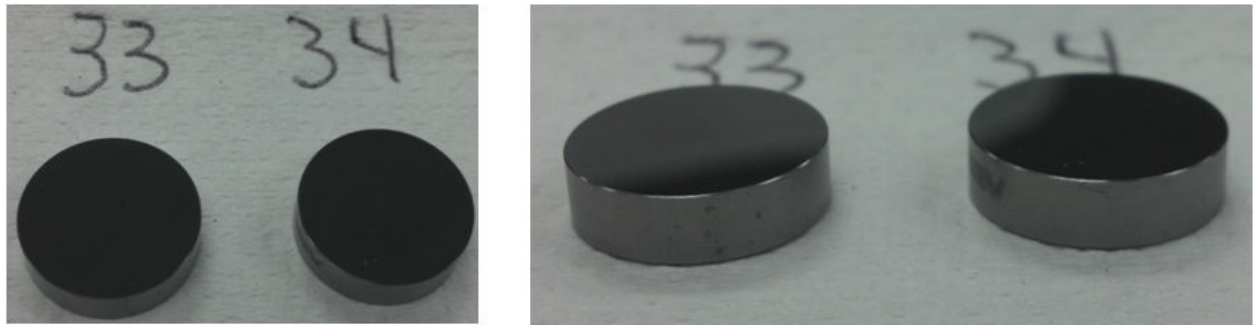
Molds after press 0

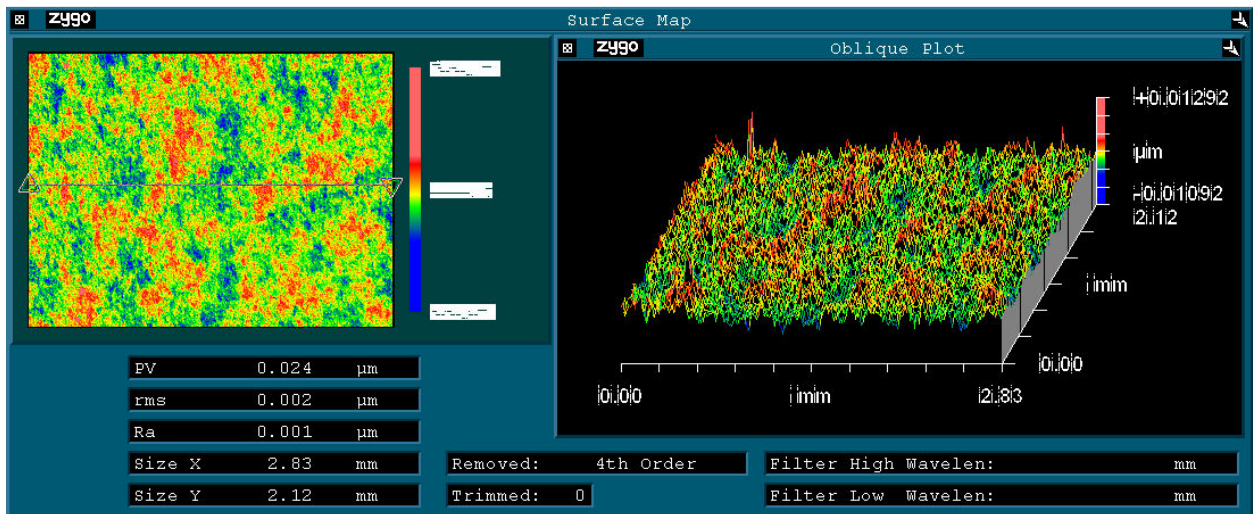Figure 12: Pictures of WC_33 and WC_34 before pressing
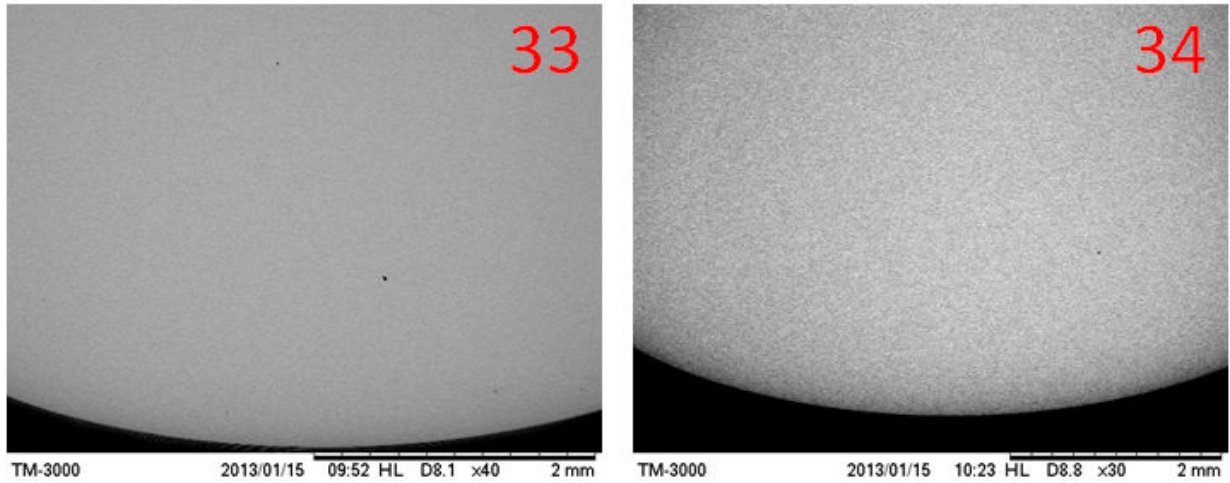

Figure 13: WC_34 Zygo after press 0

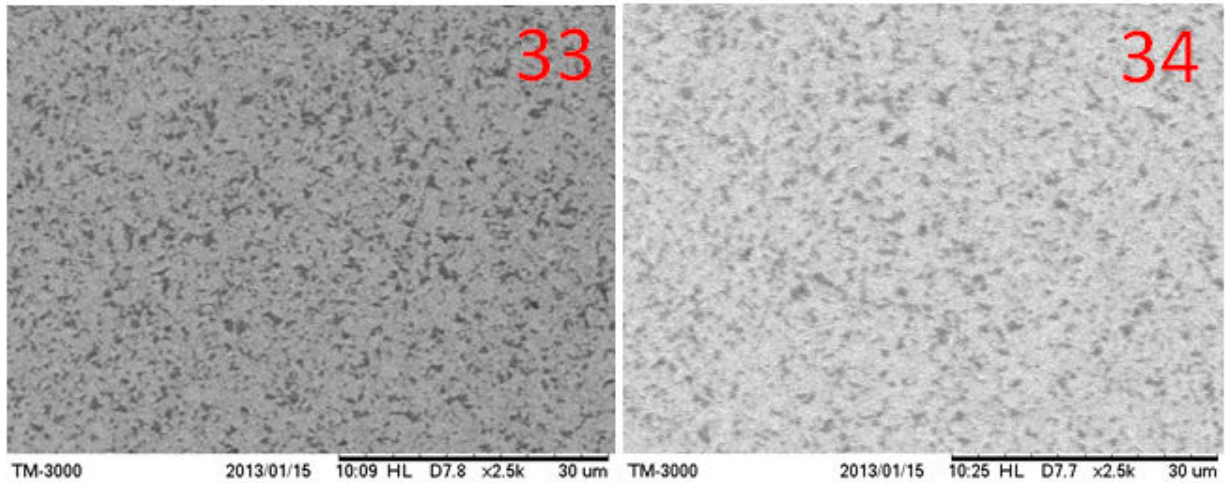**Figure 14: SEM WC_33 and WC_34 zoomed out before pressing**

Figure 15: SEM WC_33 and WC_34 zoomed in before pressing

Table 4: EDS WC_33 and WC_34 before pressing

WC_33 Measured in Center			
Element	Weight %	Weight % σ	Atomic %
Carbon	8.187	0.67633333	55.7563333
Titanium	2.67233333	0.215	4.567
Tungsten	89.1403333	0.68766667	39.6766667

WC_34 Measured in Center			
Element	Weight %	Weight % σ	Atomic %
Carbon	8.04333333	0.36966667	55.356
Titanium	2.55066667	0.118	4.403
Tungsten	89.406	0.37633333	40.2406667

The figures presented here show the comprehensive scale of analysis done on each mold insert. The raw WC inserts have a good, low surface roughness (Figure 13). One

20

thing to note, the roughness displayed in Figure 13 is lower than the roughness seen in the following studies. This is because the roughness for this study is a result of a spot measurement while the following studies all refer to roughness of a stitched or composite picture. The stitching method simply measures roughness in a grid pattern then merges those individual measurements to give a more macroscopic roughness picture. The surface is clean to the eye and the zoomed out SEM (Figure 14) reveals a surface free of physical degradation. The zoomed in SEM image (Figure 15) allows the grains of WC to be seen and the EDS for the unused inserts sets the baseline to which we will compare the following results. The insert material is comprised of approximately 55% carbon, 40% tungsten, and 5% titanium as detailed in Table 4.
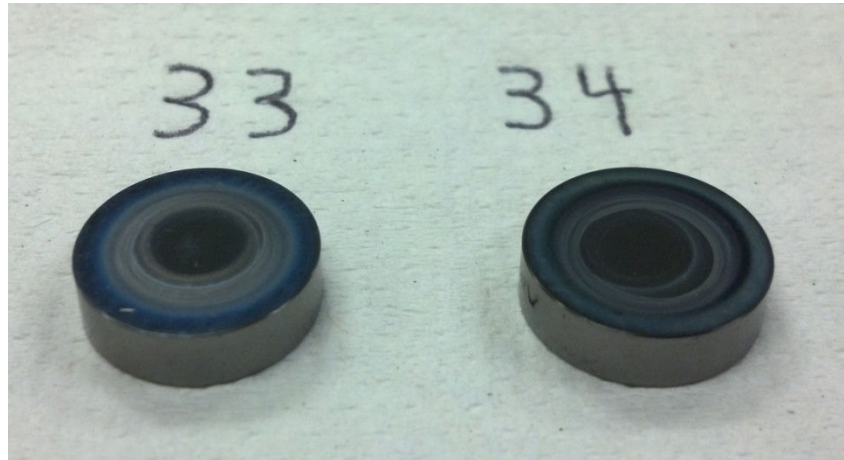
Molds after press 8

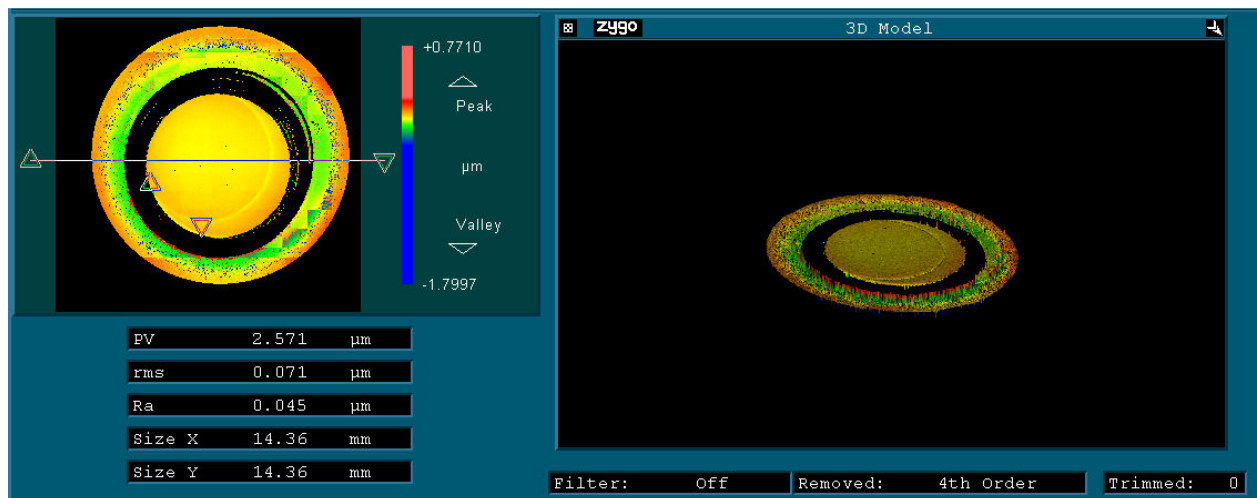**Figure 16: Picture of WC_33 and WC_34 after press 8**
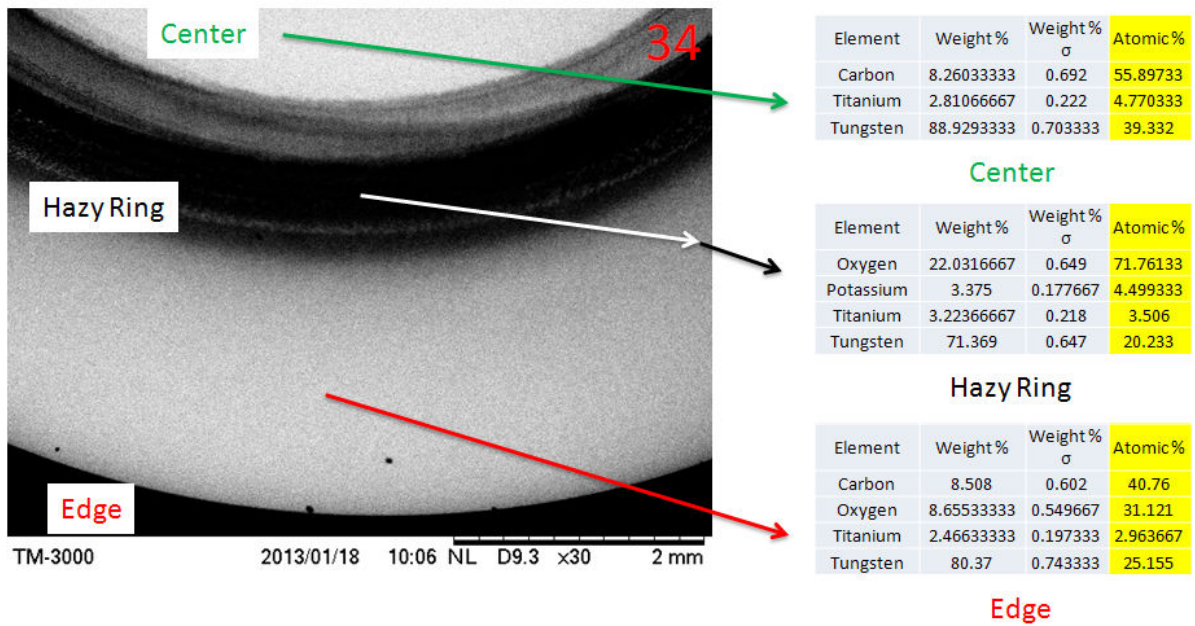

Figure 17: WC_34 Zygo after press 8

Element	Weight %	Weight % σ	Atomic %
Carbon	8.26033333	0.692	55.89733
Titanium	2.81066667	0.222	4.770333
Tungsten	88.9293333	0.703333	39.332

Center

Element	Weight %	Weight % σ	Atomic %
Oxygen	22.0316667	0.649	71.76133
Potassium	3.375	0.177667	4.499333
Titanium	3.22366667	0.218	3.506
Tungsten	71.369	0.647	20.233

Hazy Ring

Element	Weight %	Weight % σ	Atomic %
Carbon	8.508	0.602	40.76
Oxygen	8.65533333	0.549667	31.121
Titanium	2.46633333	0.197333	2.963667
Tungsten	80.37	0.743333	25.155

Edge

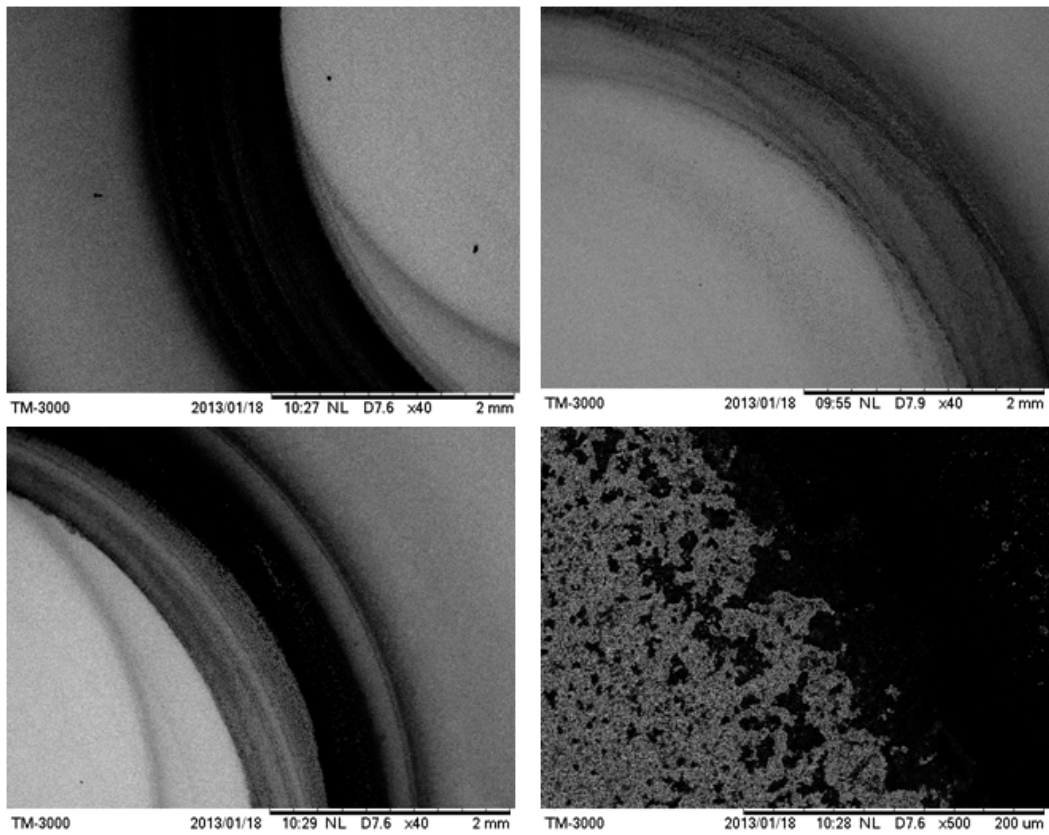**Figure 18: SEM zoomed out & EDS WC_34 after press 8**

Figure 19: SEM zoomed mid WC_34 after press 8

22

After 8 presses between raw WC and N-FK5 glass, the degradation of the mold insert is catastrophic. The SEM in Figure 18 Figure 19 shows the extent of the damage. EDS in Figure 18 shows a marked increase in potassium in the ring region while the oxidation appears complete at ~71%. Oxidation of the edge region of the insert has increased, showing that even though oxidation of the physically damaged regions reaches equilibrium, further chemical damage is still possible to the rest of the insert. Despite the increasing damage to the ring physically and to the edge chemically, the center of the insert which experiences much less material flow shows almost no sign of degradation either physical or chemical. It is safe to say that the physical flow of the glass over the inserts is the most prominent factor in limiting the mold insert lifetime. A self-evident take away from this realization is that molding involving less surface flow of material should limit damage to inserts and increase mold lifetimes.

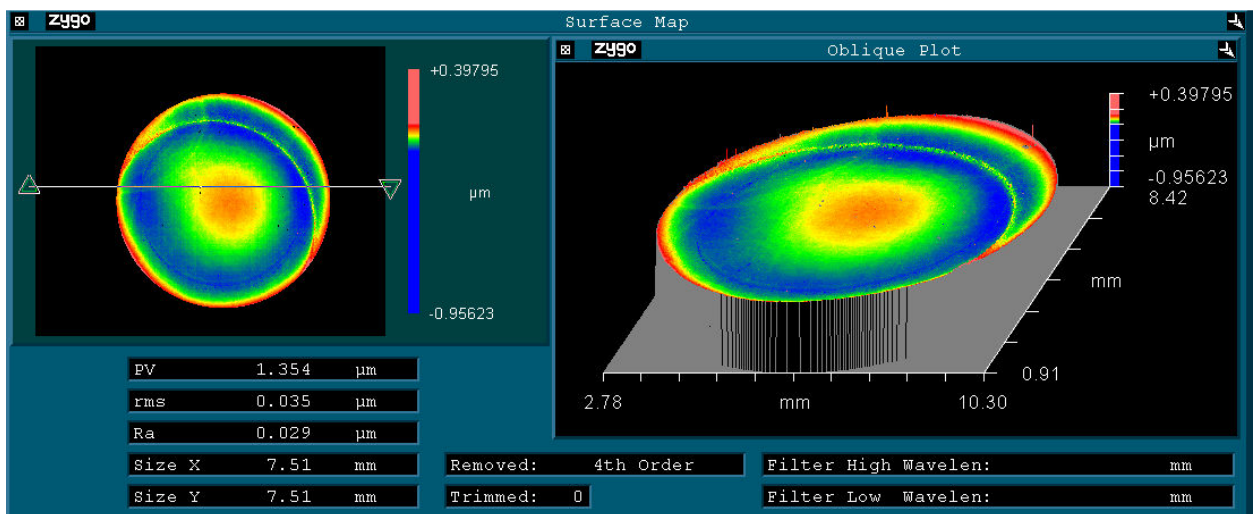**N-FK5 after press 8**

Figure 20: Picture of N-FK5 after press 8

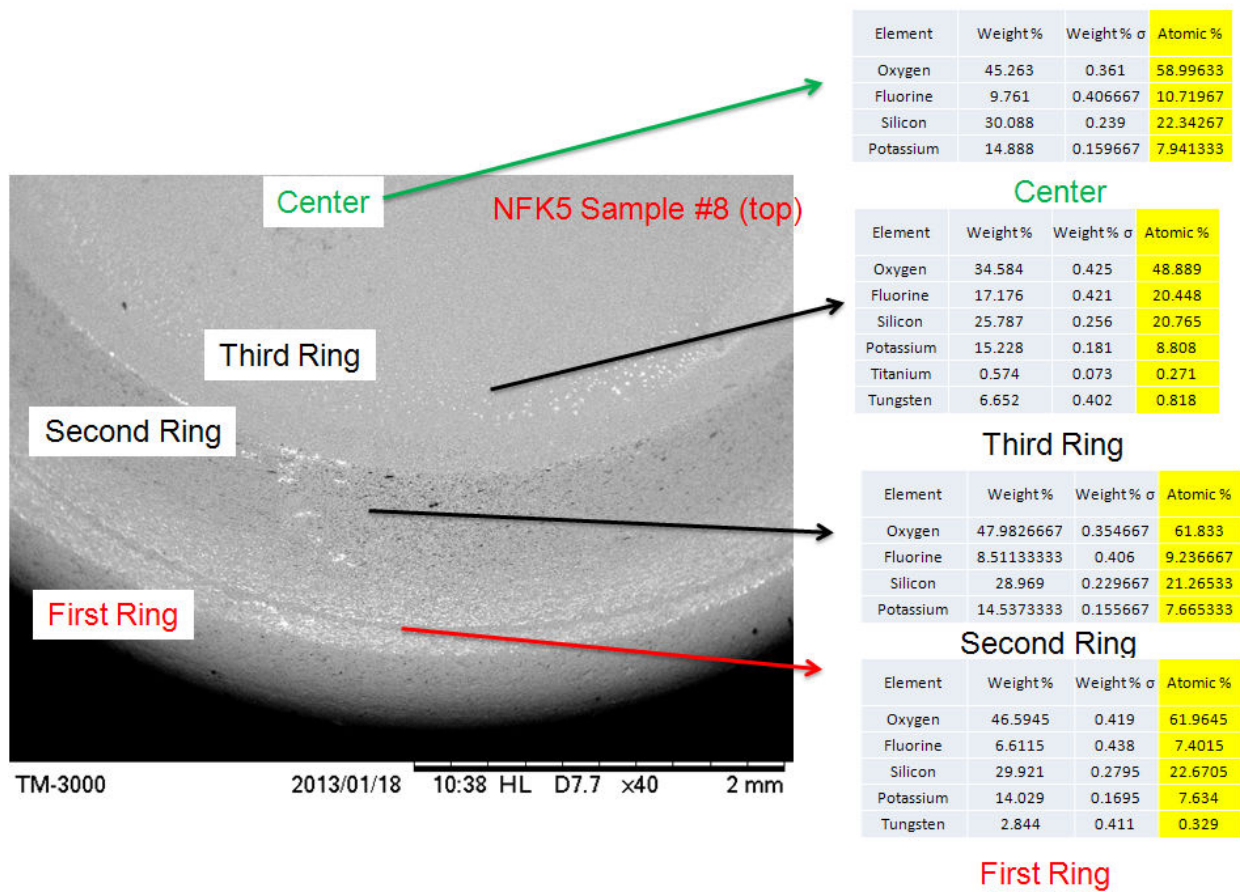Figure 21: Zygo of N-FK5 bottom pressed with WC after press 8

Center

Element	Weight %	Weight % σ	Atomic %
Oxygen	45.263	0.361	58.99633
Fluorine	9.761	0.406667	10.71967
Silicon	30.088	0.239	22.34267
Potassium	14.888	0.159667	7.941333

Third Ring

Element	Weight %	Weight % σ	Atomic %
Oxygen	34.584	0.425	48.889
Fluorine	17.176	0.421	20.448
Silicon	25.787	0.256	20.765
Potassium	15.228	0.181	8.808
Titanium	0.574	0.073	0.271
Tungsten	6.652	0.402	0.818

Second Ring

Element	Weight %	Weight % σ	Atomic %
Oxygen	47.9826667	0.354667	61.833
Fluorine	8.51133333	0.406	9.236667
Silicon	28.969	0.229667	21.26533
Potassium	14.5373333	0.155667	7.665333

First Ring

Element	Weight %	Weight % σ	Atomic %
Oxygen	46.5945	0.419	61.9645
Fluorine	6.6115	0.438	7.4015
Silicon	29.921	0.2795	22.6705
Potassium	14.029	0.1695	7.634
Tungsten	2.844	0.411	0.329

Figure 22: SEM zoomed out & EDS top of N-FK5 after press 8

24

Element	Weight %	Weight % σ	Atomic %
Oxygen	46.6833333	0.349333	60.359
Fluorine	9.40266667	0.396667	10.23833
Silicon	29.7293333	0.230667	21.89733
Potassium	14.184	0.151333	7.505333

Center

Element	Weight %	Weight % σ	Atomic %
Oxygen	35.81	0.52	50.657
Fluorine	14.175	0.42	16.887
Silicon	27.179	0.362	21.901
Potassium	16.413	0.232	9.5
Titanium	0.603	0.073	0.285
Tungsten	5.427	0.743	0.668

Second Ring

Element	Weight %	Weight % σ	Atomic %
Oxygen	45.607	0.435	63.101
Fluorine	5.397	0.4035	6.2795
Silicon	27.7305	0.2715	21.8225
Potassium	13.706	0.169	7.753
Titanium	0.362	0.0715	0.168
Tungsten	7.197	0.4075	0.8755

First Ring

Figure 23: SEM zoomed out & EDS bottom of N-FK5 after press 8

The sample involved in the 8th press continues the trend of chemical cross contamination. Both the top and bottom of the samples show significant Ti and W residue while the center of both top and bottom remain essentially unchanged. It is helpful to look at the glass, mold relationship as a mirror. The glass, at high temperature is inherently formable and therefore retains the features of the mold insert. During the first few presses, degradation is caused by the glass on the mold; once that degradation is severe enough it begins to be reflected in the post-pressed glass piece. The glass initially degrades the mold insert and continues to throughout pressing; likewise after a certain degradation threshold has been reached the mold insert begins appreciably degrading the sample. This cycle of degradation is important to acknowledge GPCL looks for ways to delay initial mold degradation and push the destructive cycle back as far as possible.

Molding Work Summary

GPCL developed a detailed, analytical process to evaluate mold tooling-glass material interaction tendencies in PGM. The work listed above is a representative sample of the extensive knowledge we have gained in this area over the past year. In addition to N-FK5 and tungsten carbide, we have also analyzed mold behaviors using SiC as well as coated WC and glassy carbon molds. This knowledge coupled with our ongoing work on the characterization of structural relaxation behavior paints a complete picture of the "know-how" needed in both

research and development to successfully refine the PGM process. These initial findings have already been extended now to non-oxide (chalcogenide glass) and are forming the basis of further use of this know-how, in commercially relevant materials important to both civilian and military applications.

REFERENCES

1. S. M. Rekhson, 'Modelling of viscoelastic and structural relaxation in glass,' *J. Non Cryst. Solids*, 73 [1-3] 151-64 (1985).

2. S. Gaylord, 'Thermal and Structural Properties of Candidate Moldable Glass Types,' MS Thesis, Materials Science and Engineering, Clemson University (2008).

3. C. T. Moynihan, S. N. Crichton and S. M. Opalka, 'Linear and nonlinear structural relaxation,' *J. Non Cryst. Solids*, 131 [2] 420-34 (1991).

4. E. Koontz, V. Blouin, P. Wachtel, J. D. Musgraves and K. Richardson, 'Prony series spectra of structural relaxation in N-BK7 for finite element modeling,' *Journal of Physical Chemistry A*, 116 [50] 12198-12205 (2012).

5. J. C. Phillips, 'Stretched exponential relaxation in molecular and electronic glasses,' *Reports on Progress in Physics*, 59 [9] 1133-207 (1996).

6. M. Potuzak, R. C. Welch and J. C. Mauro, 'Topological origin of stretched exponential relaxation in glass,' *J. Chem. Phys.*, 135 [21] 214502 (7 pp.) (2011).

7. C. T. Moynihan, A. J. Easteal, M. A. DeBolt and J. Tucker, 'Dependence of the fictive temperature of glass on cooling rate,' *J Am Ceram Soc*, 59 [1-2] 12-16 (1976).

8. N. W. Tschoegl, 'Representation by Series-Parallel Models'; pp. 136-145 in The Phenomonological Theory of Linear Viscoelastic Behavior: An Introduction. Springer-Verlag, Berlin, Heidelberg, New York, London, Paris, Tokyo, 1989.

Appendix B. Experimental characterization of stress relaxation
Vincent Blouin and Eric Koontz

Introduction

This document includes a report of activities related to stress relaxation during year 3 of the project.

Table 5 details the tasks that were assigned to Dr. Blouin's group.

Table 5: Original Proposed Tasks

B.1	Stress relaxation characterization: initial elastic response and viscosity at molding temp.
B.2	Stress relaxation characterization: time-dependent response in shear and in volume and numerical optimization
B.3	Stress relaxation property measurements of glass types in support of modeling activities (as needed)

All activities performed by Erick Koontz during year 3 have aimed at achieving these three tasks as well as additional tasks of the project. They are listed below in Table 2.

Table 6: On-going Tasks

Activity	Description	Related to proposed tasks
1	Fabrication of high temperature torsion tester	B.1-2
2	Proof of concept - Initial shear stress relaxation from torsion tester	B.1-2
3	Characterization of structural relaxation	A.1-3
4	Development of a novel Prony series fitting methodology applied to experimental data from stress and structural relaxation measurements	A.1-3, B.2-3

Background on Stress and Structural Relaxation

Glass relaxation is a phenomenon inherent to a network glass in the temperature region around the glass transition temperature (T_g). These relaxations occur as a result of applied temperature difference and applied load.

Stress relaxation is the motion of a glass network to minimize the stress state within the material when an external load is applied. This relaxation can occur in response to two different types of stress. The first is shear stress which causes a change in shape of a unit in the material. The second is hydrostatic stress which causes a volume change in a volume unit of material without changing the shape. When either (or both) of these stress types is applied, a glassy material will relieve the stress by rearranging the network. This is a viscoelastic behavior and is therefore time dependent. The viscous component of relaxation provides the time-dependent behavior of stress relief while the elastic component is more or less instantaneous. For precision glass molding (PGM) it is

important to understand how an applied stress affects the material, this includes both a material's instantaneous response as well as its time-dependent response.

Structural relaxation occurs in response to temperature change within a material. Glassy materials are, by definition metastable or nonequilibrium solids. That is to say, their structure as a solid is frozen in from the liquid state. So the structure of the material as a solid looks like the liquid when the liquid is at a given temperature. This temperature is called the fictive temperature (T_f) and it is used to describe the frozen structure of a nonequilibrium solid from an equilibrium liquid reference point. When the temperature within a glass changes, its equilibrium structure (which is a representation of its fictive temperature) changes. However, in the temperature region around T_g, the structure relaxes in a time-dependent exponential-like way very similar to stress relaxation. This change of structure as a function of temperature leads to a macroscopic change in shape of the bulk glass. This becomes important in PGM because as a glass lens is cooled, its shape changes, and knowing how the shape changes is important for hitting target dimensions of a molded lens.

Activity 1 – Fabrication of Torsion Tester

A high temperature torsion tester was designed in year 2 to perform shear stress relaxation tests on glass rods. The tester is shown in Figure 24 and the details of the design are provided in the Year 2 Annual Report. The tester was completed and assembled in year 3. All parts of the frame, motor and load cell are new. The used furnace was upgraded with a new temperature controller.

The tester was designed to fill a void in the capabilities of mechanical testing of glasses. Mechanical testing of glasses is not a trivial endeavor. The viscoelastic stress relaxation behavior is relevant not only to intentional loading of the material for stress relaxation testing, but also to the loading applied to the glass by the test fixtures. This makes it especially difficult to grip glass for mechanical testing because one must ensure that the loading applied to fix the sample does not affect the measurement being made. Torsional dynamic mechanical analyzers (DMA) are often used to do the type of testing proposed in this task. A DMA can apply a load to a sample at temperature either hydrostatically or in torsion for shear measurements. However many DMAs and those available for this project have upper operating temperatures of 400 – 500 °C, the temperature regions in which viscoelastic effects could be seen in the oxide glasses such as Schott N-BK7 which are being tested, are in the 500 – 600 °C range. A high temperature DMA is unavailable, that is the reason for designing and building an instrument that can measure shear stress relaxation.
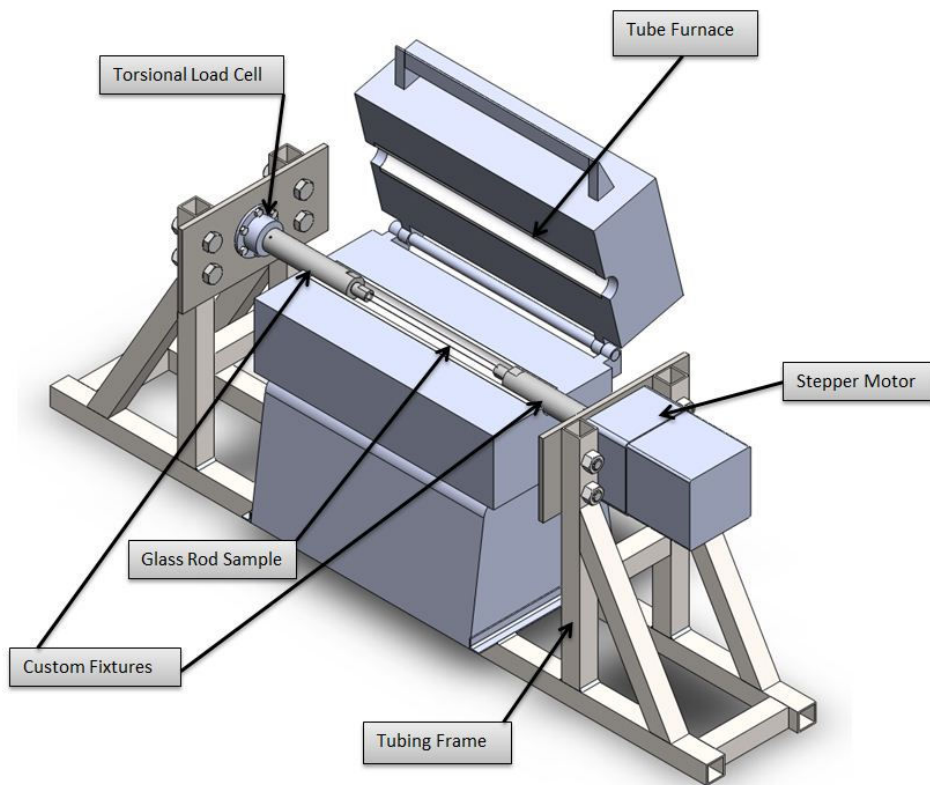
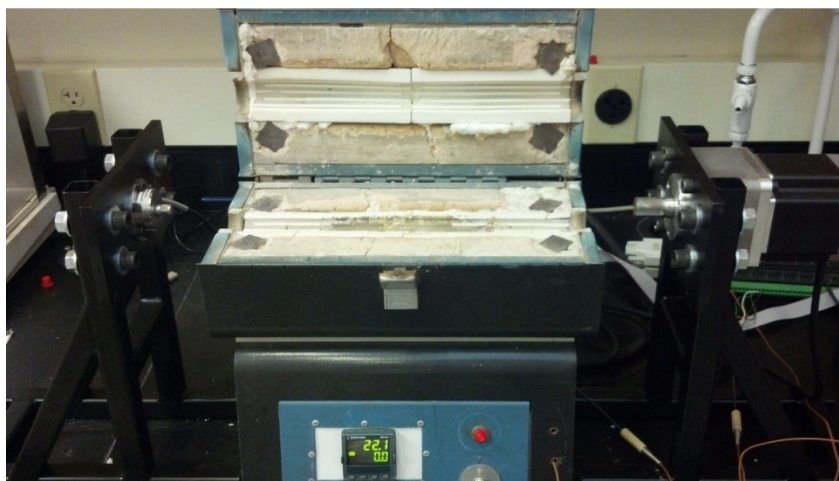**Figure 24: Torsion Tester Design**

Figure 25: HTTMA pictured with tube furnace open

The torsion tester (Figure 25) is designed to impose an instantaneous angular displacement on a heated glass rod using a stepper motor shown in Figure 26. The glass rod is fixed to the stepper motor at one end and to the load cell at the other end.

Inappropriate fixturing of the glass sample is generally a source of inaccuracy of this test. Since the glass sample is in a viscoelastic state, holding the glass sample by its ends is challenging due to potential slippage and stress concentration. Mechanical and chemical bonding techniques are being investigated as part of this project for glass types of interest. Macor glass ceramic fixtures were fabricated and installed on the tester as shown in Figure 26 and Figure 27. Macor material was selected for its low thermal conductivity, its chemical bonding compatibility with various glass types, and its ability to be machined easily. Currently, the Macor fixture is a solid cylinder with a flat end on which the glass sample is either glued using a high temperature ceramic compound or fused at high temperature (500 to 600 °C).
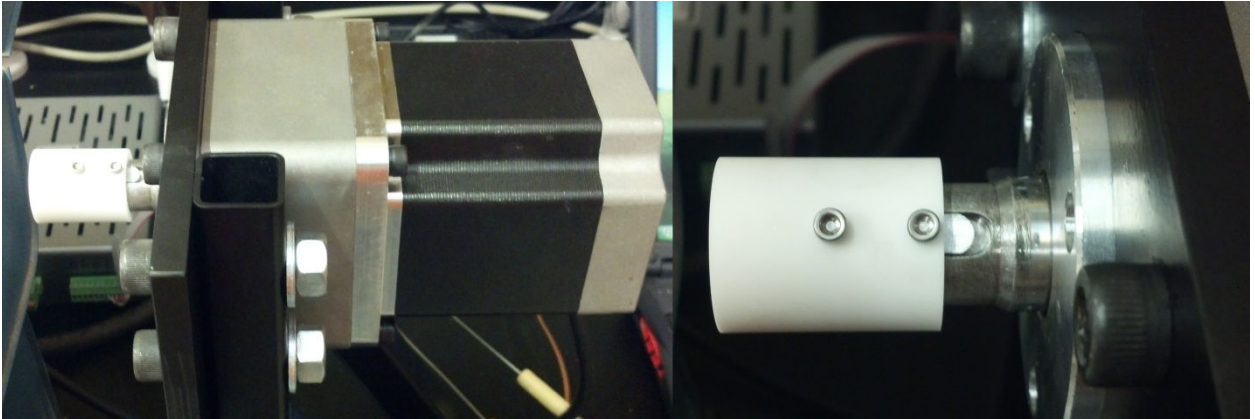
Figure 26: Stepper motor and Macor glass ceramic fixture (white cylinder)
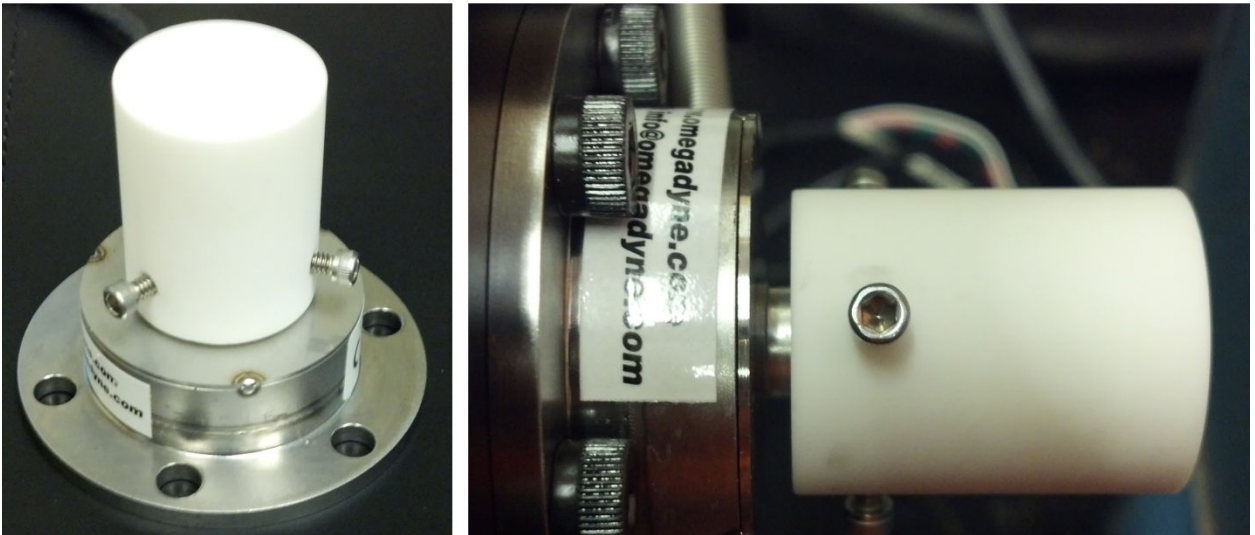
Figure 27: Torsional load cell and Macor glass ceramic fixture (white cylinder)

This torsional displacement (i.e., twist angle) imposed by the stepper motor causes a shear stress within the material. In a relatively high temperature viscoelastic state, the glass immediately begins to relax as the shear stress reduces gradually. The torsional load cell (or torque cell) shown in Figure 27 measures the resulting torque as a function of time. The temperature dependence of the shear stress relaxation process is of interest

and will be measured by performing the stress relaxation test at various temperatures, each test being performed at uniform and constant temperature.

Activity 2 – Proof of concept – Initial shear stress relaxation from torsion tester

Once the torsion tester pictured and detailed above was constructed, work began prepping the tester for proof of concept testing before investing in further fixturing. The initial shear stress relaxation test was carried out on a Pyrex tube 0.35 m long that was fused to the load cell and stepper motor with its ends sticking outside of the furnace to circumvent issues with high temperature fixturing.

The Pyrex tube was fixed at both ends and the furnace ramped to the T_g of Pyrex (560 °C) and additional tests were performed at higher temperatures (up to 580 °C). The furnace was held at that temperature for 15 minutes to ensure the entire tube reached thermal and structural equilibrium. Once the equilibration hold was complete, the stepper motor was used to impart an instantaneous angular displacement on the tube. On a computer attached to the data acquisition system (DAQ) that the load cell feeds to, a sharp jump was seen followed by exponential decay. This exponential decay is the tell-tail sign of stress relaxation occurring. The force on the load cell decayed to nearly zero.

Figure 5 shows the torque as a function of time for the test at 560 °C and Figure 29 shows the relaxation function (ie, normalized torque) for five different temperatures.
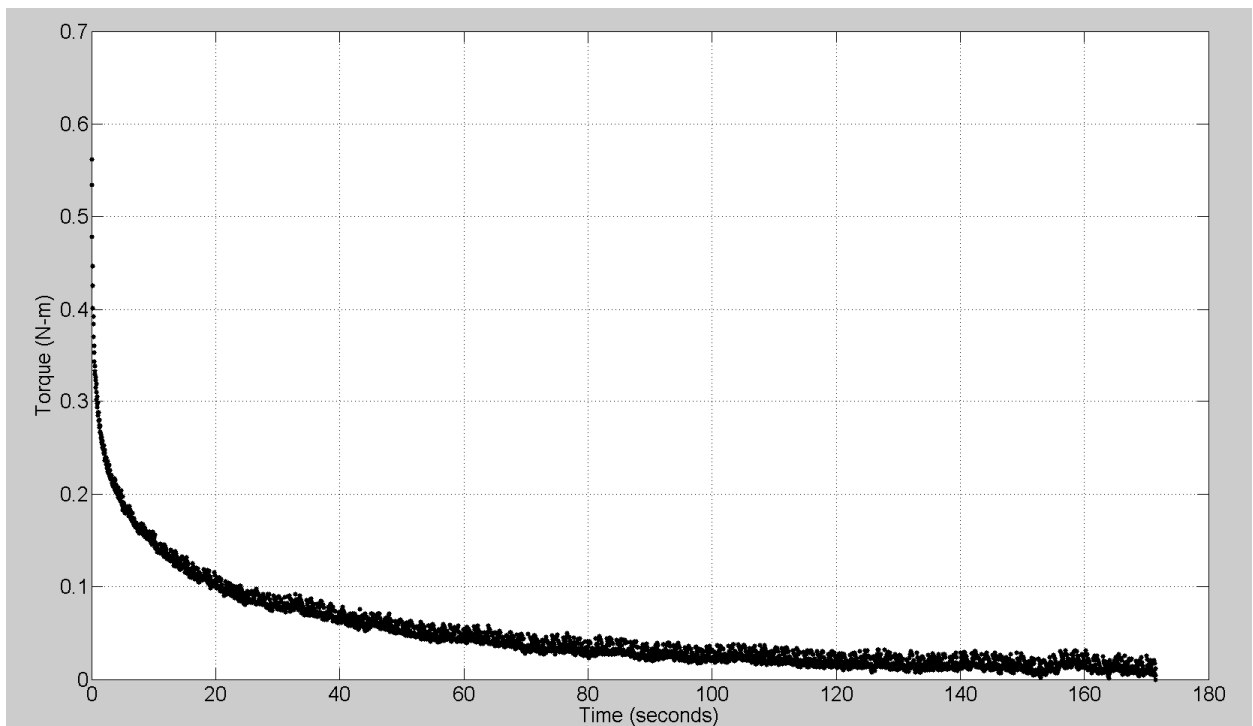
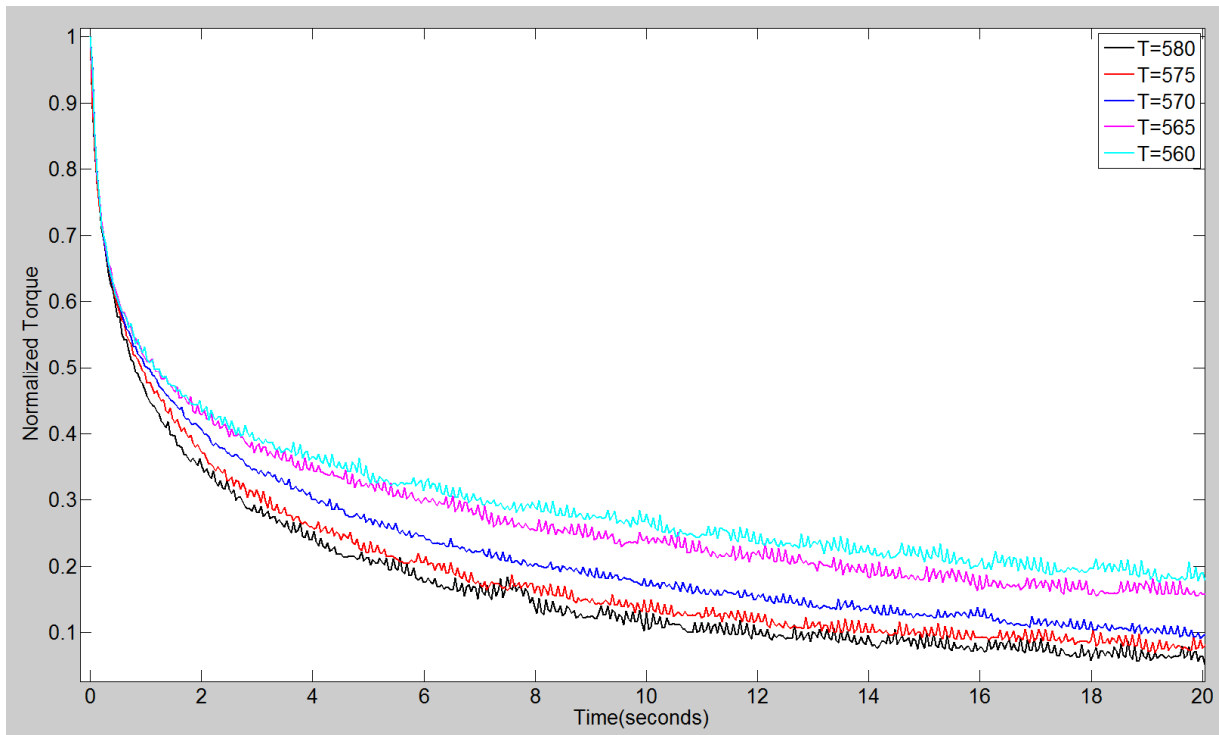**Figure 28: Stress relaxation behavior Pyrex tube, 560 °C**

Figure 29: Comparison of stress relaxation curves 560-580 °C

Even though this was only a proof of concept the consistency of the trends in the data is as expected. At higher temperatures the viscosity of the glass is lower, allowing the material to relax the stress away faster. The graph shows that this is indeed the case with the lower viscosity runs showing a faster relaxation and the higher viscosity runs taking longer to relax away the same amount of stress. In light of these results it is safe to say that the torsion tester works as it was designed and the move can be made to make permanent fixtures and begin actual testing.

Activity 3 – Characterization of structural relaxation

In order to characterize the structural relaxation for the reasons stated above, a thermo mechanical analyzer (TMA) was used. An N-BK7 glass sample was placed in the TMA as shown in Figure 7. Platinum foil was placed at both ends of the sample to prevent it from fusing to the silica probe or the silica stage during testing. The sample was ramped at 5 °C/min to a temperature above T_g to erase the effects of any previous heating or cooling cycles. The temperature was then ramped to the test temperature at a rate of 1 °C/min. It was held isothermally for as long as deemed necessary for the glass to reach total structural equilibrium, this was said to be the time at which the glass stopped showing nonlinear deformation. Once thermal and structural equilibrium was reached, a 5 °C temperature down step was initiated at 20 °C/min. The sample was held at the final temperature until it once again reached structural equilibrium. This was done for several final temperatures from 542 to 577 °C. The relaxation curves can be seen in Figure 8.
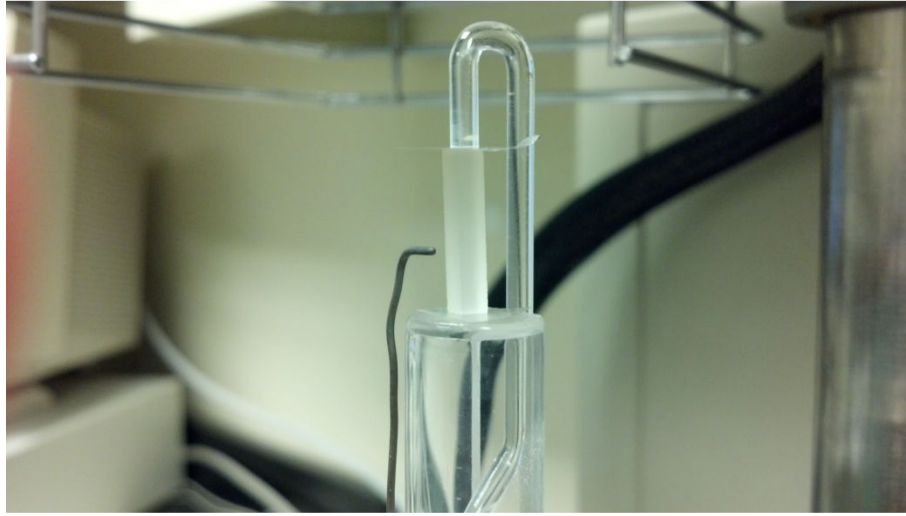
32

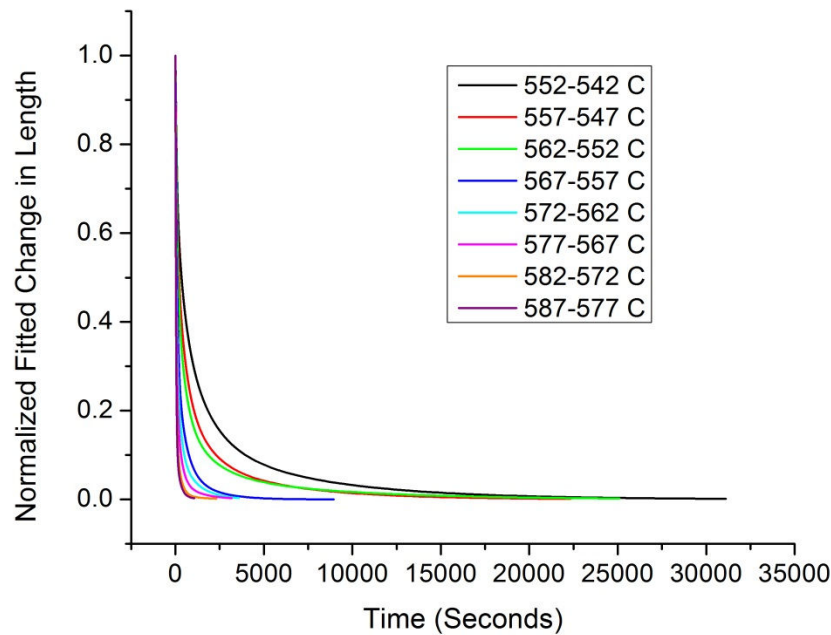**Figure 30: TMA with N-BK7 sample for structural relaxation measurements**

Figure 31: Structural relaxation curves for N-BK7 measured by TMA

Similar to the stress relaxation curves in Activity 2, these structural relaxation curves follow the trends expected with higher temperatures, lower viscosity samples relaxing to their equilibrium structure faster than at higher viscosities. The analysis of this data and the data presented in Activity 2 will be detailed in Activity 4.

Activity 4 – Development of novel Prony series fitting model applied to experimental data from stress and structural relaxation measurements

The nature of viscoelastic stress relaxation behavior of glass as well as that of the structural relaxation of a glass network leads to the need for a model that captures the exponential-like behaviors and can accurately quantify them. Since the shear stress relaxation testing is just finishing the proof of concept phase, the following analysis has not yet been done on that data. However it has been developed and used extensively on the structural relaxation data detailed in section 3. In order to fit the experimental data obtained by TMA experiments, a Prony series was employed.

$$\phi(t) = \sum_{i=1}^{N} w_i * e^{-\left(\frac{t}{\tau_i}\right)} \tag{1}$$

Error! Reference source not found.) shows a generic Prony series where w_i is the weight term and τ_i is the relaxation time constant or tau. Note that the novelty presented here lies in the numerical procedure used to curve-fit the Prony series to the experimental data. The data from the curves in Figure 8 was analyzed using a unique Prony series fitting method developed by Dr. Blouin's group. The data was imported to Matlab and fitted using the FMINCON function and a least squares method of optimization. An array of reasonable tau values were input to the optimizer and the computer solved for the weight values in order to fit the data. The only constraint other than the specified taus was the condition that all weights had to sum to unity. Once the data was fit with the Prony series an error of $R^2=0.9996241$ was found, this included several thousand Prony taus. This signifies a good numerical fit of the data. Figure 9 shows an example of the visual accuracy of the fit.
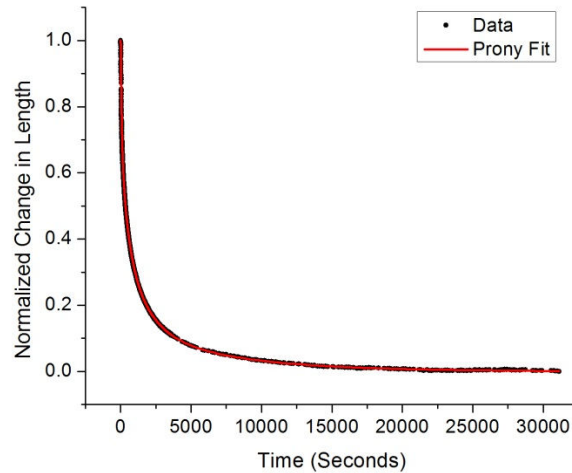

Figure 32: Prony series fit shown with original relaxation data
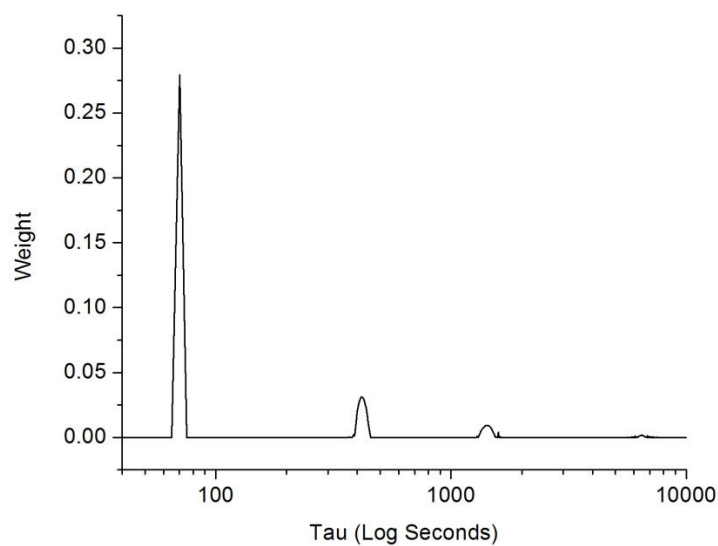
Many efforts were made to ensure that the fit of

Figure 33: Prony series spectrum, a plot of w_i versus τ_i

In Figure 33 the plot of the weights versus taus shows several interesting features. The first is four distinct tau peaks. Each tau value that is significantly non-zero will form a spike or a peak, we see in this case that we have four such distributions of taus. This consequentially would lead us to believe that a four term Prony series is the smallest that can represent the experimental data. To test this a fit was done by inputting only four terms and the result was a good fit with an R^2 of 0.9996239, only slightly worse than the fit that had several thousand terms. Fits were also attempted with less than four terms and were not successful in producing R^2 values nearly as high as the four term fit.

The second point of interest was how the taus and weights would change with temperature. Fitting of all the temperature runs shown in Figure 8 was done and the results compiled. In Figure 34, the tau values of each peak (e.g. first, second, third) are plotted and the first noticeable feature is that the tau values do not change much with temperature. Within the error bars they could be said to be nearly equivalent.
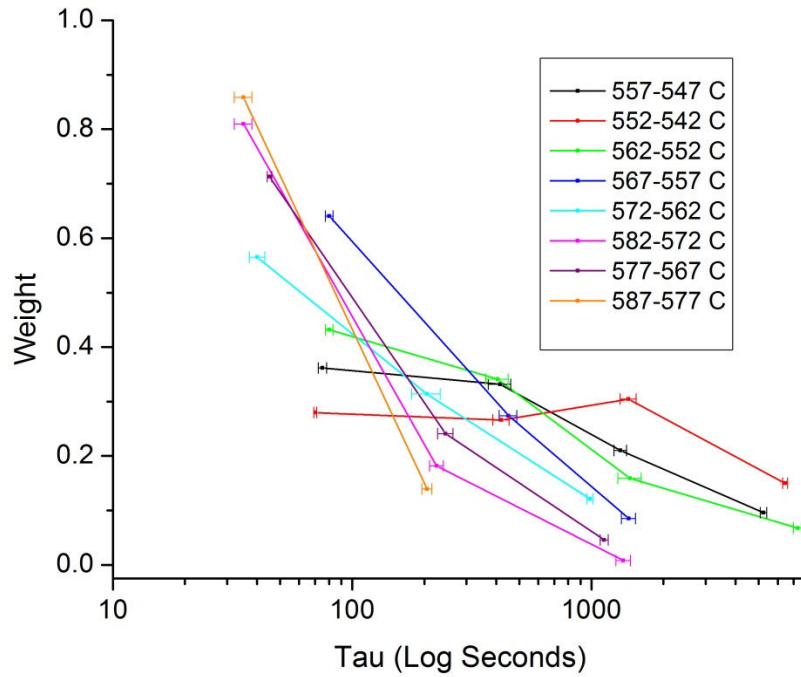
35

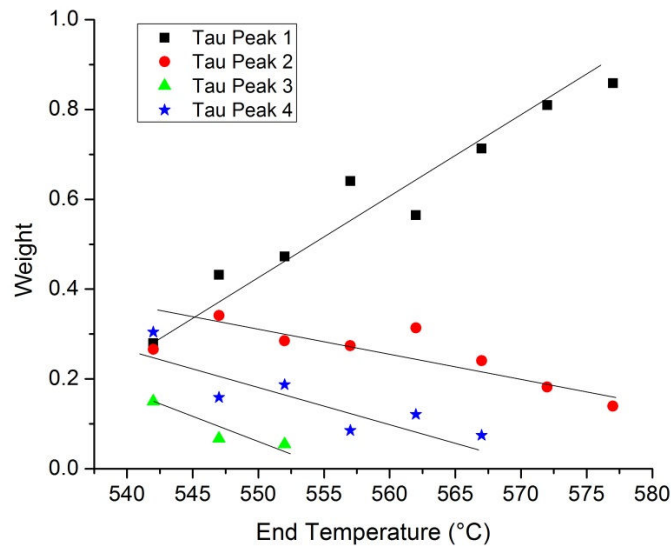**Figure 34: Prony spectrum for N-BK7 from 547-577 °C, using 5 °C temperature jumps**

Figure 35: Prony weight trends versus temperature

Since the taus do not significantly vary with temperature, attention can be given to the weights which most certainly change. Figure 12 shows that weights vary more or less linearly with temperature. The first peak weights increase with temperature while all other peak weights decrease with temperature. This leads to the conclusion that at higher temperatures the glass should display single exponential relaxation behavior, which is known to be the case. These weight trends can be fitted with a linear function and input back into a Prony series with the appropriate taus to define a master equation (Equation

t,T= i=14miT+bi∗e−tτi   (2)

Table 7, describes the structural relaxation behavior of N-BK7 in this temperature range.

$$\phi(t,T) = \sum_{i=1}^{4}(m_i T + b_i) * e^{-\left(\frac{t}{\tau_i}\right)}$$ (2)

Table 7: Weight trend parameters as functions of temperature

	Slope (m)	Intercept (b)	R^2
Peak 1	0.0157	-8.1739	0.94
Peak 2	-0.0042	2.6196	0.6
Peak 3	-0.0084	4.826	0.85
Peak 4	-0.0095	5.29	0.85

Equation (2) can be input to a finite element modeling program to describe the dimension change of a glass work piece under temperature induced shape change within this temperature range. This equation allows modelers to ignore whether or not a material adheres to thermo rheological simplicity assumptions or not and simplifies the modeling process all together.

This method was shown as an appropriate way to characterize structural relaxation in amorphous, viscoelastic solids. This same technique can be applied to shear stress relaxation data in order to define a material's time-dependent response to stress.

Future Work

Future work for year 4 includes the continuation of all tasks described above in order to achieve the original proposed tasks. More specifically:

Task-1 – High temperature torsion tester fixtures

- Pursue ways to fixture a samples made of various glasses of interest to the stepper motor and load cell of the torsion tester such that the fixturing does not affect the experimental results, including:
    - Mechanical bonding of glass to substrate
    - High temperature cementing
    - Low impact gripping of sample

Task-2 – Shear stress relaxation testing of N-BK7 rods

- Do a full characterization of shear stress relaxation in N-BK7
- Study temperature and time dependence of relaxation
- Study dependence of relaxation on initial loading and rate of loading

Task-3 – Characterization of structural relaxation in other glasses in support of modeling group

- Will characterize structural relaxation of specified glasses as needed for inputs for modeling

- o Chalcogenides
- o Other moldable oxides

Publications

- E. Koontz, V. Blouin, P. Wachtel, J. D. Musgraves, K. Richardson, "Prony series spectra of structural relaxation in N-BK7 for finite element modeling," Presented at the 2012 Glass & Optical Materials Division Spring Meeting, The American Ceramic Society, May 20-24, St. Louis, MO, 2012.
- E. Koontz, V. Blouin, P. Wachtel, J. D. Musgraves, K. Richardson, "Prony Series Spectra of Structural Relaxation in N-BK7 for Finite Element Modeling" Journal of Physical Chemistry (Submitted August 2012).
- H. Kadali, E. Koontz, V. Blouin, K. Richardson, P. Joseph, "On The Characterization of Stress Relaxation of Glass Using Helical Samples" (In Preparation).

Appendix C. Computational analysis of lens molding
P. Joseph, D. Joshi, M. Trabelssi

During the course of this grant the following journal papers (available at the ARO report site) with a focus on computational mechanics, were published:

- B. Ananthasayanam, P.F. Joseph, D. Joshi, S. Gaylord, L. Petit, V.Y. Blouin, K.C. Richardson, D.L. Cler, M. Stairiker, M. Tardiff, "Final shape of precision molded optics: Part I – Computational approach, material definition and the effect of lens shape" *J. Thermal Stresses* 35, pp. 550-578, 2012.
- B. Ananthasayanam, P.F. Joseph, D. Joshi, S. Gaylord, L. Petit, V.Y. Blouin, K.C. Richardson, D.L. Cler, M. Stairiker, M. Tardiff, "Final shape of precision molded optics: Part II – Validation and sensitivity to material properties and process parameters," *J. Thermal Stresses* 35, pp. 614-636, 2012.
- D. Joshi, P. Mosaddegh, J. D. Musgraves, K. C. Richardson, P. F. Joseph, "Thermo-Mechanical Characterization of Glass at High Temperature Using the Cylinder Compression Test: Part I –Viscoelasticity, Friction and PPV," *J. Rheol.*, 57 1367-1389, 2013.
- D. Joshi, P. Mosaddegh, J. D. Musgraves, K. C. Richardson, P. F. Joseph, "Thermo-Mechanical Characterization of Glass at High Temperature Using the Cylinder Compression Test: Part II – No-Slip Experiments, Viscoelastic Constants and Sensitivity," *J. Rheol.*, 57, 1391-1410, 2013.
- B. Ananthasayanam, D. Joshi, M. Stairiker, M. Tardiff, K.C. Richardson, P. F. Joseph, "High Temperature Friction Characterization for Viscoelastic Glass Contacting a Mold," *J. Non-Cryst. Solids*, 385, 100-110, 2014.
- D. Joshi and P.F. Joseph, "Parallel Plate Viscometry for Glass at High Viscosity," to appear, *Journal of the American Ceramic Society*.

In addition the following three papers, which are included at the end of this section as Appendices C1, C2 and C3, will soon be submitted:

- C1. D. Joshi and P. F. Joseph, "Sensitivity analysis of lens shape deviation and residual stresses within the precision molded lens."
- C2. M. Trabelssi, H. Ebendorff-Heidepriem, K. C. Richardson, T. Monro and P. F. Joseph, "Prediction of Die Swell of Extruded Glass Preforms at High Viscosity."
- C3. M. Trabelssi and P.F. Joseph, "Ring compression test for high temperature glass based on the generalized Navier law."

Current and Future Work. The above journal papers detail the past work in lens molding, and out of necessity, the large effort in obtaining material characterizations (viscosity, friction and stress relaxation). The three papers in the Appendices describe the current work. The two doctoral students involved, Dhananjay Joshi and Mohamed

Trabelssi should graduate in May 2014. Both have a few details before completing their doctoral program. Of interest in this current work is the difficulty we are having being certain that the residual stresses predicted by the computational procedure are correct. We believe this all comes back to the reliability of the material characterizations. Although we are very grateful for the no-cost extension which allowed us to provide much more deliverables to our final report in the form of published papers, we still need more time to bring this effort to completion. Hopefully the field will appreciate that in order to make reliable predictions, it is essential to have material characterizations beyond what is available in the literature. I expect the future work of D. Joshi will show this.

Appendix C1: (Paper DRAFT)

Sensitivity analysis of lens shape deviation and residual stresses in the precision molded lens

Dhananjay Joshi and Paul F. Joseph*

Department of Mechanical Engineering, Clemson University, SC 29634-0921.

ABSTRACT: Computational mechanics approach is a widely used to understand and overcome commonly encountered issues in lens molding application. These issues include lens shape deviation, stress induced birefringence and lens cracking. The computational modeling of lens molding process involves detailed knowledge of viscoelastic material behavior of the optical glass which is often not available easily. The process of finding the detailed viscoelastic characterization of a glass at a given temperature and its temperature dependence can be very demanding process as it may involve series of complex experiments. This research investigates the level of details required in modeling the viscoelastic behavior of glass and its effect on some of the lens molding issues mentioned above. For example, we found out that the final size and shape of the lens is influenced by factors such as: high temperature elastic modulus (E) of the glass, an error in reference temperature of glass (T_R), and the convective heat transfer coefficient modeled between the mold, lens and the surroundings. Three different level of details for viscoelastic stress relaxation behaviors of glass were considered: 1) Simple - single Maxwell element for modeling response in shear and an elastic element for bulk response, 2) Intermediate - multiple Maxwell elements for modeling response in shear and an elastic element for bulk response, 3) Complex- multiple Maxwell elements for modeling both shear and bulk response. It was found that these modeling details have no effect on the final size and shape of the lens but do affect the residual stresses inside lens to greater extent. An example calculation of a stress birefringence inside the glass lens will be shown at the end. It is concluded that in order to accurately predict the residual stresses inside lens, the detailed viscoelastic characterization of glass is required.

1. INTRODUCTION

Computational mechanics approach is widely used to model the complex thermo-mechanical behavior of an optical glass during simulation of the lens molding, extrusion and other glass forming processes. This approach proves to be an effective tool in understanding and overcoming the associated shortcomings such as lens profile deviation (final shape), stress birefringence, lens cracking etc. in the molding process, while, the preform die swell, cavity shape distortion etc. in the extrusion process. The accuracy of prediction of above parameters strongly depends upon input of the thermo-mechanical properties of the glass to the numerical model. These properties mainly include the stress and structural relaxation parameters, temperature dependent values of elastic modulus and the temperature dependent viscosity (TRS parameters). The thermo-mechanical characterization of glass focusing mainly on the lens molding process is carried out by several researchers [1-15] experimentally and/or computationally by treating the optical glass as either viscous or viscoelastic solid material.

Lens molding process is a hot forming process in which the optical glass material in the form of a gob, ball or a near net shape (preform), is subjected to a molding temperature above its glass transition temperature and is compressed between a two dies to impart the desired shape to the glass. A preform undergoes changes in its mechanical properties as it is being heated from the room temperature up to the molding temperature. This temperature dependent mechanical response of such glass can be modeled using suitable material models available in literature. For example, a viscoelastic stress relaxation function is commonly used by researchers to model the mechanical response behavior of glass during lens molding process. Joshi et al. [1,2] and Ananthasayanam et al. [3,4] used viscoelastic material to model glass forming process at high temperature using a cylinder and ring compression test respectively. Yi and Jain [5] modeled the

hot glass as rigid visco-plastic material during forming/pressing stage while, as an elastic-viscoplastic material during annealing/cooling stage. The flow of glass during forming temperature was assumed to obey the Newtonian law, while the bulk behavior was modeled as elastic. Other researchers [6-9] used time dependent shear modulus (generalized Maxwell model) and elastic bulk modulus to model the behavior of glass at high temperature. Chang et al [10] and Yan et al [11] used power law model that relates stress to a power of strain rate to describe the flow behavior of glass at high temperature. Zhou et al [12] used a Maxwell and a Kelvin element in series to model the viscoelastic relaxation response. Duffrene et al. [16] performed experiments on soda-lime-silica glass near transition temperature (T_g) of glass to extract a complete description of stress relaxation behavior of the soda-lime-silica glass sample. Their data includes both the shear as well as bulk relaxation parameters.

Many authors considered that elastic modulus remains unchanged from its room temperature value throughout the thermal cycle of lens molding process. Loch and Krause [17] considered temperature dependent elastic modulus of glass at high temperature. They performed numerical simulations of glass shaping process at high temperature and they considered value of elastic modulus drops to about 1/10 of its value at the room temperature based on the experimental evidence. Comprehensive data on temperature dependence of elastic modulus is provided in study by T. Rouxel [18]. It reveals that for a group of Chalcogenide glasses, the elastic modulus drops below 10GPa as temperature is further increased above T_g. In an extensive study of sensitivity parameters affecting the lens shape deviation by Ananthasayanam et al [4], it was shown that the TRS behavior of glass within the molding temperature range greatly affects the lens deviation for both types of lenses. On the other hand, they concluded that the reference temperature (T_R) of the glass does not affect the deviation as long as the lens is heated to the same molding temperature at the beginning of pressing stage. The sensitivity of the thermal contact conductance coefficient

and the decay profile on the lens shape deviation was studied by Ananthasayanam et al [4]. They concluded that both factors only affect the pressing time but not the lens shape deviation. The effect of convective heat transfer between the outer surface of preform/lens and the surrounding nitrogen environment in addition to the contact conductance coefficient was considered by Yi et al [5] in their numerical simulations along with the thermal contact conductance between glass and mold. They considered the convective heat transfer coefficient of 20 and 200 W/m^2K during heating/soaking and cooling stages respectively.

In this study, we begin by presenting the FEA convergence results for a steep meniscus lens subjected to a typical lens molding cycle. We primarily use two lens shapes in this study: Bi-convex and steep meniscus. We examine the sensitivity of certain material and process parameters on the final size and shape of lens (lens profile deviation) and residual stresses within the lens shapes considered. Three parameters are considered for studying the lens shape deviation include: elastic modulus of glass at high temperature ($E(T)$), error in the reference temperature of glass (T_R) and convection heat transfer coefficient (h_{conv}) between lens mold assembly and surroundings. The effect of different levels of detail in stress relaxation modeling, on the lens profile deviation and residual stress state inside the molded lens will be considered.

2. MODELING DETAILS

The thermo-mechanical properties of the optical glass such as viscoelasticity and temperature dependent TRS behavior and the details of the finite element model used in this study can be found in Table III of [1] and Table I and II of [2]. The lens profile deviation is defined as geometrical difference between the desired profile (mold) and the final shape of the molded lens [3]. The two lens shapes namely Bi-convex and steep meniscus are considered for this sensitivity study.

The sensitivity of stress relaxation parameters on lens shape deviation is studied by utilizing the stress relaxation functions given by Duffrene et al [17]. The details of the parameters used in Abaqus are given in Table 1. One of the aims of this study is to determine the level of detail of stress relaxation model that is required for determining the lens shape deviation within a certain level of accuracy. To understand the effect of stress relaxation on the lens, 3 different cases of stress relaxation functions were considered namely, the viscoelastic shear and viscoelastic bulk relaxation function, viscoelastic shear relaxation and elastic bulk, viscous shear relaxation and elastic bulk. The above relaxation functions are plotted against time as shown in Figure 1. For all the three cases studied, the relaxation times (τ_i) were adjusted such that the equilibrium viscosity (η) is maintained at a constant at value of log(10) Pa.s as per the following equation [19],

$$\frac{\eta}{G_0} = \sum_{i=1}^{n} w_i \tau_i .$$

(1)

The high temperature elastic modulus of the glass was numerically changed from its room temperature value (about 100 GPa) up to a lower value of 1GPa while keeping the equilibrium viscosity of the glass the same. This change is assumed to happen between 510°C and 560°C. This was done to understand the effect of elastic modulus on the lens shape deviation during mainly slow cooling and gap opening stages of lens molding.

The reference temperature (T_R) is the temperature of the glass at which all the viscoelastic properties of the glass are evaluated from the experiment. Based on the T_R and other parameters, the viscoelastic behavior of the glass over the entire temperature range can be calculated. Hence, it is critical to know this temperature (T_R) accurately. Given the uncertainties in determining the actual temperature of the glass during high temperature creep experiments, it is often difficult to

45

predict the reference temperature (T_R) accurately. In this study we consider the uncertainty of ±20°C in evaluating T_R and simulate its effect on the lens shape deviation. The uniform shift in T_R causes a subsequent uniform shift in the viscosity-temperature curve of the glass. This affects the thermal history of the molded lens causing change in the profile deviation. This shift also results in different press time (t_{pr}) as the "shifted glass" will have a different viscosity-temperature relationship. In this numerical experiment, the press time of lenses was adjusted to have the same center thickness for respective lens type. All other parameters were kept unchanged.

During actual molding process, the heat is transferred from lens to mold and surroundings via conduction, convection and radiation heat transfer mechanisms. As the lens is mainly cooled in nitrogen environment under forced convection, the convective heat transfer coefficient between the glass and the surroundings is introduced in the model at the end of gap creation stage when N_2 flows through the mold cavity. The same was not considered during the heating and pressing stage as it is believed that it would only affect the pressing time and not the shape change of the lens. Value of the film coefficient (h_f) and surrounding temperature (T_∞) was specified along the boundary of the lens and mold in the beginning of the fast cooling stage of the lens molding process. Such a lens would be cooled at a different rate due to the added heat transfer mechanism and is believed have a different shape deviation.

Three different levels details in of stress relaxation modeling are considered. The simple assumption involves use of a single Maxwell element for modeling response in shear and an elastic element for bulk response. This model requires knowledge of only the equilibrium viscosity at a reference temperature and it is similar to assuming the material behavior as viscous. The equation below gives the function form that can be used to show the response of this simple material,

$$G_1(t) = 2G_0 e^{-t/\tau} \qquad\qquad G_2(t) = 3K_0 \qquad\qquad (2)$$

Where 'τ' is relaxation time in shear and K_0 is the instantaneous bulk modulus of material.

Next, we considered a model involving multiple Maxwell elements for modeling response in shear and an elastic element for bulk response. The function form is given by,

$$G_1(t) = 2G_0 \sum_{i=1}^{n_1} w_i e^{-t/\tau i} \qquad\qquad G_2(t) = 3K_0 \qquad\qquad (3)$$

The most complex viscoelastic response was considered using multiple Maxwell elements for modeling both shear and bulk response. This response involved use of following function form,

$$G_1(t) = 2G_0 \sum_{i=1}^{n_1} w_i e^{-t/\tau i} \qquad\qquad G_2(t) = 3K_0 + (3K_\infty - 3K_0)\left(1 - \sum_{j=1}^{n_2} v_j e^{-t/\lambda j}\right) \quad (4)$$

Where, K_∞ is the equilibrium bulk modulus, w_i and v_j are the weighting factors for the deviatoric and volumetric relaxation functions, respectively, and τ_i and λ_j are the corresponding relaxation times for the deviatoric and volumetric relaxation functions.

3. RESULTS AND DISCUSSION

A. Convergence Study

Results in this study rely on the accurate prediction of final size and shape of molded lens and the residual stresses inside within the lens during and after molding operation. Convergence study of final size and shape of lens was previously considered by Ananthasayanam et al. [4]. A numerical convergence study of the stress state inside lens was performed to ensure these values

converge within certain tolerance limit. A steep meniscus lens shape was selected as this lens shape is expected to have a higher shape deviation and overall higher magnitude of residual stress distribution upon cooling. Also, this shape of lens is believed to have difficulty in compensating the shape deviation as result of molding. In this numerical study, a steep meniscus lens was subjected to complete thermo-mechanical cycle experienced by a typical lens during actual molding operation with the process parameters defined by Ananthasayanam et al. [4]. Frictional contact was assumed between the glass and mold interface with Coulomb's friction law. In-plane-principal stresses and out-of-plane principal stresses are evaluated at different intervals during the molding process. The study was conducted for three different meshes and a mesh with different value for parameter CETOL, which is a creep strain rate error tolerance defined in Abaqus that controls the accuracy of creep integration. Table 1 presents the convergence study results for Steep meniscus lens. It reports the percentage change in the value of maximum in-plane principal stresses, the time at which these stresses occur and also special coordinates inside lens at which these stresses occur during the important stage of lens molding. As seen from the table, the numbers are within acceptable limits for all stages except for the pressing stage. The stresses are very high at beginning of pressing and are difficult to converge due to the complex contact conditions involving hot glass and mold. Figure 1 shows the converged values of In-plane-principal stress distribution at a vertical section about 5 mm away from the axis of lens at different times during molding.

B. High temperature elastic modulus (E)

The Figures 2 and 5 shows the plot of lens shape deviation vs. high temperature elastic modulus for Bi-convex and Steep Meniscus lenses respectively. The deviation increases as the value of high temperature elastic modulus value drops below well its room temperature value. The change in deviation mainly occurs before and during gap creation stages. During slow

cooling stage, which precedes the gap creation stage, the pressing force is reduced to a maintenance force which is about 1/3 of the pressing force. The slow cooling stage is follow by a gap creation stage in which the maintenance force drops completely to zero. Lower value of elastic modulus causes a higher mechanical strain and deformations during stages when the magnitude of applied force drops to zero. This can also induces a higher stress state in the lens resulting in the higher lens shape deviation of lens.

C. Reference temperature (T_R)

The Figures 3 and 6 shows the effect of reference temperature on the deviation for both types of lenses. As expected the shape deviation changes as the value of T_R is perturbed by ±20°C. The lens press time is changed for each case as shown in Figure. It takes longer to press the lens with higher T_R, keeping other parameters including the heat transfer coefficient at the lens and mold interface unchanged. This happens because the temperature at which the lens is molded also increases with higher T_R. Since the lens molded with different T_R has different thermal history, the deviation of such a lens will be different. Thus when T_R was changed by +20°C, the molding temperature rises causing change in shape deviation, about 2 microns for Bi-convex and, about 4 microns for steep meniscus. While lowering the T_R by 20°C lowers the deviation, by about a micron for Bi-convex and, by about 2 microns for Steep meniscus. During stress relaxation experiment, the actual temperature of the glass is less than the temperature recorded by the thermocouple, thus value of T_R is usually underestimated.

D. Convective heat transfer coefficient (h_{conv})

Figures 4 and 7 show the lens shape deviation for different convective heat transfer coefficients considered. The effect of modeling convective heat transfer is to increase the rate of heat transfer from the lens, consequently cooling it faster than before. As lens cools faster, the

equilibrium liquid gets less time to accommodate for shape change due to structural rearrangements resulting in increase in deviation. The change in deviation is calculated based on deviation of the baseline case with $h_{conv}= 0$. For higher heat transfer coefficient ($h_{conv}= 200W/m^2K$), the change in deviation is about 15 microns for Bi-convex while about 44 microns for Steep meniscus lens. When a relatively low value of coefficient is used ($h_{conv} = 20W/m^2K$), the change in deviation for both types of lenses is less than 2 microns.

E. Stress relaxation

It was previously determined that the choice of stress relaxation functions has a negligible effect on the lens shape deviation, but the effect on the residual stresses was believed to be significant. Figures 8 and 9 shows the plots of in-plane principal stress at section 5 mm away from axis within the respective lens at different time intervals during lens molding. As seen from the figure, as the complexity of material model increases, the stresses inside lens drop to a lower values. The estimate of residual stresses inside lens at the end of process could off significantly if the simplified assumption regarding the material model are made in the analysis.

4. CONCLUSIONS

Following conclusions are made based on the current sensitivity study of two lens types.

1. It is important to know the high temperature elastic modulus $E(T)$ of optical glass as it has a significant impact on the lens shape deviation for both types of lenses. In general, the lower the value of E, higher the residual stresses and deviation. This conclusion is important for certain types of optical glasses including Chalcogenides which have a low value of E at temperatures above Tg.

2. The change in reference temperature causes a non-negligible change in deviation of both types of lenses keeping other parameters the same except the pressing time.

Lower the TR, lower is the press time and the deviation of a lens. Simulations suggest that if T_R is within 20$^\text{o}$C of the actual value, the change in deviation is about less than a micron for Bi-convex and, about -2μm for Steep meniscus lens.

3.   Considering the mechanism of convective heat transfer between the glass and mold at end of slow cooling stage affects the thermal history of the lens. The effect is increases in the deviation of lens as lens cools faster than before. Thus it is important to consider convective heat transfer coefficient in order to predict the lens shape change during lens molding.

4.   The lens shape deviation for both types of lenses is not sensitive to the viscoelastic stress relaxation function. Viscoelastic behavior of the optical glass during molding can be simplified by assuming that material has a viscous response in shear and elastic response in bulk. However, this assumption will lead to an overestimation of residual stresses inside the lens.

REFERENCES:
1. D. Joshi, P. Mosaddegh, J.D. Musgraves, K.C. Richardson, P.F. Joseph, "Thermo-Mechanical Characterization of Glass at High Temperature Using the Cylinder Compression Test: Part I – Viscoelasticity, Friction and PPV," accepted for publication in the Journal of Rheology, July 9, 2013.
2. D. Joshi, P. Mosaddegh, J.D. Musgraves, K.C. Richardson, P.F. Joseph, "Thermo-Mechanical Characterization of Glass at High Temperature Using the Cylinder Compression Test: Part II – No-Slip Experiments, Viscoelastic Constants and Sensitivity," accepted for publication in the Journal of Rheology, July 9, 2013.
3. B. Ananthasayanam, P F Joseph, D. Joshi, S. Gaylord, L. Petit, V Y Blouin, K C Richardson, D. Cler, M. Stairiker, M. Tardiff, Final shape of Precision molded optics: Part I -

Computational approach, material definitions and effect of lens shape. Journal of Thermal stresses, 35, (2012) pp.550-578.

4. B. Ananthasayanam, P F Joseph, D. Joshi, S. Gaylord, L. Petit, V Y Blouin, K C Richardson, D. Cler, M. Stairiker, M. Tardiff, Final shape of Precision molded optics: Part II - Validation and sensitivity to material properties and process parameters. Journal of Thermal stresses, 35, (2012), pp.614-636.

5. A. Y. Yi, A. Jain, Compression Molding of Aspherical Glass Lenses-A combined Experimental and Numerical Analysis, J. Am. Ceram. Soc., **88** (2005), pp. 579-586.

6. M. Sellier, C. Breitbach, H. Loch and N. Siedow, An iterative algorithm for optimal mould design in high-precision compression moulding. Proc. IMechE Vol. **221** Part B: J. Engineering Manufacture, pp 25-33.

7. F. Wang, Y. Chen, F. Klocke, G. Pongs and A. Yi, Numerical Simulation Assisted Curve Compensation in Compression Molding of High Precision Aspherical glass Lenses. Journal of Manufacturing Science and Engineering, 131, Feb 2009, Issue 1, 011014 (6 pages).

8. Y-C Tsai, C Hung, J-C Hung,H-F Tseng, Finite element prediction of the lens shape of moulded optical glass lenses, Proc. IMechE, Part B: Journal of Engineering Manufacture, **225**,2011, pp. 224-234.

9. M. Arai, Y. Kato, and T. Kodera, Characterization of the thermo-viscoelastic property of glass and numerical simulation of the press molding of glass lens. J of Therm. Stresses, **32**, 2009, pp. 1235-1255.

10. S. H. Chang, Y. M. Lee, T. S. Jung, J. J. Kang, S. K. Hong, G. H. Shin, Y. M. Heo, Simulation of an aspheric glass lens forming behavior in progressive GMP process, AIP Conf. Proc. 908 pp.105-1060 (2007)

11. J. Yan, T. Zhou, J. Masuda, T. Kuriyagawa, Modeling high-temperature glass molding process by coupling heat transfer and viscous deformation analysis. Precision Engineering, 33, 2009, pp. 150-159.

12. T. Zhou, J. Yan,J. Masuda, and T. Kuriyagawa, Investigation on the viscoelasticity of optical glass in ultra precision lens molding process. J of Mat. Process Tech., **209**, 2009, pp. 4484-4489.

13. B. Ananthasayanam, P F Joseph, D. Joshi, S. Gaylord, L. Petit, V Y Blouin, K C Richardson, D. Cler, M. Stairiker, M. Tardiff, Final shape of Precision molded optics: Part I - Computational approach, material definitions and effect of lens shape. Journal of Thermal stresses (in press)

14. B. Ananthasayanam, P F Joseph, D. Joshi, S. Gaylord, L. Petit, V Y Blouin, K C Richardson, D. Cler, M. Stairiker, M. Tardiff, Final shape of Precision molded optics: Part II - Validation and sensitivity to material properties and process parameters. Journal of Thermal stresses (in press)

15. F. Klocke, F. Wang, Y. Wang, G. Liu, O. Dambon, A.Y. Yi, "Development of a flexible and reliable numerical simulation for precision glass molding of complex glass optics", 6th International Symposium on Advanced optical Manufacturing and Testing Technologies, Proc. Of SPIE, 8416,841603-1, (2013)

16. L. Duffrene, R. Gy, H. Burlet, and R. Piques, Multiaxial linear viscoelastic behavior of soda-lime-silica glass based on a generalized Maxwell model. Soc. Rheol., **41**, 1997, pp. 1021-1038.

17. H. Loch, D. Krause, Mathematical simulation of glass technology, Springer, New York, 2002.

18. T. Rouxel, Journal of American Ceramic Society, 90 [10] 3019-3039, 2007.

19. Scherer, G. Relaxation in glass and composites. John Wiley and Sons, New York, 1986

Table for Lens Molding Paper:

Molding Stage	% change in maximum value of in-plane principal stresses	% change in time at which the maximum stresses occur	% change in geometric location where the maximum stresses occur (co-ordinates)	
			X	Y
Pressing	13.7	79.9	-6.51	-0.01
Slow Cooling	3.97	0	-0.07	-0.18
Gap creation	3.97	0	-0.07	-0.18
Cooling #2	0.26	0	0	-0.29
Release	0.24	0	0	-0.73
Cooling #3	0.43	0	0	0.61
Cooling #4	-0.69	2.97	0	-0.30

Table 1. Convergence study of steep meniscus lens for maximum value of In-plane principal stresses inside lens during different stages of lens molding. Two additional convergence criterion considered include time at which the maximum stresses occur and its geometric location inside lens. Values indicate percentage change of refined mesh (20,499 elements) values relative to the baseline mesh (13,641 elements) values.

Figures for Lens Molding paper:
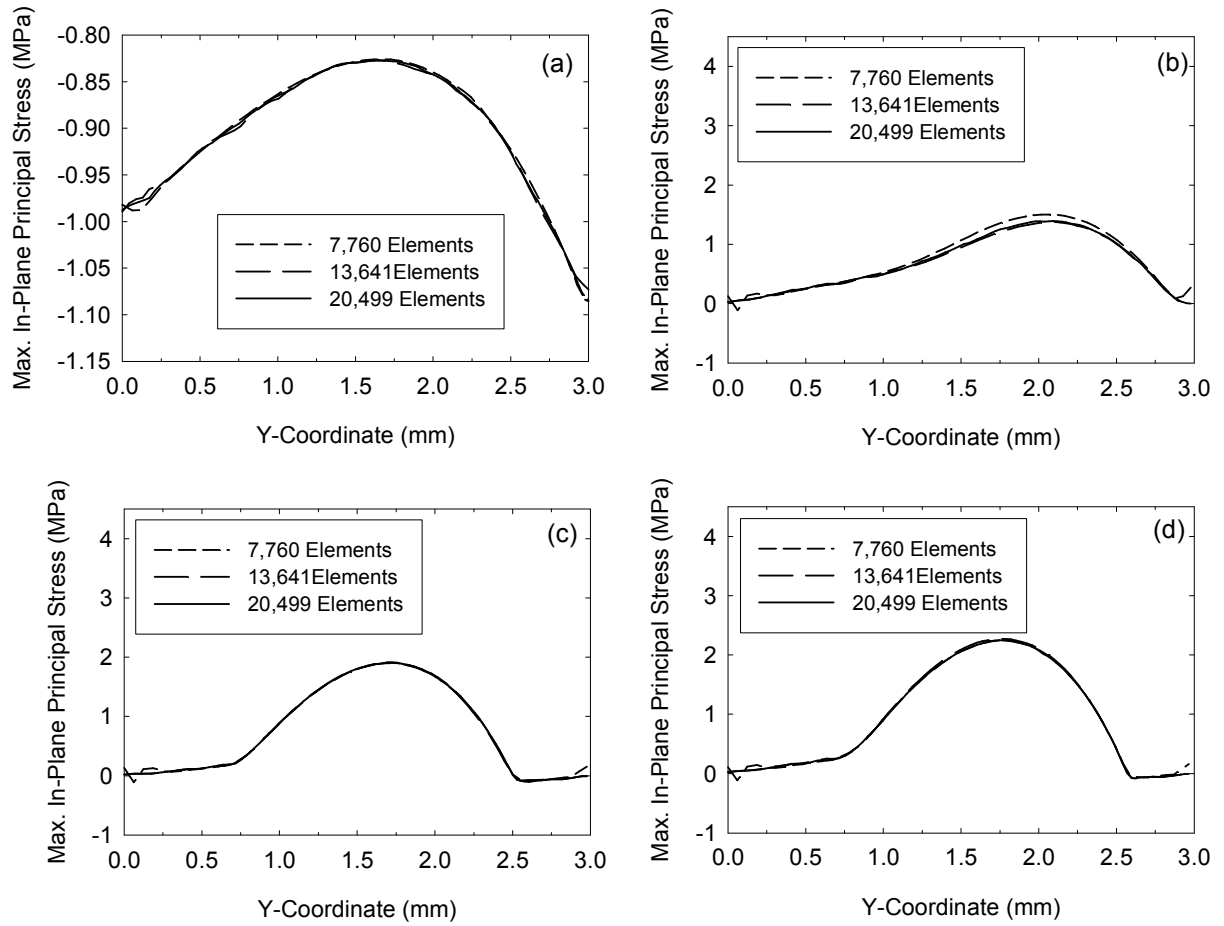
Figure 1. Convergence of In-Plane principal stresses at a vertical section 5 mm away from central axis of the steep meniscus lens for different meshes and different molding stages considered. (a) End of Pressing, (b) End of Slow Cooling, (c) End of Gap creation, (d) End of Process.
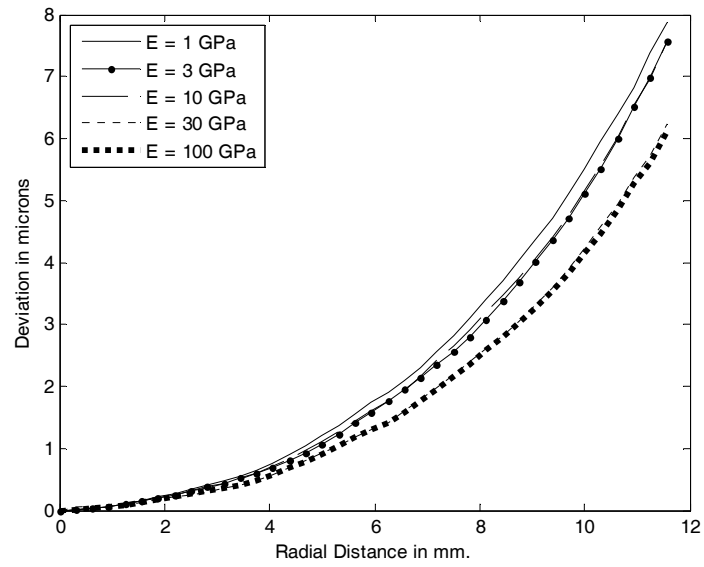
Figure 2. Bi-Convex: Effect of E
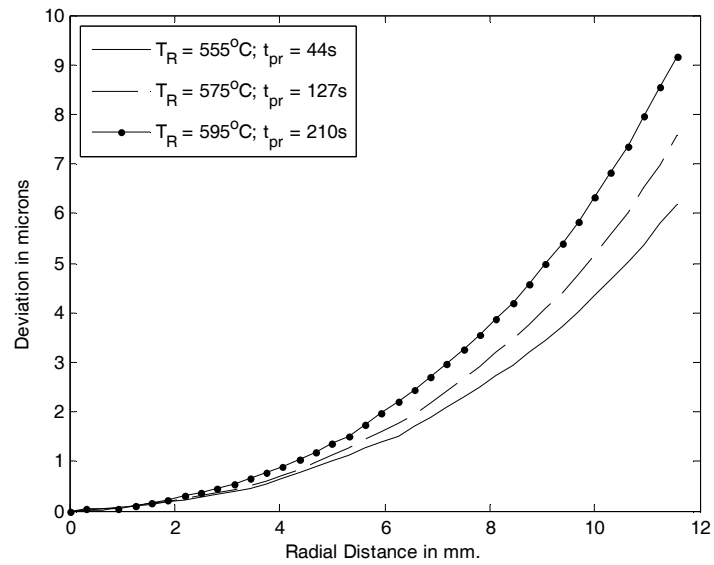
Figure 3. Bi-Convex: Effect of Tr

56
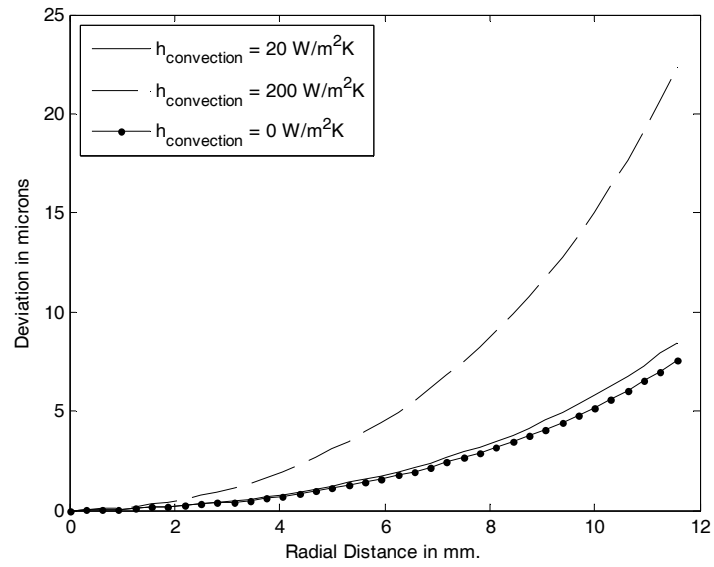
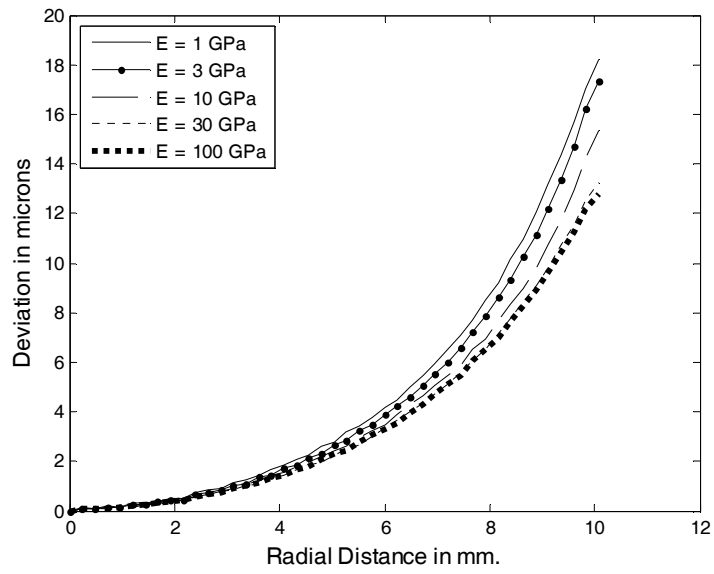Figure 4. Bi-Convex: Effect of convective coefficient (h_{conv})

Figure 5. Steep meniscus: Effect of E
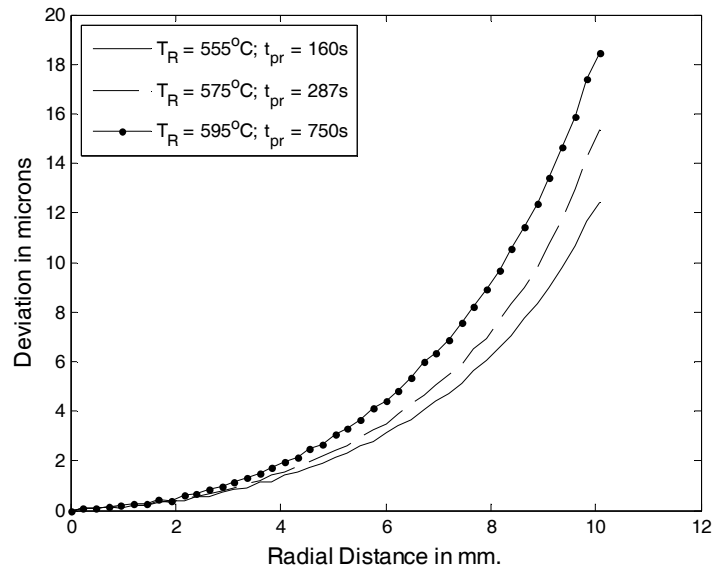
Figure 6. Steep Meniscus: Effect of Tr.
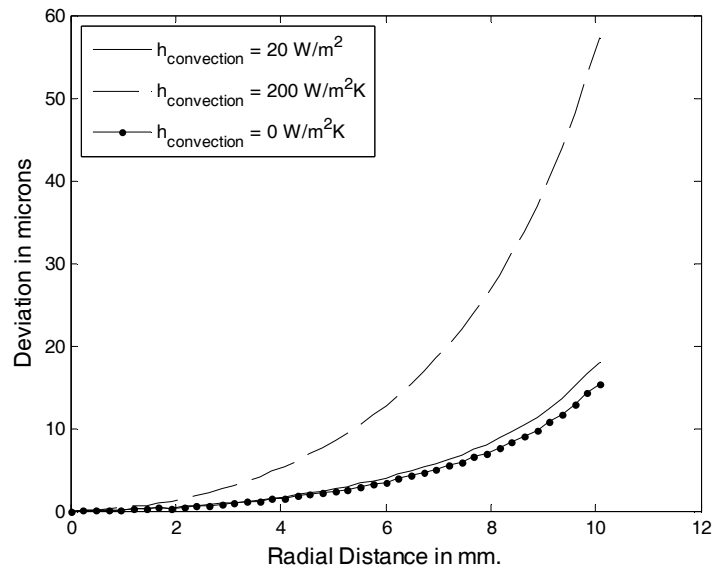
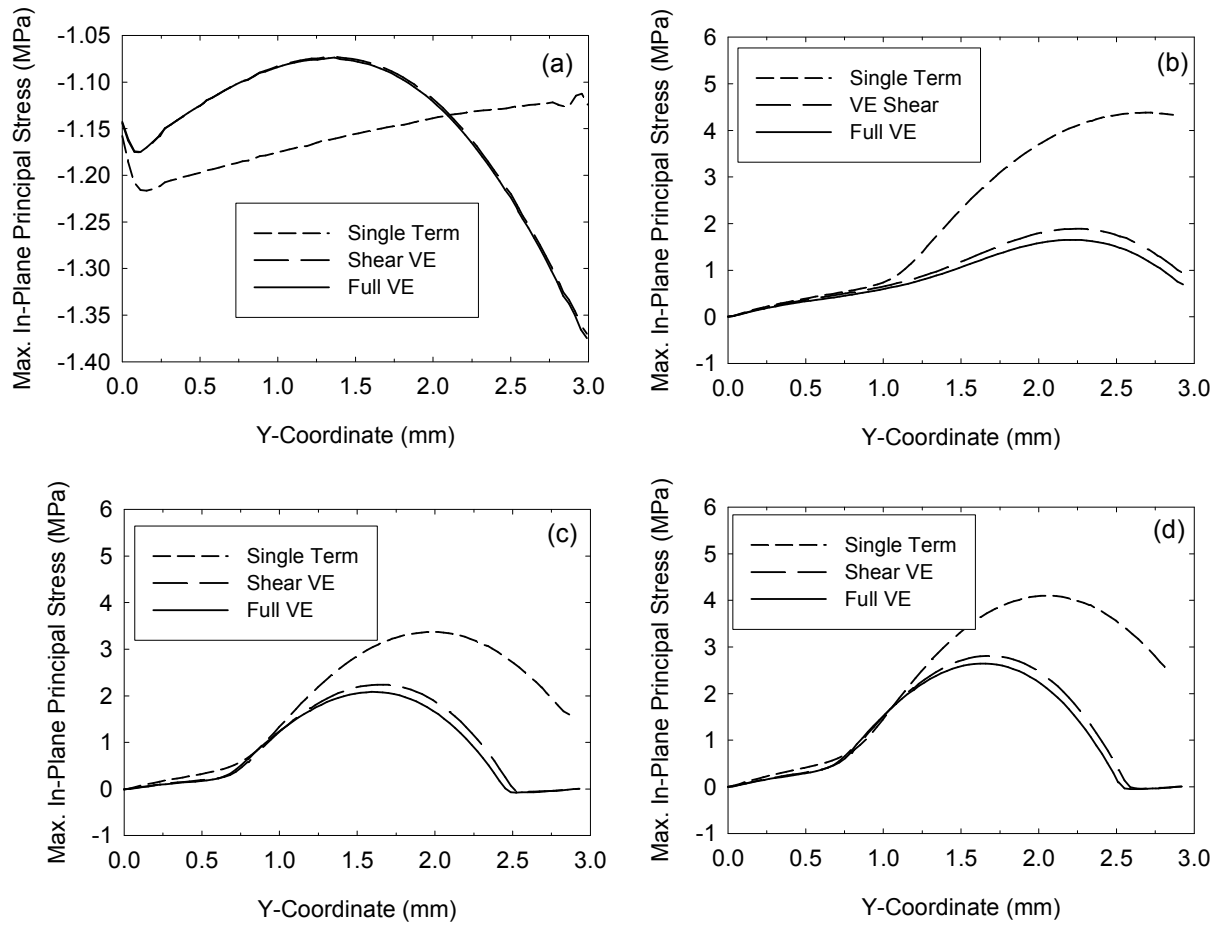Figure 7. Steep Meniscus: Effect of convective coefficient h_{conv}
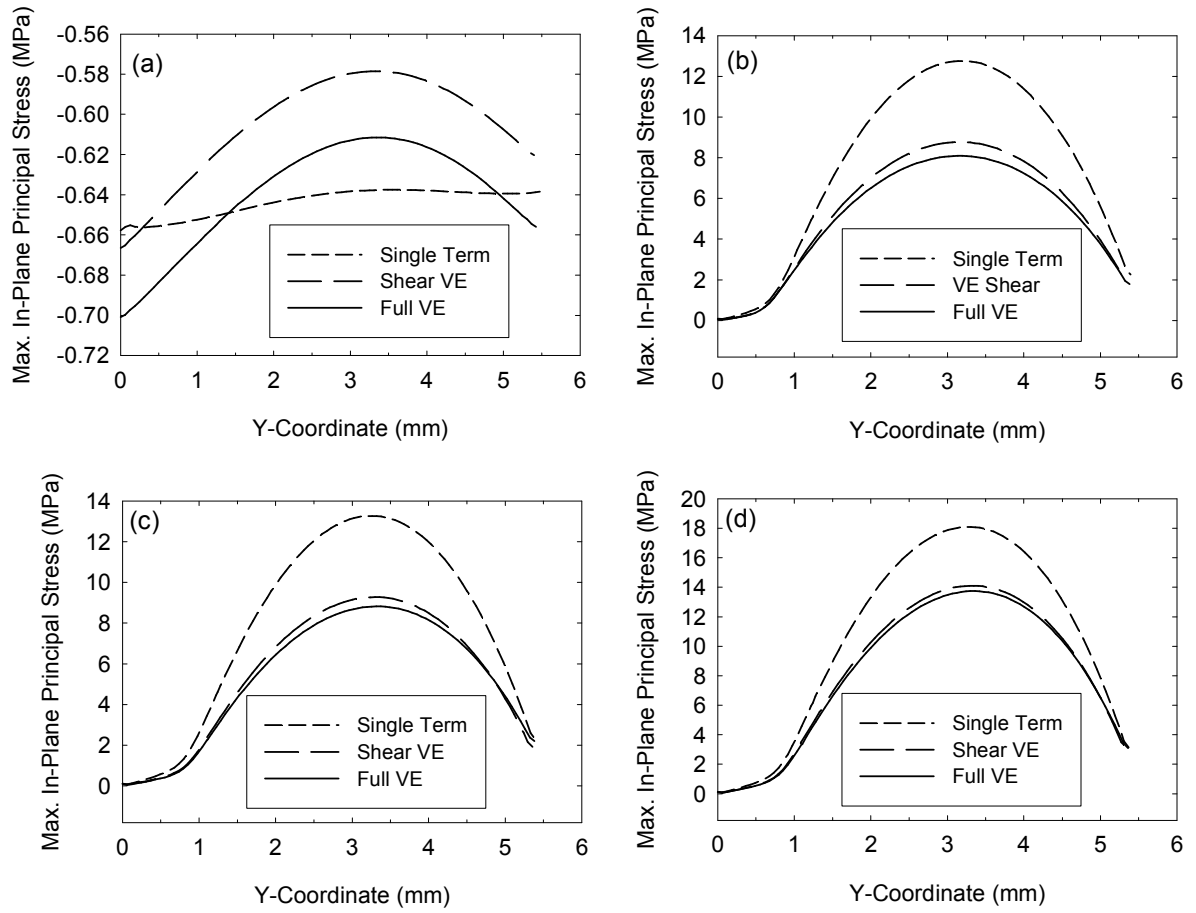
Figure 8. Bi-Convex: Effect of Stress relaxation modeling detail on stress state at a vertical section 5 mm away from central axis. (a) End of Pressing, (b) End of Slow Cooling, (c) End of Gap creation, (d) End of Process.

Figure 9. Steep Meniscus: Effect of Stress relaxation modeling detail on stress state at a vertical section 5 mm away from central axis. (a) End of Pressing, (b) End of Slow Cooling, (c) End of Gap creation, (d) End of Process.

Appendix C2. (Paper DRAFT)

Prediction of Die Swell of Extruded Glass Preforms at High Viscosity

Mohamed Trabelssi[1], Heike Ebendorff-Heidepriem[2], Kathleen C. Richardson[3,4], Tanya Monro[2] and Paul F. Joseph[1*]

[1]Department of Mechanical Engineering, Clemson University, Clemson, SC 29634-0921, USA
[2]Institute of Photonics and Advanced Sensing, School of Chemistry and Physics, The University of Adelaide, Adelaide, SA5005, Australia
[3]Department of Materials Science and Engineering, COMSET, Clemson University, Clemson, SC
[4]currently at the College of Optics and Photonics, University of Central Florida, Orlando, FL 32816, USA
   *Corresponding author, jpaul@clemson.edu, Phone: 864-656-0545, Fax: 864-656-443

Abstract. Computational simulations of glass extrusion are performed to quantify the effects of material behavior and slip at the die/glass interface on the die swell. Experimental data for three glass types are used to guide the computational study, which considers glass material to be viscous with and without shear thinning and viscoelastic using the Maxwell upper convected model. The study starts with assuming no-slip at the glass/die interface in order to see if material behavior alone can explain the die swell results, and then considers slip using the Navier model where interface shear is directly proportional to the relative slip speed at the interface. Consistent with the possibility of slip and intended high viscosity applications, viscosity ranging from $10^{7.4}$ to $10^{8.8}$ Pa·s was used. Based on optimization of the various input parameters required to achieve the measured die swell and ram force values, the study concludes that interface slip occurred since only extreme values of the shear thinning parameters provided an alternative.

Introduction

Extrusion is a widely spread manufacturing process for making glass and polymer preforms that can be used to make optical fibers. While polymers are the material of choice for many applications, there are applications where the use of specific glasses is required to achieve targeted optical properties. Microstructured Optical Fibers (MOF), which have complex geometrical patterns of holes in the cross section, are an important example[1-3]. To achieve the desired preform structure and excellent optical quality (in order to achieve ultimately low-loss optical fibers), use of high viscosity combined with low speed is essential. The typical viscosity range is from 10^7 - 10^9 Pa·s, while the ram speed is reduced to values like 0.5 mm/min and smaller. Additional examples of glass preforms that require high viscosity extrusion have been provided[4-6].

Extrusion closer to the glass transition temperature introduces the possibility of two interesting aspects that affect cross sectional distortion: viscoelastic glass behavior and glass/die interface slip. Evidence that slip occurs in this viscosity range was provided for L-BAL35 glass at a viscosity of $10^{8.3}$ Pa·s pressed on a tungsten mold with a diamond like carbon coating[7]. The ring compression test was used to quantify a very low coefficient of Coulomb friction of 0.05. While interface slip and viscoelastic material behavior are common in studies of Precision Glass Molding[8-10], most glass extrusion studies apply the no-slip boundary condition appropriate at higher temperature[11,12]. Exceptions include the important contribution by Egel-Hess and Roeder[13] who studied die swell both experimentally and computationally at a viscosity of $10^{7.05}$ Pa·s. Die swell is important in extrusion applications as it is global evidence of the deformation mechanisms that cause cross sectional distortion. These authors concluded that for some die

materials interface slip must occur, while the choice of glass composition had no influence on friction. An approximate method based on an inputted wall slipping velocity at the die exit was used to quantify the effect of friction. In another study of die swell for non-circular cross sections[14] both no-slip and full slip were implemented into a computational scheme for a viscosity of $10^{6.86}$ Pa·s.

Ebendorff-Heidepriem and Monro[15] presented a detailed experimental and analytical study of the basic assumptions used to estimate ram speed, applied ram force and viscosity in the range of 10^7 to 10^9 Pa·s for extruded solid glass preforms. The study included several experimental results, accounts for interface slip and showed several linear correlations of a number of extrusion variables. While these assumptions appear to oversimplify the problem, the results show reasonable agreement with viscosity estimations in the literature. In this study several assumptions made by Y. Yue et al.[11] were applied even though the range of viscosity was considerably higher.

While there have not been many die swell computational studies for glass that involve viscoelasticity and/or interface slip, such studies are common in the polymer literature. For example, there have been die swell studies that use a no-slip boundary condition with viscoelastic material behavior[16-18] and studies with slip[19,20]. The importance of interface slip in the polymer literature is evident in the review paper by Hatzikiriakos[21], which includes the review of various slip models.

In the current combined computational and experimental study of extrusion of high viscosity glass, the most basic modeling assumptions were used to understand the primary reasons for

die swell. This includes material behavior of viscous, upper convective Maxwell model to account for viscoelastic behavior and shear thinning using the Cross law. In addition, the ram speed is considered as a processing parameter, while behavior at the glass/mold interface condition takes into account no-slip and slip making use of the linear form of the Navier law. By comparing results to experimental data within the context of realistic values of the material parameters, conclusions about the validity and importance of these assumptions are made that are specific to glass extrusion at high viscosity.

Governing equations

In the Eulerian framework the governing equations for steady state, axisymmetric, incompressible flow are given by the continuity and conservation of momentum equations as follows:

$$\nabla \cdot u = 0 \tag{1}$$

$$\nabla \cdot \left(\eta \nabla u \right) - \nabla p + f = 0 \tag{2}$$

where $u = u(r, z)$ is the velocity vector in cylindrical coordinates, $T = \eta \nabla u$ is the deviatoric stress tensor, η is the shear viscosity, p is the pressure and f represents the body force terms. Inertial forces are neglected due to the low rates of deformation. When the viscosity is constant Eqn. (2) simplifies to

$$\eta \nabla^2 u - \nabla p + f = 0 \tag{3}$$

The equations for both constant viscosity and shear thinning viscosity are solved using the ANSYS software, POLYFLOW.

Die geometry

The experimental data where obtained from extrusions of three different glasses under various conditions of viscosity (temperature) and ram speeds. The die used in this process has a geometric composition similar to the one shown in Figure 1[15]. The die shape is composed of three compartments:

- The feeding chamber, which is a reservoir-like compartment where the glass billet is pressed. This part is included in the computational domain with sufficient length for the flow to reorganize before reaching the next chamber. Its length does not have a significant influence on the die swell results.

- The second compartment is referred to as the Interface (or funnel) in Figure 1, which links the feeding chamber to the channel. While not always present in a die[14,15], this transition region is important in this specific extrusion process. Its shape is chosen to reduce the risk of failure, such as poor surface quality, or preserve a more homogenous stress state within the glass. In this case the shape of the interface is tangent to the channel and non-perpendicular to the feeding chamber.

- The Die Channel, which is the most basic component in the die, is the region where the flow profile is shaped before the glass reaches the exit.

Boundary conditions

Boundary conditions for this problem are specified on the four surfaces identified in Figure 1, which are defined as the Inflow, Outflow, Free surface and Die/Glass interface regions. At the Inflow region the volume flow rate is specified and the radial component of velocity is zero. Both parabolic and uniform velocity profiles were used at the die entrance ($z = -L_d$), leading to the conclusion that the details of the flow profile at the die entrance had negligible effect on the die swell. A parabolic profile was used due to improved convergence. At the Outflow region, which is taken far enough downstream to achieve a steady state solution, the shear stress is zero and the normal stress is zero in the absence of gravity. On the Free Surface region the glass is free of stress. Finally, at the Die/Glass interface, for the no-slip condition, the velocity is zero, while for the slipping, the normal component of velocity is zero and the tangential component obeys the friction law.

Experimental die swell data

Die swell and ram force data was obtained for five cases of extrusion performed using F2, Bismuth and Tellurite glasses. The die material was stainless steel grade 303. As presented in Table 1, the selected glass fiber preforms were extruded at relatively high viscosity ranging from $10^{7.4}$ to $10^{8.8}$ Pa·s, while the ram speed ranged from 0.5 to 0.2 mm/min, which corresponds to a volume flow rate of 6.1 to 2.4 mm^3/s. Experimental observations indicate that for log of viscosity/(Pa·s) of 7.5 or lower, the preform diameter decreases in the course of extrusion due to effect of gravity. This preform tapering effect can significantly affect the determination of die swell from the measured preform diameter. For log viscosity/(Pa·s) = 8.5 or greater, no tapering of extruded rods was observed. To avoid the impact of gravity, the experimental die swell values

were measured as the preform diameter 10-30 mm from the end of the preform that was

extruded first, where effect of gravity is negligible. The glass extrusion conditions were

experimentally determined to be very similar for the three glass types, but F2 glass was also

extruded at higher ram speed at lower viscosity. Experimentally, the extrusion parameters are

selected to avoid extrusion failure which includes low preform surface quality (sharkskin

surface) or in severe cases a corkscrew preform shape. Details of the experimental procedure

are presented by Ebendorff-Heidepriem and Monro[15]. The primary cause for error in the

measurements was temperature uncertainty of ±3 °C, which had a direct effect on the viscosity,

which in turn affected the ram force and the die swell.

Table1: Experimental process parameters and measured values of extruded preform diameter and ram force.

Case	Glass	Ram speed (mm/min)	Billet Diameter (mm)	Die exit Diameter (mm)	Log viscosity (Pa·s)	Extruded preform diameter (mm)	Force (kN)
1	F2	0.5	30.5	10.2	7.4 (555 °C)	11.0±0.2	6.8
2	F2	0.2	30.5	10.2	8.1 (529 °C)	11.0±0.2	14
3	F2	0.2	30.5	10.2	8.6 (509 °C)	11.0±0.2	67
4	Bismuth	0.2	30	10.2	8.8 (460 °C)	10.4±0.2	26
5	Tellurite	0.2	30	10.2	8.8 (342 °C)	10.5±0.2	25

Mesh presentation and convergence

Mesh convergence studies were performed by running simulations for fourteen mesh

configurations for a viscous glass extruded through the reference die. Though the reference die

had a relatively complex geometry, it was meshed entirely with rectangular elements.

Refinement was only necessary near the die exit. The meshes were characterized by two

parameters: the minimum mesh size and the refinement coefficient, as provided by the

software ANSYS. Combinations of these parameters for each mesh were compared to those of

the reference mesh which had the highest density of elements and refinement. The details of

the fourteen different meshes used in this mesh convergence study are given in Table 2. The

reference mesh is designated as M5.2 in this table.

The die swell profile was chosen as the primary convergence criterion since it is the most basic

measurable outcome of the simulations. In addition, variables related to the velocity and

pressure distribution along the centerline were also considered.

Table2: Mesh configuration definitions performed on Case 1 in Table 1 (log viscosity = 7.7 Pa·s,
ram speed = 0.5 mm/min).

Mesh nomenclature	Refinement coefficient (respective values for meshes on the left)	Minimum mesh size (mm)	Number of Elements	Number of Nodes
M1.0, M1.1 M1.2	2,5,8	0.6	1113	1218
M2.0, M2.1 M2.2	2,5,8	0.4	2431	2587
M3.0, M3.1 M3.2	2,5,8	0.2	9411	9719
M4.0, M4.1, M4.2,	2,5,8	0.12	26141	26652

| M5.1, M5.2 | | 5,8 | 0.09 | 46121 | 46800 |

The extrusion parameters for Case 1 in Table 1 were used to determine the steady state die swell for each of the fourteen mesh configurations presented in Table 2. This case has the lowest viscosity and the highest ram-speed. The die swell results are presented in Table 3 both as absolute values and as percent error when compared to the results from the densest mesh. The data in this table indicate that most of the mesh setups perform similarly, with all but M1.0 agreeing to the first digit.

Table3: Mesh convergence study of the die swell radius.

Mesh	M1.0, M1.1, M1.2	M2.0, M2.1, M2.2	M3.0, M3.1, M3.2	M4.0, M4.1, M4.2	M5.1, M5.2
Die swell radius (mm)	5.80834	5.79003	5.77074	5.76211	
	5.78417	5.77332	5.76163	5.75642	5.7527
	5.77511	5.76704	5.7582	5.75423	5.75437
Percent error as compared to results of M5.2.	8.524	5.719	2.763	1.441	
	4.821	3.159	1.368	0.569	0.255
	3.433	2.197	0.842	0.234	---

The trend of the results in Table 3 shows that convergence improves by increasing the refinement coefficient as well as increasing the number of elements, although increasing the refinement coefficient is more effective. Evidence that the results have nearly converged is seen by comparing M3.1 to M4.0, where a small adjustment in the refinement coefficient gives the better result but the deviation is greater than 1%. Another example of the benefits of

refinement is shown by comparing the M4.2 and M5.1 results. Based on the die swell results, which are also presented in Figure 2 for the entire length of the preform, the optimum mesh is M3.2 since it is has less than 1% deviation and uses the fewest elements. Before final selection of this mesh the behaviors of the pressure and velocity along the centerline were also considered. These results showed that in general the variations of these quantities for the best meshes have good agreement; however, the location of the maximum value of the velocity was the most sensitive to mesh since, as shown in Figure 3, the maximum occurs near the die exit. A detailed investigation of this behavior narrowed the choice to M3.2 over M4.1, although the difference was not significant. To conclude, the mesh, M3.2, gives good agreement with die swell as well as the pressure and velocity along the centerline, and thus was selected for the simulations.

Results

Viscous material behavior

In this section the viscous material model with a no-slip boundary condition is used to compare the predicted die swell with the experimental data for the four test cases. A summary of the results is presented in Table 4. Most notable is that the predicted die swell values for this model are independent of the flow rate and viscosity [13]. Furthermore, the numerical simulations overestimated the die swell in all cases, especially for the cases of Bismuth and Tellurite. For the case of F2 glass, though the die swell is again over-predicted, it is better than the other predictions by a factor of two. The differences between the data and the predictions are large enough to discard the possibility of computational error as the explanation.

Table 4: Die Swell results for viscous material behavior with no-slip boundary condition.

Case	Ram speed (mm/min)	Flow rate (mm³/s)	Log of viscosity/(Pa·s)	Extruded preform diameter (mm)	
				Data	Numerical
1	0.5	6.088	7.4	11.0±0.2	11.516
2	0.2	2.435	8.1	11.0±0.2	11.516
3	0.2	2.435	8.6	11.0±0.2	11.516
4	0.2	2.356	8.8	10.4±0.2	11.523
5	0.2	2.356	8.8	10.5±0.2	11.523

The presented cases cover a considerable range of flow rate and a variety of viscosities; however these variations had no impact on the numerical outcome. It is therefore apparent from the data and these numerical results that an inappropriate material model was used and/or the assumption of a no slip boundary condition is incorrect.

Time dependent material behavior

The viscous assumption neglects the time dependent response introduced by viscoelastic material behavior and is justified when the extrusion process is extremely slow or the glass is at a temperature above the transition temperature range, where glass behavior transitions from that of an elastic solid to a viscous fluid[22]. Given that the interest in this study is high viscosity extrusion at a temperature within this range, the possibility of viscoelastic material behavior should be considered, especially since the viscous assumption failed to describe the outcome of the experimental data. To determine the impact of this model adjustment the five study cases are considered using the Maxwell upper convected model[23], which is presented below:

$$T + \lambda \overset{\triangledown}{T} = 2\eta D \,,$$

(4)

where T is the deviatoric stress tensor, λ is the relaxation time, D is the tensor of the

deformation rate, $\overset{\triangledown}{T}$ is the upper-convected time derivative of T defined as

$$\overset{\triangledown}{T} = \frac{\partial T}{\partial t} + u \cdot \nabla T - \left[\left(\nabla u \right)^{T} \cdot T + T \cdot \left(\nabla u \right) \right] \,.$$

(5)

Table 5 shows die swell results for five relaxation times ($\lambda = \eta/G$) for each of the four

experimental data sets. Table 4 provides the $\lambda = 0$ limiting case of the viscoelastic solution. It is

important to note that another mesh convergence study was conducted for viscoelastic material

behavior.

The results in Table 5 show an initial decrease of the die swell as the relaxation times, λ,

increases, followed by an increase in the die swell and the computational solution captures the

complexity of the response. In order to understand this, as the relaxation time increases from

zero, a recoverable elastic contribution to the stress occurs within the glass. If the relaxation

time is high, this stress does not have time to relax until the flow emerges from the die exit

which increases the die swell. However, if the relaxation time is low, it appears that there is time

for the stress to relax and cause a rearrangement while still in the channel which causes a slight

reduction in the die swell. Realistic values of the relaxation time for viscosity in the range of $10^{7.4}$

$- 10^{9}$ Pa·s are less than unity since the shear modulus is larger than 1 GPa[24]. Therefore, while the

numerical solution shows that die swell can increase for large relaxation times, in the physical

range of material behavior there is a small decrease, which is too small to explain the

experimental results.

Table 5: Die Swell results for viscoelastic material behavior with no-slip boundary condition.

Case	Ram speed (mm/min)	Log viscosity (Pa·s)	Extruded preform diameter (mm)						
			Data	Numerical				
				$\lambda = 0.1$	$\lambda = 1$	$\lambda = 5$	$\lambda = 10$	$\lambda = 20$
1	0.5	7.4	11.0±0.2	11.500	11.460	11.520	11.900	13.160
2	0.2	8.1	11.0±0.2	11.500	11.480	11.440	11.460	11.720
3	0.2	8.6	11.0±0.2	11.501	11.480	11.433	11.467	11.723
4	0.2	8.8	10.4±0.2	11.502	11.481	11.433	11.462	11.700
5	0.2	8.8	10.5±0.2	11.502	11.481	11.433	11.462	11.700

From these results the time dependence of the material behavior makes the result more

sensitive to the process parameters. However, this sensitivity does not produce the correct die

swell results observed in the experimental data as the die swell is still over estimated by the

model.

Shear thinning

The possibility of using a shear thinning model to target the measured die swell was considered

even though the numerical data indicates that the maximum shear rate in the experiments is

very low for such behavior. To illustrate this point, an optimization process was used to adjust

the material properties for a glass with shear thinning to fit the experimental value of the

preform diameter. The Cross law[25,26] was chosen for this task due to its simplicity and limited number of parameters, which is presented below

$$\eta = \frac{\eta_0}{1 + (\lambda\dot{\gamma})^m} \ ,$$

(4)

where η_0 is the equilibrium viscosity of the glass, $\dot{\gamma}$ is the rate of shear strain and m and λ are model parameters. Written in this form the exponent m can be used as a measure of nonlinearity; the closer this coefficient to 1 the higher the degree of nonlinearity. From a material behavior perspective a high m means that the material viscosity decreases rapidly for a small increase of the local shear rate. This behavior is bounded in the shear rate domain by constant λ, which defines the value at which the shear rate starts to affect the viscosity. As the λ parameter increases, the viscosity becomes sensitive to shear rate at a lower value of the shear rate. Because of this, for very high values of λ the nominal viscosity η_0 is difficult to measure.

To perform the task of optimization, a number of shear thinning glass property configurations were considered. First a value of λ was selected and then an optimizer was coupled with POLYFOW to search for the corresponding value of m required to achieve the experimental value of the die swell. This task was carried out for the Tellurite example, which is Case 5 in Table 1. The results of the optimizer are shown in Table 6 and Figure 5. For the three cases presented in Figure 5, the velocity profiles are presented in Figure 6. The results in Figure 7 show the viscosity distributions in the die channel for the two extreme cases considered in Table 6 (m = 0.95, λ = 100) and (m = 0.63, λ = 4000). The regions are defined as a range of percentage of η_0. These results indicate a very high degree of shear thinning, especially for the case when λ

= 4000. The results in Figure 8 summarize the variation in viscosity throughout the die and the

channel for all the cases in Table 6. In these figures the x-axis represents the viscosity

normalized by the nominal viscosity η_0, while the y-axis represents the percentage of the

volume of glass that has a viscosity greater than η/η_0. The closer this is to 100%, the less the

effect of shear thinning. The figure on the right, which accounts for just the volume of glass in

the channel, shows more extreme results since there is no stagnation region.

The results presented in Table 6 indicate a high degree of nonlinearity since the m parameter is

greater than 0.6 for a wide range of the λ parameter. In order to better appreciate this degree

of nonlinearity, a constant "apparent" viscosity can be defined which requires the same ram

force as that obtained using the Cross law. Based on the linear relationship between the ram

force and the viscosity established by Ebendorff-Heidepriem and Monro[15], the apparent

viscosity can be calculated using the definition of the Relative force presented in Table 6 of that

study[15]. Based on this definition, as shown in Table 6, the apparent viscosity is at most 57% of

the nominal viscosity.

Table 6: Shear thinning optimization study results for Tellurite using a no-slip boundary condition.

Cross law Parameters			Extruded preform diameter (mm)	Relative force*	$\eta_{Apparent}$ (Pa·s)
η_0 (Pa·s)	λ	m			
6.31E+08	1.00E+02	0.95	10.5	57.22%	3.61E+08
6.31E+08	2.00E+02	0.82	10.5	43.31%	2.73E+08
6.31E+08	4.00E+02	0.74	10.5	32.56%	2.05E+08
6.31E+08	8.00E+02	0.70	10.5	24.15%	1.52E+08
6.31E+08	2.00E+03	0.65	10.5	15.97%	1.01E+08
6.31E+08	4.00E+03	0.63	10.5	11.52%	7.27E+07

Glass material behavior is generally known to have a constant viscosity for a broad range of shear rate[12]. Furthermore, Scherer[22] reported that inorganic glass starts to deviate from viscous behavior at relatively high stress levels such as 50-100 MPa, which were not reached in these numerical experiments. Therefore, while nonlinear viscosity can explain the die swell results in Table 1 from a numerical point of view, from a physical point shear thinning is an unlikely explanation.

In a study of friction mechanisms in polymer extrusion, Joshi et al.[27] present a simulation where the influence of slipping of the polymer was considered using a nonlinear viscosity. They showed that interface slip between the polymer and the channel could lead to a behavior similar to that of nonlinear viscosity. Therefore, while shear thinning can cause a noticeable change in die swell, other factors must be more important. In the next section the no-slip boundary condition, which was enforced throughout this study, is relaxed.

Interface slip

Due to the relatively high viscosity of the glass in the extrusion cases of Table 1, the possibility of slip at the die/glass interface is considered. In this section the linear form of the Navier law of friction[21] is used to account for interface slip, which is defined by

$$u_s = b \frac{du}{dy}\bigg|_{y=0} = b \dot{\gamma}_w = \frac{b}{\eta} \sigma_w = k \sigma_w \qquad \textbf{(5)}$$

where u_s is the relative slip velocity at the interface, b is a constant with units of length, $\dot{\gamma}_w$ is the shear rate in the glass at the interface, η is the viscosity of the glass and k is the friction coefficient. Similar to the shear thinning case, an optimizer was used to adjust the friction coefficient to target the measured die swell for the case of viscous material behavior. The results are presented in Table 7.

Table 7: Die Swell optimization results for viscous material behavior with interface slip using the Navier law.

Case	Ram speed (mm/min)	Log viscosity (Pa·s)	Extruded preform diameter (mm)	Numerical diameter from optimizer	Required Navier friction coefficient: Log[k·Pa/(m/s)]
1	0.5	7.4	11.0±0.2	11.007	10.960
2	0.2	8.1	11.0±0.2	11.000	11.649
3	0.2	8.6	11.0±0.2	11.002	12.151
4	0.2	8.8	10.4±0.2	10.399	11.280
5	0.2	8.8	10.5±0.2	10.497	11.510

As shown in Table 7 the presence of slip can account for the discrepancy between the data and the results. Furthermore, the values of Log[k·Pa/(m/s)] are at a reasonable level. For this viscosity range, additional computations showed that the no friction limit corresponds to about Log[k·Pa/(m/s)] = 8, while the no slip limit occurs at about Log[k·Pa/(m/s)] = 14. In order to see the effect of including slip and viscoelastic material behavior, the same optimization procedure to determine the friction coefficient to obtain the target value of the die swell was applied for a viscoelastic material. These results are presented in Table 8 for the same range of relaxation times considered in Table 5. These results show that the friction coefficient is not sensitive to

the relaxation time, indicating that viscoelasticity does not have a significant effect on die swell

compared to that of slip.

Table 8: Same as Table 7 for viscoelastic material behavior.

Case	Required Navier friction coefficient to achieve measured preform diameter: Log[k·Pa/(m/s)]				
	λ =0.1	λ =1	λ =5	λ =10	λ =20
1	10.95	10.946	10.89	10.35	10.95
2	12.045	12.045	12.04	12.01	11.87
3	12.147	12.145	12.14	12.16	12.02
4	11.283	11.281	11.27	11.27	11.25
5	11.648	11.645	11.64	11.66	11.52

Ram force

The focus of the current study is the effect of modeling assumptions on the die swell. Since

interface slip appears to be the most significant factor in the die swell, it is important to also

consider the ram force since for a given viscosity and die geometry, friction plays the primary

role in the force required to maintain a given ram speed. In all the previous calculations in

Tables 4 - 8 the ram force is a computational output from the extrusion. These forces are

summarized in Table 9.

Table 9. Plateau values of ram force (kN) for selected trials from Tables 4 - 8.

Case	Force data (kN)	Viscous no-slip (Table 4)	VE no-slip (Table 5)	S.T. no-slip (Table 6)	Viscous slip (Table 7)	VE slip (Table 8)
1	6.8	11.56	λ = 0.1: 11.548 λ = 1: 11.546 λ = 5: 11.61	-	9.33	λ = 0.1: 9.294 λ = 1: 9.287 λ = 5: 9.095
2	14	23.16	λ = 0.1: 23.23	-	18.61	λ = 0.1: 18.67

			λ = 1: 23.22 λ = 5: 23.24			λ = 1: 18.66 λ = 5: 18.69
3	67	73.14	λ = 0.1: 23.23 λ = 1: 23.22 λ = 5: 23.24	-	58.81	λ = 0.1: 58.97 λ = 1: 58.93 λ = 5: 59.05
4	26	108.46	λ = 0.1: 108.80 λ = 1: 108.78 λ = 5: 108.86	-	34.72	λ = 0.1: 35.00 λ = 1: 34.93 λ = 5: 34.82
5	25	108.46	λ = 0.1: 108.80 λ = 1: 108.78 λ = 5: 108.86	m = 0.95: 62.1 m = 0.70: 26.2 m = 0.63: 12.5	45.46	λ = 0.1: 45.91 λ = 1: 45.87 λ = 5: 45.66

As a general trend in Table 9 the computational model over-predicts the ram force. Similar to the results for the die swell comparisons in Tables 4 - 6, when no-slip is assumed only shear thinning has the ability to match the data. The case of m = 0.70 and λ = 800 from Table 6 matches the die swell and comes close to the ram force as shown in Table 9. However, as shown in Figure 7, it is believed that the reduction in viscosity in this shear thinning model is too drastic to be physical. The ram force can also be reduced by allowing for slip, but as the results in Table 9 show the values of friction used to match the die swell from Tables 7 and 8 lead to a ram force that is still too high for four of the five study cases. Concerning Case 3 which is the only case for which the model over predicts the die swell, the experimental ram force is unusually high compared to Cases 4 and 5, which have higher viscosity.

In order to quantify the discrepancy in force in Table 9 in terms of the die swell for which the experimental error is known, the measured ram force can be matched by changing the friction coefficient, which leads to a prediction of the die swell. This optimization task for viscous glass behavior was performed and the results are presented in Table 10. The percent error in die

swell in this table is obtained using the die exit diameter of 10.2 mm, i.e., the actual

experimental die swell for Cases 1-3 is 11 mm – 10.2 mm = 0.8 mm.

Table 10. Die swell obtained by adjusting friction coefficient to match experimental ram force.

Case	$Log \dfrac{\eta}{Pa \cdot s}$	Measured preform diameter (mm)	Force data (kN)	Force calculated (kN)	Required Log[k·Pa/(m/s)] to match force	Resulting preform diameter (mm)	% Error in die swell
1	7.4	11.0±0.2	6.8	6.800	10.450	10.688	-39.0
2	8.1	11.0±0.2	14	14.039	11.187	10.711	-36.1
3	8.6	11.0±0.2	67	66.804	12.594	11.222	+27.8
4	8.8	10.4±0.2	26	26.000	11.036	10.325	-37.5
5	8.8	10.5±0.2	25	25.000	11.002	10.316	-61.3

As seen from the Table 10 results, by changing the friction coefficient from the values in Table 7

to those in Table 10, the die swell is now under-predicted in all cases but Case 3. The Bismuth

(Case 4) and Tellurite (Case 5) die swell values are within experimental measurement error,

while the cases of F2 glass (Cases 1, 2 and 3) are not. In terms of percent error, the worst case is

Tellurite. From a computational point of view, two possible explanations for under-predicting

the die swell in Table 10 are shear thinning and viscoelastic behavior. Inclusion of either of these

behaviors can be used to match both the die swell and the ram force. For example, by adding

shear thinning the friction force would have to be higher, which would result in an increase in

die swell. Such a modification might be appropriate for Tellurite. From an experimental point of

view, the low die swell values in Table 10 can be explained by viscosity that is lower than what

was determined based on temperature measurements and/or conversion from temperature to

viscosity. In this case a higher friction coefficient would be needed to match the ram force,

which would increase the die swell. For Cases 1-3 the combinations of friction coefficient and

viscosity using viscous glass behavior were determined to match both the die swell and the ram

force. For Case 1 these values were Log[k·Pa/(m/s)] = 10.81 and $\eta = 10^{7.27}$ Pa·s, for Case 2:

Log[k·Pa/(m/s)] = 11.53 and $\eta = 10^{7.98}$ Pa·s and for Case 3: Log[k·Pa/(m/s)] = 12.207 and $\eta =$

$10^{8.656}$ Pa·s. By comparing these three viscosity exponents (7.27, 7.98, 8.66) to those of Cases 1-3

from Table 1 (7.4, 8.1, 8.6), these results give perhaps the best indication of how the

computational and experimental results compare.

Discussion

Glass forming processes such as Precision Glass Molding and extrusion of Photonic Crystal Fiber

preforms can take place at temperatures below those where a no-slip fluid mechanics boundary

condition is justified. Typical viscosity ranges for these processes are $10^{7.5}$ to 10^9 Pa·s, where

both interface slip and viscoelastic material behavior complicate processing and modeling. In

this study experimental extrusion data in this viscosity range was used to quantify the

importance of shear thinning, viscoelastic behavior and slip. Comparisons between model

predictions and measurements were presented with reasonable results, understanding there

are sources of error from both. Two important sources of error are that the model assumes

constant viscosity (temperature) throughout the volume of glass and uniform friction

throughout the die surface. Each of these assumptions can be the cause for a discrepancy

between model predictions and measurements. While the computational results show that slip

most likely occurs in these extrusion examples, they does not rule out the presence of mild

shear thinning and/or viscoelastic behavior. In order to address further these aspects,

independent experiments are required to characterize the material behavior and friction. As

discussed by Joshi et al.[28,29] who studied the cylinder compression test, a possible complication

in interpreting data is that changes in both friction and viscosity can cancel each other, which requires accurate knowledge of one quantity in order to determine the other with accuracy. As such, the measured value of the viscosity affects the prediction of the friction coefficient, k, in the current study. Furthermore, the change in predicted friction coefficient from a change in measured viscosity could easily be more significant than the change due to the inclusion of viscoelastic effects as quantified in Table 8. The experimental viscosity values are based on temperature measurements of the outer portion of the die[15] and are believed to be accurate enough to conclude that the current study provides evidence that slipping occurred in these extrusion cases and is the most significant factor that affects the die swell.

Conclusion

The extrusion of high viscosity glass was studied from a numerical point of view under various assumptions. After demonstrating convergence of the computational solution and providing justifications for the neglect of gravity and the details of the flow profile at the die entrance, a comparison between experimental data and computational results was made using the most basic viscous material model with no-slip boundary conditions. Since the corresponding numerical results were not able to fit the data, the model was adjusted by considering viscoelastic material behavior, shear thinning and slip at the glass/die interface. Based on this study the following conclusions can be made:

- The die swell results are over-predicted using a no-slip boundary condition and a viscoelastic material model for all values of the relaxation time including the viscous limit of zero. For the physical range of relaxation times, $\lambda < 1$, a very small drop in

computed die swell is observed. A dramatic increase in die swell occurs as the relaxation time increases, but this is outside of the physical range.

- Shear thinning can explain the measured die swell, but only if local reductions in viscosity are so severe as to be non-physical. Therefore, for reasonable shear thinning behavior using a no-slip boundary condition the die swell is over-predicted.

- Relaxation of the no-slip boundary condition allowed for an easy match of the die swell results using purely viscous material behavior. As such slip at the interface is a primary mechanism that affects the current die swell results. If either the friction coefficient or the viscoelastic material behavior was known based on independent tests, further refinement in the die swell solution could be obtained.

- The computational model using viscous material behavior and interface slip over-predicted the ram force for all but one case, although the results were close enough to be explained by a measurement error in viscosity of at most 0.13 Pa·s.

References

[1] H. Ebendorff-Heidepriem and T. Monro, "Extrusion of complex preforms for microstructured optical fibers," Opt. Express 15, 15086-15092 (2007).

[2] S. D. Savage, C.A. Miller, D. Furniss, A. B. Seddon, "Extrusion of chalcogenide glass preforms and drawing to multimode optical fibers", Journal of Non-Crystalline Solids,

Volume 354, Issue 29, 1 July 2008, Pages 3418-3427, ISSN 0022-3093,

10.1016/j.jnoncrysol.2008.01.032.

[3] A. Belwalkar, H. Xiao, W. Z. Misiolek, J. Toulouse, Extruded tellurite glass optical fiber

preforms, Journal of Materials Processing Technology, Volume 210, Issue 14, 1 November

2010, Pages 2016-2022, ISSN 0924-0136, 10.1016/j.jmatprotec.2010.07.018.

[4] A. B. Seddon, D. Furniss and A.Motesharei, "Extrusion method for making fiber optic

preforms of special glasses," Proc. SPIE 3416, Infrared Glass Optical Fibers and Their

Applications, 32 (September 28, 1998); doi:10.1117/12.323398.

[5] D. Furniss and A. B. Seddon, Towards Monomode Proportioned Fibreoptic Preforms By

Extrusion, *Journal Of Non-Crystalline Solids*, 256&257 232-236 (1999).

[6] E.T.Y. Lee and E.R.M. Taylor, "Two-die assembly for the extrusion of glasses with

dissimilar thermal properties for fibre optic preforms", Journal of Materials Processing

Technology, Volume 184, Issues 1–3, 12 April 2007, Pages 325-329, ISSN 0924-0136,

10.1016/j.jmatprotec.2006.11.115.

[7] B. Ananthasayanam, D. Joshi, M. Stairiker, M, Tardiff, K.C. Richardson and P.F. Joseph,

"High Temperature Friction Characterization for Viscoelastic Glass Contacting a Mold,"

Journal of Non-Crystalline Solids, 385 100-110 (2014).

[8] B. Ananthasayanam, P.F. Joseph, D. Joshi, S. Gaylord, L. Petit, V.Y. Blouin, K.C.

Richardson, D.L. Cler, M. Stairiker and M. Tardiff, "Final shape of precision molded

optics: Part I – Computational approach, material definitions and the effect of lens shape," *J. Therm. Stresses*. 35 (2012) 550-578.

[9] M. Sellier, C. Breitbach, H. Loch, N. Siedow, Proceedings of the I MECH E Part B Journal of Engineering Manufacture. 221 (2007) 25-33.

[10] B. Ananthasayanam, P.F. Joseph, D. Joshi, S. Gaylord, L. Petit, V.Y. Blouin, K.C. Richardson, D.L. Cler, M. Stairiker, M. Tardiff, J. Therm. Stresses. 35 (2012) 614-636.

[11] Y.Yue, G. Carl, C. Russel, "Rheological properties of calcium metaphosphorate melts during extrusion", Glasstech. Ber, 1999.

[12] M. Brown, "A review of research in numerical simulation for the glass-pressing process," Proc. of the I MECH E Part B J. Eng. Manuf., 221 (2007), Number 9, pp. 1377-1386.

[13] W. Egel-Hess and E.Roeder, "Extrusion of glass melt – influence of wall friction", Glasstech. Ber ,1989

[14] H.-J. Mayer, Chr. Stiehl and E. Roeder, "Applying the finite-element method to determine the die-swell phenomenon during the extrusion of glass rods with non-circular cross-sections," Journal of Materials Processing Technology, Volume 70, Issues 1–3, October 1997, Pages 145-150, ISSN 0924-0136, 10.1016/S0924-0136(97)00053-8.

[15] H. Ebendorff-Heidepriem and T. Monro, "Analysis of glass flow during extrusion of optical fiber preforms," Opt. Mater. Express 2, 304-320 (2012).

[16] R. Ahmed, R.F. Liang and M.R. Mackley, "The experimental observation and numerical prediction of planar entry flow and die swell for molten polyethylenes," J. Non-Newtonian Fluid Mech., 59, 129 153, 1995.

[17] S. Bunditsaovapak, T. Fagon and S. Thenissara, "Surface Tension Effect to Die-Swell Extrusion of Viscoelastic Fluid," AIP Conf. Proc. 982, 639 (2008); doi: 10.1063/1.2897871.

[18] M.F. Toméa, G.S. Pauloa, F.T. Pinhob and M.A. Alvesc, "Numerical solution of the PTT constitutive equation for unsteady three-dimensional free surface flows," J. Non-Newtonian Fluid Mech. 165, 247–262, 2010.

[19] R.I. Tanner, "A new inelastic theory of extrudate swell," J. Non-Newtonian Fluid Mech. 6 289 1980.

[20] P. Jay, J.M. Piau, N.E. Kissi and J. Cizeron, "The reduction of viscous extrusion stresses and extrudate swell computation using slippery exit surfaces," J. Non-Newtonian Fluid Mech. 79, 599-617, 1998.

[21] S.G. Hatzikiriakos, "Wall slip of molten polymers," Progress in Polymer Science, 37, 624-643, 2012.

[22] G.W. Scherer, Relaxation in Glass and Composites, John Wiley and Sons, New York, 1986.

[23] R.I. Tanner, Engineering Rheology, Oxford University Press, Mar 2, 2000 - Page 160.

[24] T. Rouxel, "Elastic Properties and Short-to Medium-Range Order in Glasses", J. Am. Ceram. Soc., 90 [10] 3019-3039 (2007)

[25] Macosko C. W.:Rheology - Principles, Measurements and Applications. Wiley-VCH, New York (1994) -Page 86.

[26] O. Verhoyen and F. Dupret, A simplified method for introducing the Cross viscosity law in the numerical simulation of Hele Shaw flow, Journal of Non-Newtonian Fluid Mechanics, Volume 74, Issues 1–3, January 1998, Pages 25-46, ISSN 0377-0257

[27] Y. M. Joshi, A. K. Lele and R.A. Mashelkar, "A unified wall slip model," Journal of Non-Newtonian Fluid Mechanics, Volume 94, Issues 2–3, 30 November 2000, Pages 135-149, ISSN 0377-0257, 10.1016/S0377-0257(00)00160-9.

[28] D.Joshi, P. Mosaddegh, J. D. Musgraves, K. C. Richardson and Paul F. Joseph, "Thermo-Mechanical Characterization of Glass at High Temperature Using the Cylinder Compression Test: Part I –Viscoelasticity, Friction and PPV," Journal of Rheology, 57, pp. 1367-1389, 2013.

[29] D. Joshi, P. Mosaddegh, J. D. Musgraves, K. C. Richardson and P. F. Joseph, "Thermo-Mechanical Characterization of Glass at High Temperature Using the Cylinder Compression Test: Part II – No-Slip Experiments, Viscoelastic Constants and Sensitivity," Journal of Rheology, 57, 1391-1410, 2013.
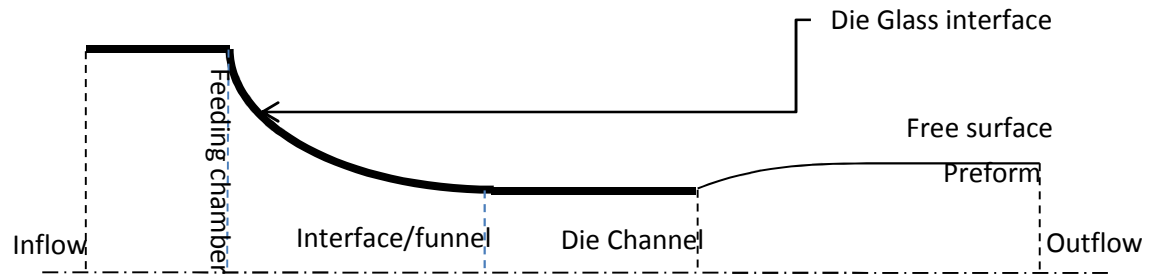
Figure 36. A model of the reference die geometry used in the experiments[15].

Refinement directions
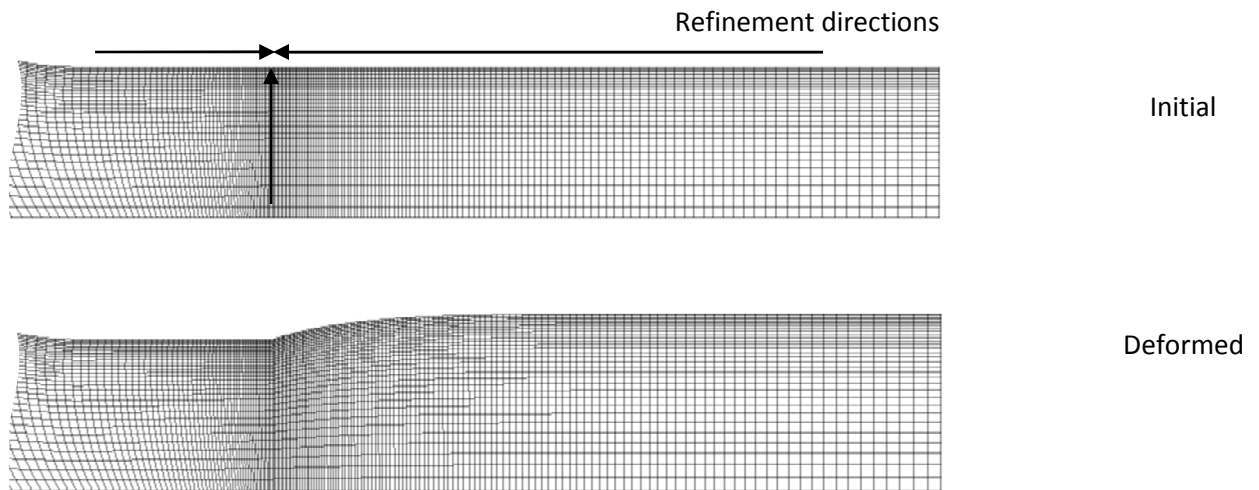
Initial

Deformed

Figure 2. Mesh refinement position (Default mesh), deformed and initial mesh.
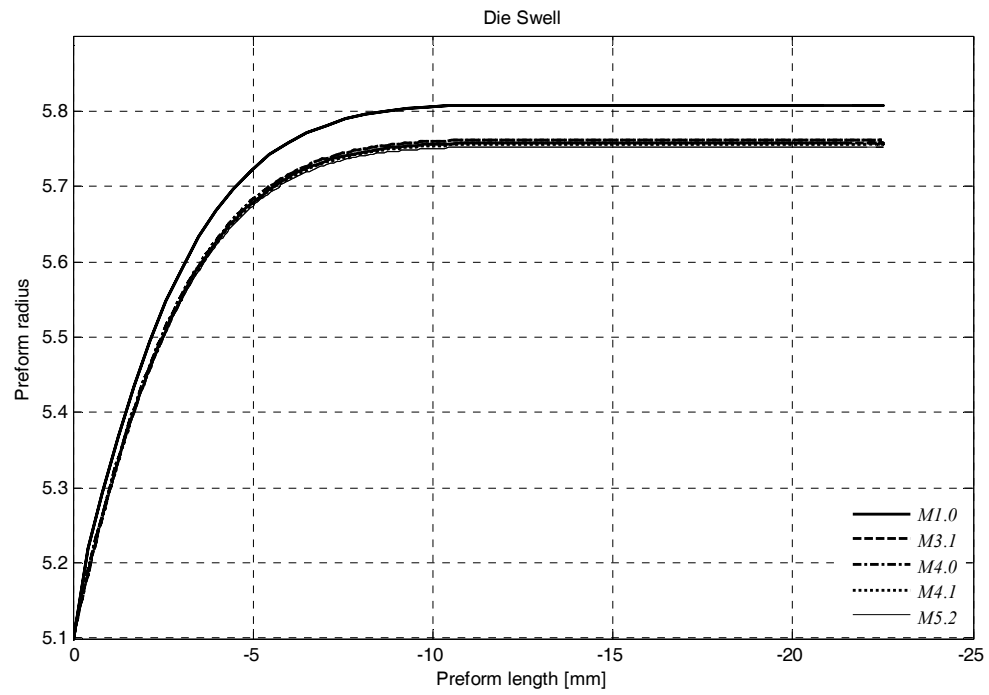
Figure 3. Die swell profiles in the mesh convergence study.
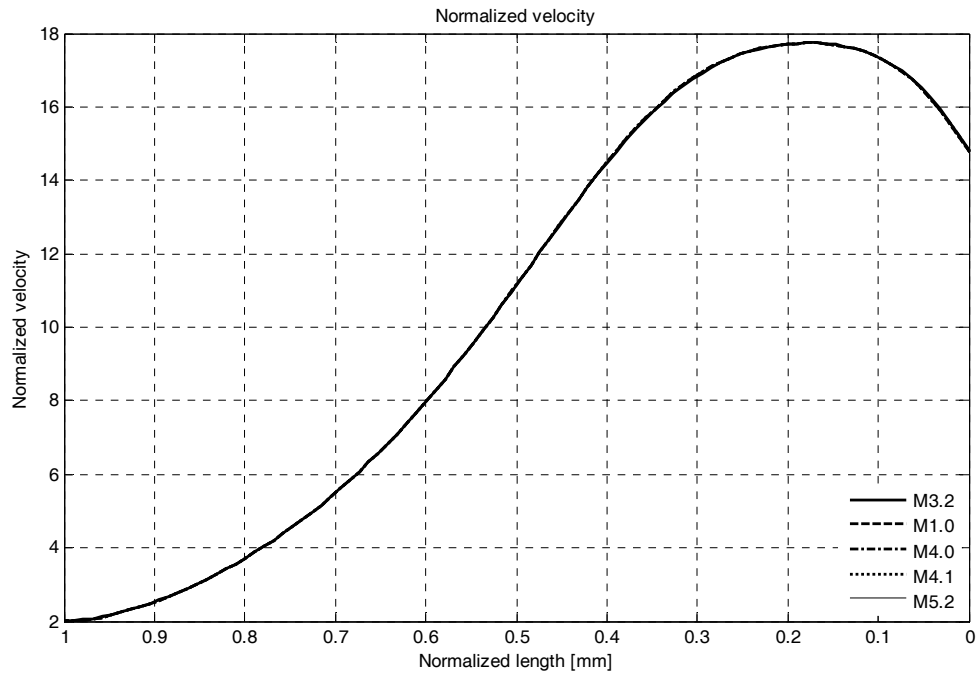
Figure 4. Velocity at the center line from the convergence study.
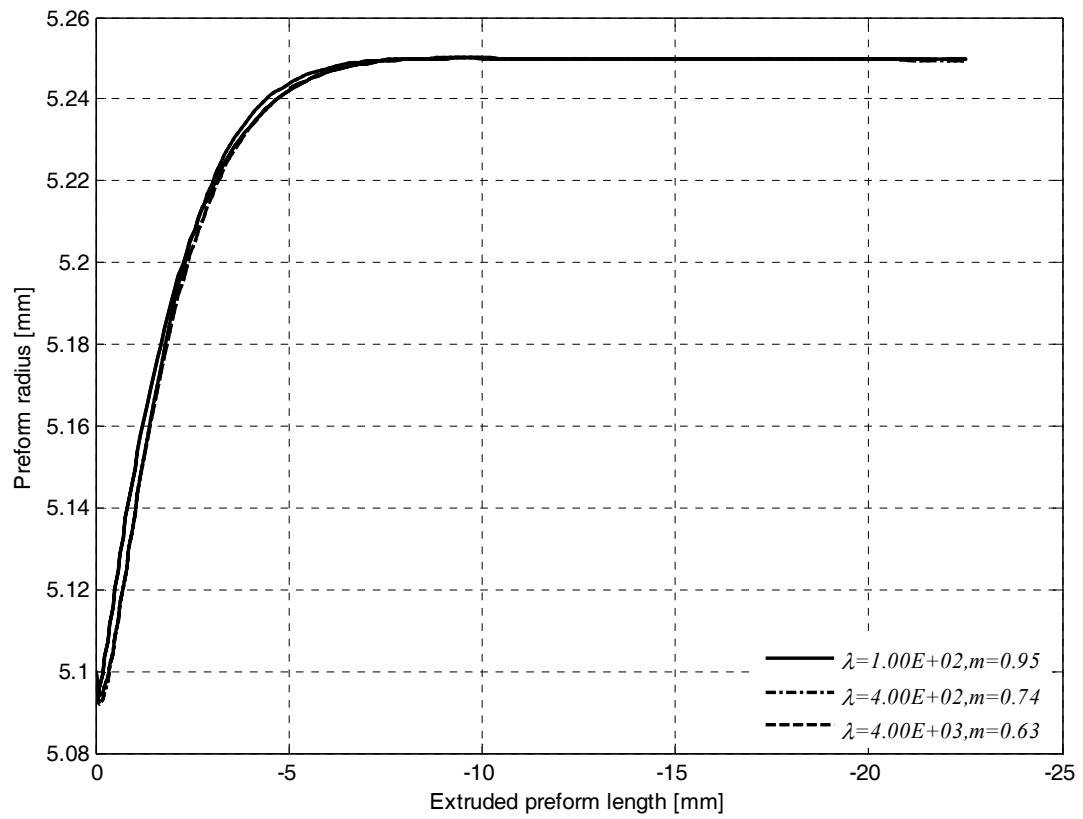
Figure 5. Die swell profiles from the optimization study using the Cross law of shear thinning.
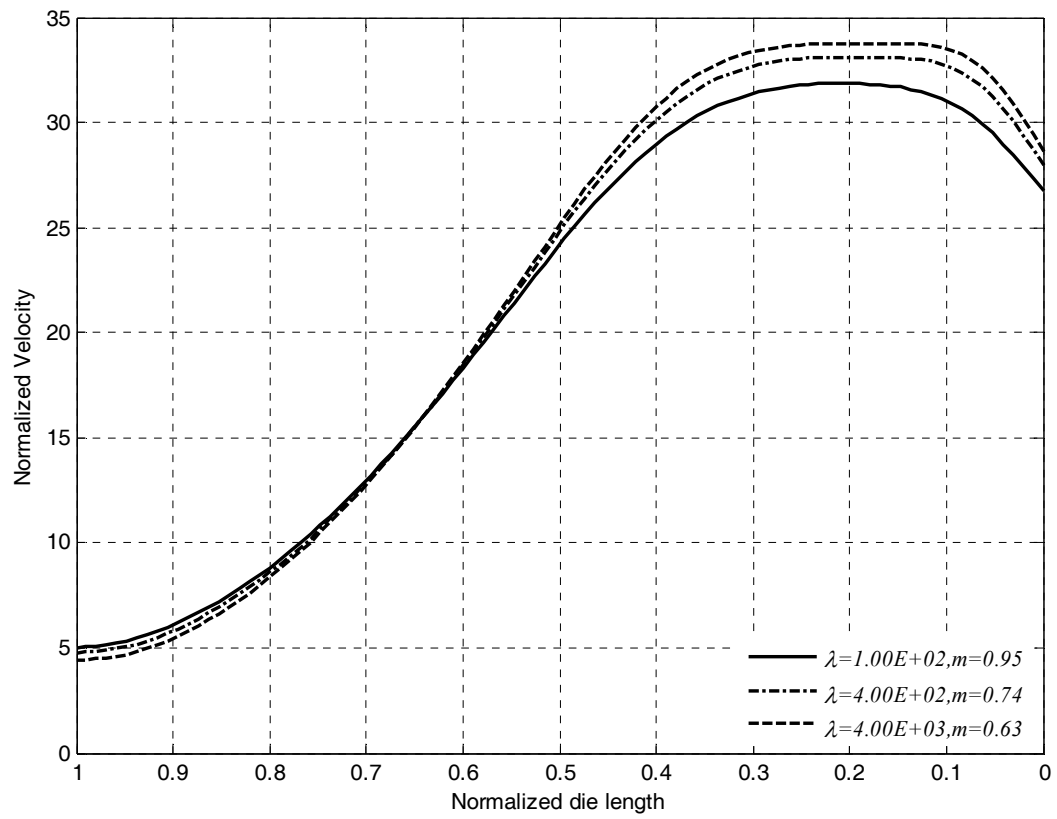
Figure 6. Same as Figure 5 for the velocity along the center line.
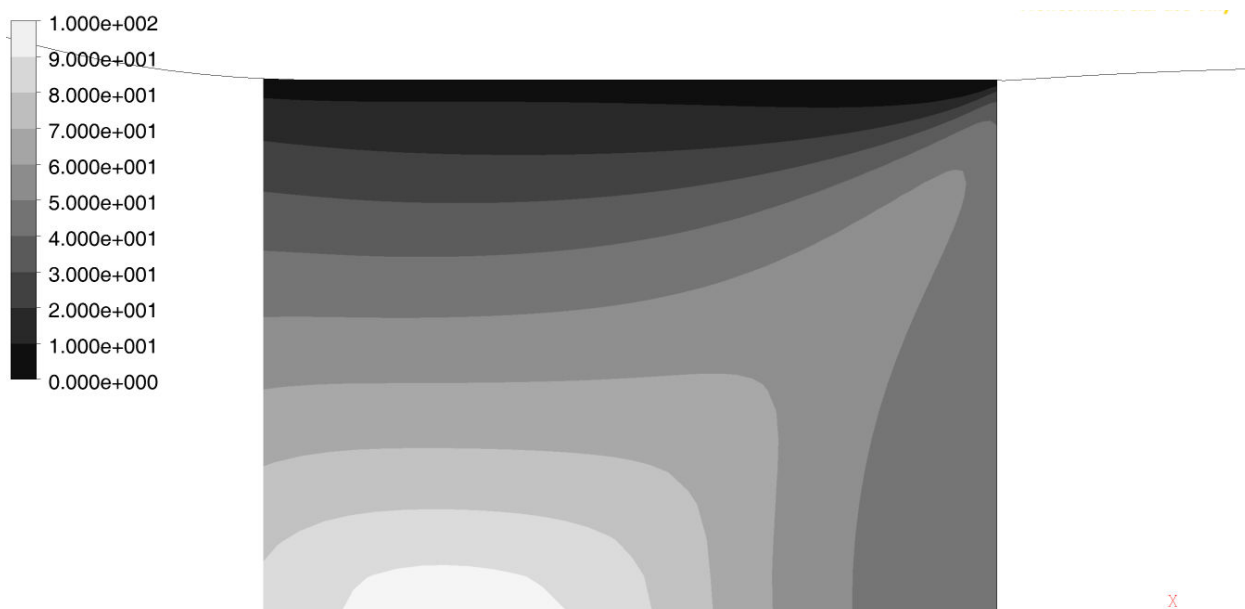
$m = 0.94, \lambda = 100$
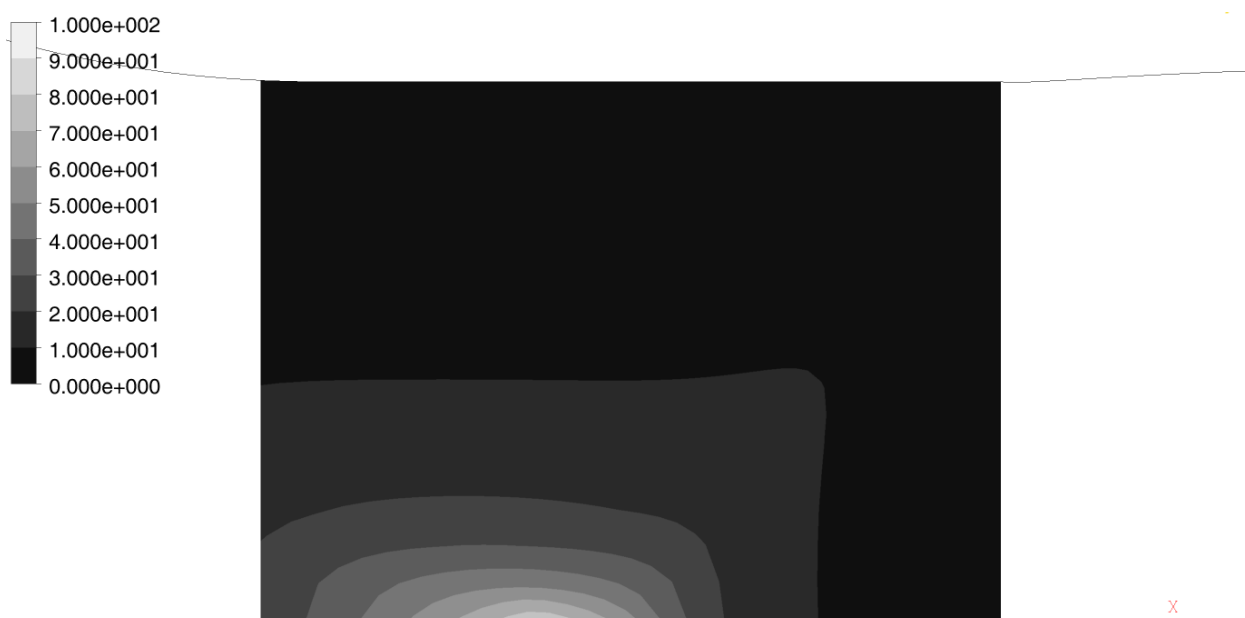
$m = 0.63, \lambda = 4000$

Figure 7. Viscosity distributions for two cases of the Cross law optimization study (see Table 6), which show regions in the die channel where viscosity is within the prescribed range of percentage of η_0, where η_0 is $10^{8.8}$ Pa·s. The centerline is on the bottom and the die exit is on the right.
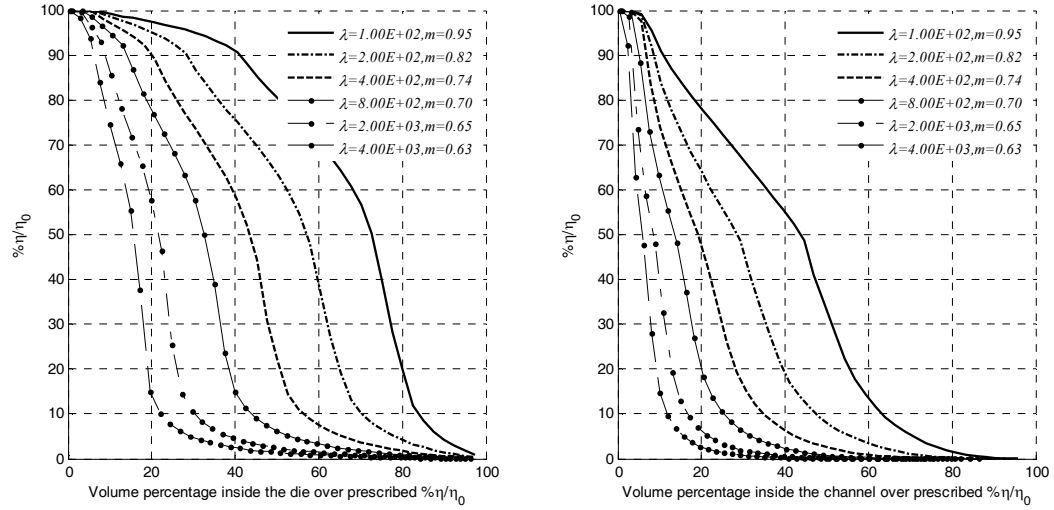
Figure 8. Viscosity distribution from the Cross law optimization study presenting the percentage of the volume of glass that has a viscosity greater than the prescribed level of percentage of η/η_0. The figure on the left is for the entire die, while the figure on the right is for only the channel.

Appendix C3. (Paper DRAFT)
  Ring compression test for high temperature glass based on the generalized Navier law

Mohamed Trabelssi and Paul F. Joseph*

Department of Mechanical Engineering, Clemson University, Clemson, SC, USA

*Corresponding author, jpaul@clemson.edu, Phone: 864-656-0545, Fax: 864-656-4435

Abstract: Glass forming processes such as Precision Glass Molding and high viscosity extrusion take place at temperatures were slip between the glass and mold surfaces is known to occur. Characterization of the frictional forces that accompany interface slip are essential in computational simulations of these processes for prediction of pressing time or force, distortion of the part and possible wear of expensive mold surfaces. In this study the Navier law, where the interface shear stress, τ, is related to the relative sliding speed of the glass on the mold surface, v, by $\tau = kv^e$, is used in simulations of the ring compression test to produce friction calibration curves. Contrary to the nonlinear form of the law, the linear form is used to produce calibration curves that are rate and viscosity independent. The Navier friction coefficient for the linear form is characterized for the full range of behavior from no-slip to no friction. The linear results show an approximate one to one correspondence between the Navier coefficient and the Coulomb friction coefficient allowing one ring compression test to provide both characterizations.

Keywords: friction, ring compression test, Navier law, glass, high viscosity

1. Introduction

According to Coulomb friction, the friction force between sliding bodies is proportional to the pressing force. It is generally agreed that this model assumes the presence of micro imperfections on the contacting surfaces that interact to create a resistance to sliding. This is a good assumption for a solid dry contact pair and is widely used in solid mechanics. As the temperature of glass increases, this solid mechanics-based mechanism gives way to a more fluid mechanics-based response.

The friction behavior of amorphous long molecular chain materials has been considered in several studies. These materials, whether considered as viscous or viscoelastic, react with a neighboring foreign material in a way that depends on their molecular composition. In the vicinity of the contact zone, the molecular chains create a boundary layer with completely different behavior from that of the bulk material. Slipping within this layer can occur due to several mechanisms.

Based on micro structure mechanics, models were built to explain numerous complex slip phenomena. However for the sake of simplicity and numerical efficiency, a model based on macro observations provides more workable implementation while being compatible with particular cases of the micro models and experimental observations. This model suggest a linear relationship between the log of the shear stress on the log of the velocity, given by

$$\tau = k\, v^e \Leftrightarrow \log \tau = \log k + e \log v$$

where τ is the shear stress at the wall and v is the velocity. This law is called the generalized Navier law.

2. Finite Element Model

Mohamed - here we have to describe what was modeled, how it was modeled and convergence of the model.

3. Results

3.1 Importance of previous work.

The study by Ananthasayanam et al. [9] showed that if the ring compression test was conducted according to a prescribed process of heating, soaking, pressing and cooling, the FCC could be obtained simply by assigning the material properties at the pressing temperature in the computational model and then simulating the entire test at that temperature. Additional requirements included uniform temperature in the ring at the time of pressing and measurement of the inner diameter at the centerline. Furthermore, either constant load or pressing using a constant rate resulted in the same FCC. Guidelines were presented for both cases for a glass specimen size with outer diameter (*OD*) of 19.15 mm, inner diameter (*ID*) of 9.59 mm and a height (*H*) of 6.37 mm, which gives the ratios of *OD:ID:H* = 6:3:2 that were recommended by Male and Depierre [1]. As such, in the current study it was sufficient to conduct isothermal, rate controlled tests using the standard specimen at constant viscosity to produce valid FCC. The rates used in the current study range from ….

3.2 Pressing speed dependence of the generalized Navier law

Ananthasayanam et al. [9] showed that the FCC obtained using the Coulomb friction law were the same for rate and load controlled tests. Since the Navier law is based on relative sliding speed, it is important study how rate of loading affects the FCC for a given viscosity. The computational results revealed that the calibration curves for a given nonlinear model ($e \neq 1$) can be very sensitive to pressing speed. The FCC for a specific combination of *k, e* and range of pressing speeds were where this sensitivity was very noticeable is presented in Figure 1. In this figure the calibration curves are plotted for a viscosity of 10^9 Pa·s, exponent, $e = 1.2$, Navier friction coefficient, $k = 10^{12}$ Pa/(m/s)^e and five pressing speeds (the pressing times to achieve ??%

axial deformation are 5s 10s 20s 200s 1000s). This shows that different curves, i.e., FCC associated with different values of the Coulomb friction coefficient, μ, can be achieved using the same generalized Navier friction law. As such, Figure 1 shows a case where the FCC are sensitive to the rate of loading.

In order to show the importance of the exponent, e, in Figure 2 the FCC are presented for the same conditions as those of Figure 1, but for $e = 0.25, 0.5, 1, 1.2$ and 1.75. This result is typical for those with other k and viscosity values. For small exponents ($e = 0.25$), the FCC are insensitive to rate and go to the high friction limit, while the FCC for large exponents (1.75) are also rate insensitive and tend to the low friction limit. The special case of $e = 1$, which gives the linear form of the law, is rate insensitive and corresponds to an intermediate level of friction. Finally, the other values when $e \neq 1$ and neither high nor low, show rate dependence. The important conclusion, which is based on examination of behavior for the full range of viscosity and friciton coefficient, is that the FCC are independent of loading rate for the linear form of the law.

3.3 Viscosity dependence of the calibration curves

While the FCC using the linear form of the Navier law are independent of rate, the FCC depend on the viscosity, which was not the case for the Coulomb law [9]. Therefore it appears that for each viscosity new calibration curves should be generated. Generating FCC for a specific viscosity is not practical, and it compromises one of the most important advantages of the ring compression test, which is material behavior independence. In order to understand how the calibration curves depend on the value of viscosity, the data for the FCC must be plotted in a different way. The standard FCC correspond to plotting the percent decrease in inner radius as a function of axial deformation for a family of friction coefficients for each value of viscosity. In Figure 3 the percent decrease in inner radius is instead plotted as a funtion of the Log of the

friction coefficient, Log(k·m/(Pa·s)), for a family of viscosity values for each value of axial deformation. While these results show a dependence on viscosity, there appears to be a constant shift from one viscosity curve to another and this shift is constant from one axial deformation level to another. This suggests plotting the percent decrease in inner radius instead as a function of Log(k·m/η), which is done in Figure 4. Clearly this simple but important approach, which works for all levels of deformation, eliminates the viscosity dependence of the FCC.

3.4 FCC for both the Coulomb and linear Navier models

FCC were generated using both the Coulomb friction model as a function of the Coulomb friction coefficient, μ, and the linear Navier model as a function of Log(k·m/η). Both curves are presented in Figure 5, where interestingly enough, it is seen that the profiles are very similar. This suggests an approximate conversion from one model to the other. Apparently the loading in this test does not distinguish between the two models as does, for example, the pressurized Couette flow test of [..]. As a final calculation in this section, a curve fitting procedure is used to obtain k for an arbitrary value of percent inner decrease in inner radius for a given level of axial deformation, i.e., a way to interpolate between the curves presented in Figure 5.

3.5 Interpolation procedure for the FCC

The procedure to interpolate between the FCC in Figure 5 for a given data point (FCC_x, FCC_y), where FCC_x is the axial deformation normalized by the original height and FCC_y is the corresponding decrease in the inner radius normalized by the original inner diameter, is to first obtain the "effective" decrease in inner radius defined as

$$FCC_{effective} = A \times FCC_y + B , \qquad\qquad (2)$$

where, through a procedure of curve fitting, the coefficients A and B were obtained and are

presented in Table 1.

Table 1. Values of the coefficients A and B defined in Equation (2) that are used
to obtain Log($k \times m/\eta$) from Table 2.

FCC_x: Axial deformation/H from FCC	A	B
0.05		
0.10		
0.15		
0.20		
0.25		
0.30	4	0.18
0.35		
0.40		
0.45		
0.50		

Then the value of the effective inner radius from Eqn. (2) is used in Table 2 to obtain the friction

coefficient.

Table 2. Values of Log($k \times m/\eta$) in terms of the effective fractional decrease in
inner radius as defined by Equation (2).

$FCC_{effective}$: $A \times FCC_y + B$	Log(k×m/η)
-0.5	
-0.22	1.8
0.7	

An example of this two-step procedure is presented below for a viscosity of 10^8 Pa·s using the

data point $FCC_x = 0.30$ and $FCC_y = -0.1$, which coincides with the FCC in Figure 5 for $\mu = 0.04$:

$$FCC_{effective} = 4 \times (-0.1) + 0.18 = -0.22$$

$$\rightarrow k = \left(10^8 \times 10^{1.8}\right) Pa/(m/s) = 10^{9.8} Pa/(m/s) \qquad (3)$$

Application of this procedure was applied to the FCC data in Figure 5 to approximate the Navier

friction coefficient for increments of the Coulomb friction coefficient for levels of axial

deformation of 0.30 and 0.50. The results are presented in Table 3.

Table 3. Values of the Navier friction coefficient that coincide with the FCC
values for the Coulomb friction coefficient at levels of 0.30 and 0.50 axial
deformation. Equation (2) and Tables 1 and 2 were used to obtain these results;
see also Figure 5.

μ	decrease of inner D: 0.3	Log(k×m/η) 0.3	decrease of inner D: 0.5	Log(k×m/η) 0.5
0	-19.51	0	-41.41	0
0.01	-17.89	0.93	-36.33	0.867
0.02	-16.25	1.26	-31.26	1.232
0.03	-14.59	1.46	-26.16	1.449
0.04	-12.92	1.61	-21.09	1.618
0.06	-9.48	1.86	-11.70	1.884
0.08	-6.025	2.066	-4.494	2.065
0.1	-3.219	2.221	1.198	2.202
0.15	1.569	2.488	12.07	2.464
0.2	5.28	2.71	20.99	2.689
0.3	11.18	3.159	34.41	3.071
0.4	15.24	3.709	43.17	3.423
∞	17.47	∞	50.78	∞

4. Discussion

The RCT has been used for over forty years to characterize the coefficient of Coulomb friction

for metals used in forming processes. The complexity of conditions at the interface, which can

include slip and/or partial slip as axial deformation progresses, is quantified through

computational mechanics by the value of the inner radius as a function of the level of axial

deformation, which is easy for the experimentalist to measure. The test works because the inner

radius is highly sensitive to the level of friction between the ring specimen and the mold surfaces.

The test works especially well for glass since it has been shown [ ] that the FCC are insensitive to

the complex thermo-mechanical behavior of glass, meaning that one set of master curves can be used for any glass type. This universality of the FCC is attributed to the extreme sensitivity of the inner radius to friction, where all other effects are secondary.

In applying this test to characterize friction between hot glass and a mold or die surface, it is important to select the correct friction model for the application. In solid mechanics the most basic model is Coulomb friction, where the shear stress due to friction while slip occurs is proportional to the contact pressure and independent of sliding speed. In fluid mechanics the most basic model is the linear Navier law used herein, where the shear stress is proportional to the relative sliding speed and independent of the pressure. The laws are indeed opposites. The problems of interest, which include PGM and extrusion of PCF, occur at relatively high viscosity of about $10^{7.5} - 10^{9}$ Pa·s, which essentially spans the transition between fluid and solid behavior.

5. Conclusions

The ring compression test can be used to characterize the linear form of the Navier friction law for any glass type using universal FCC which are loading rate independent. Contrary to the FCC using the Coulomb friction model, the viscosity must be known to obtain the Navier friction coefficient. The nonlinear form can also be characterized, but requires the computational capability to generate specific FCC that are rate dependent. It is interesting that the profiles of the FCC using the linear Navier model are very similar to those of the Coulomb model, indicting there is an approximate one to one correspondence between μ and k for the ring compression test.

References

[1] A.T. Male and V. Depierre, ASME J. Lubr. Technol. 92 (1970) 389-397.

[2] H. Sofuoglu, H. Gedikli, J. Rasty, ASME J. Eng. Mater. Technol. 123 (2001) 338-348.

[3] H. Sofuoglu and H.J. Rasty, Tribol. Int. 32 (1999) 327-335.

[4] D.R. Hayhurst and M.W. Chan, Int. J. Mech. Sci. 47 (2005) 1-25.

[5] B. Ananthasayanam, P.F. Joseph, D. Joshi, S. Gaylord, L. Petit, V.Y. Blouin, K.C. Richardson, D.L. Cler, M. Stairiker, M. Tardiff, J. Therm. Stresses. 35 (2012) 550-578.

[6] B. Ananthasayanam, P.F. Joseph, D. Joshi, S. Gaylord, L. Petit, V.Y. Blouin, K.C. Richardson, D.L. Cler, M. Stairiker, M. Tardiff, J. Therm. Stresses. 35 (2012) 614-636.

[7] D. Joshi, P. Mosaddegh, J.D. Musgraves, K.C. Richardson, P.F. Joseph, J. Rheol. 57 (2013) 1367-1389.

[8] Dhananjay Joshi, Peiman Mosaddegh, J. David Musgraves, Kathleen C. Richardson, Paul F. Joseph, "Thermo-Mechanical Characterization of Glass at High Temperature Using the Cylinder Compression Test: Part II – No-Slip Experiments, Viscoelastic Constants and Sensitivity," Journal of Rheology, 57, 1391-1410, 2013.

[9] B. Ananthasayanam, D. Joshi, M. Stairiker, M. Tardiff, K.C. Richardson, P.F. Joseph, "High Temperature Friction Characterization for Viscoelastic Glass contacting a Mold," accepted November 4, 2013, Journal of Non-Crystalline Solids.
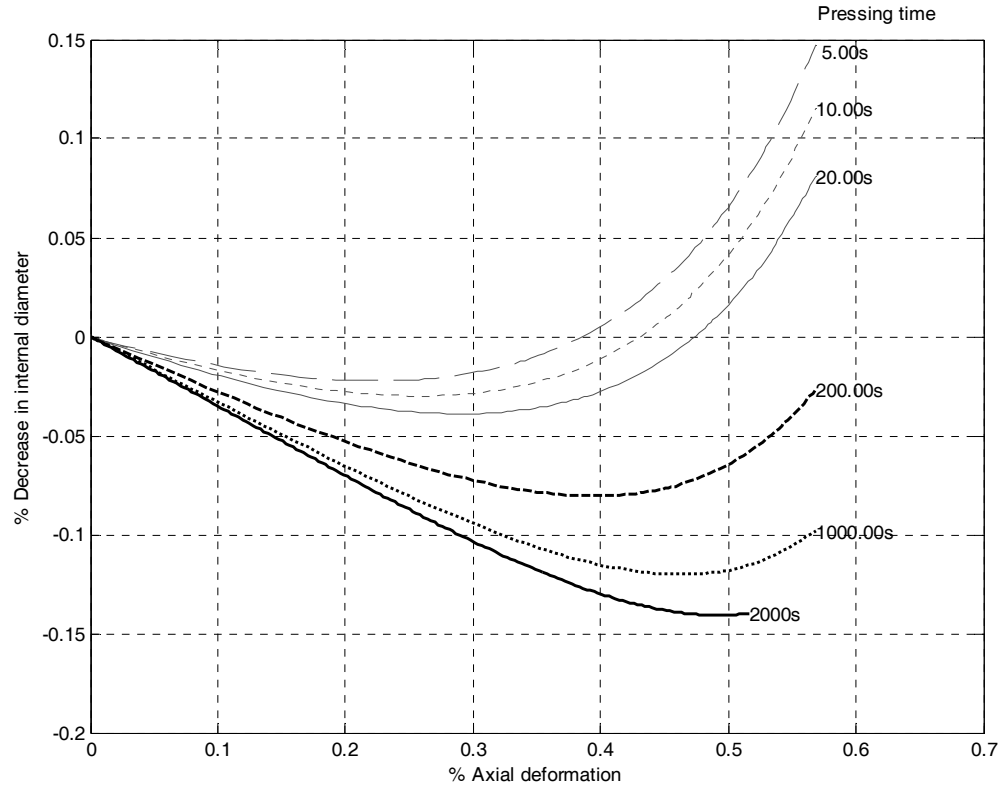
Figure 1. Dependence of the FCC on the pressing time for $\eta = 10^9$ Pa·s using a nonlinear form of the Navier law ($e = 1.2$, $k = 10^{12}$ Pa/(m/s)^e).
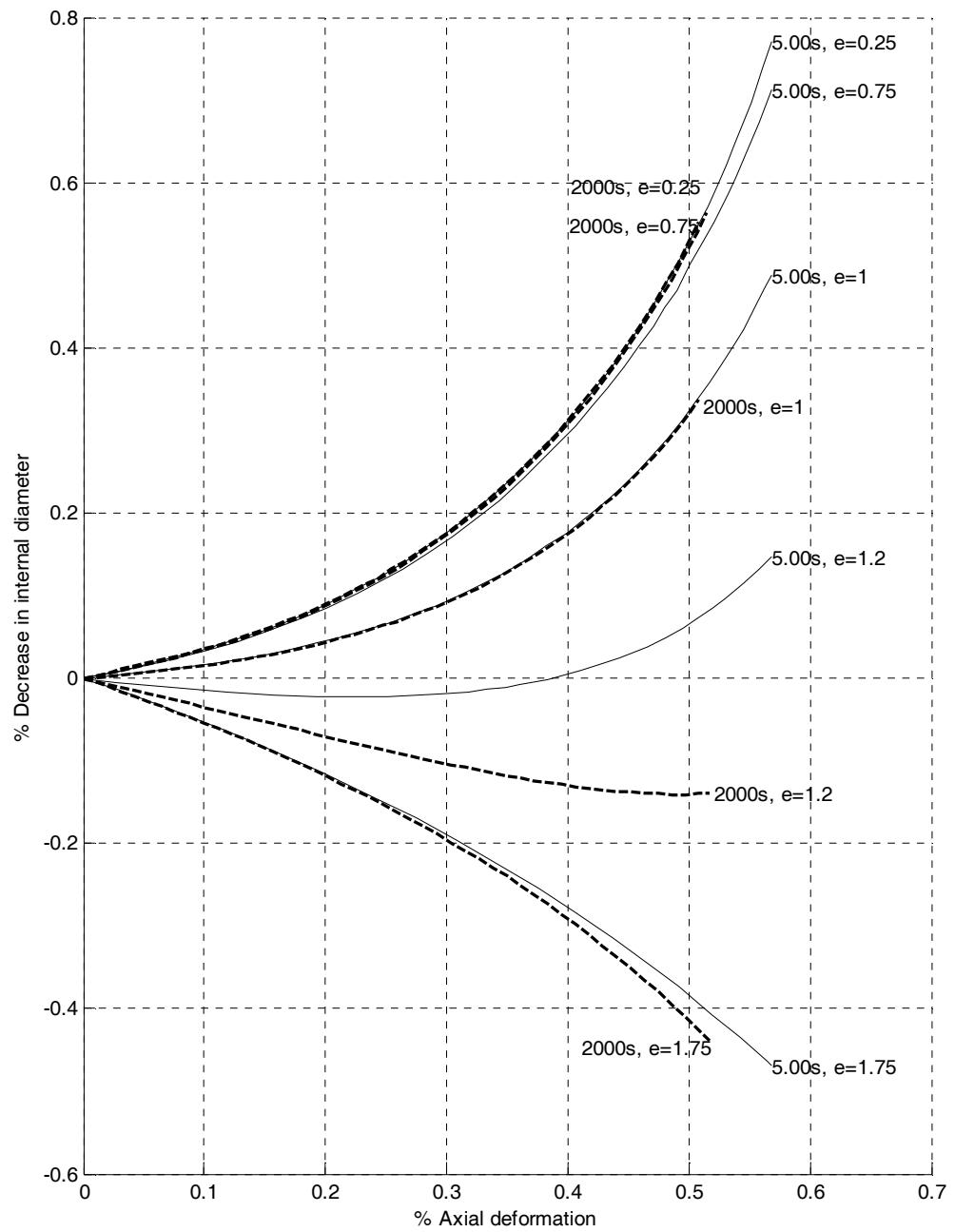
Figure 2. Dependence of the FCC on the exponent of the nonlinear form of the Navier law for $\eta = 10^9$ Pa·s. For each exponent the FCC for pressing times of 5 and 2000 s are presented.
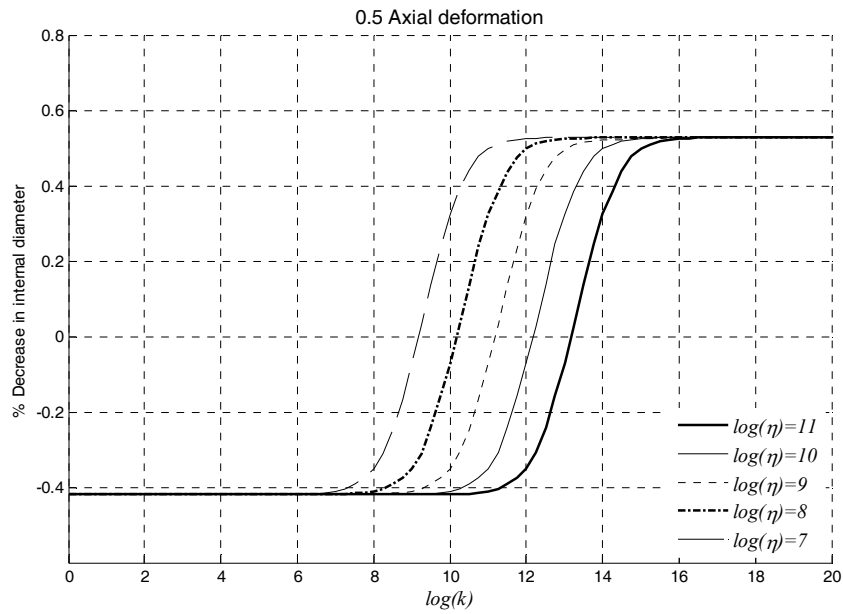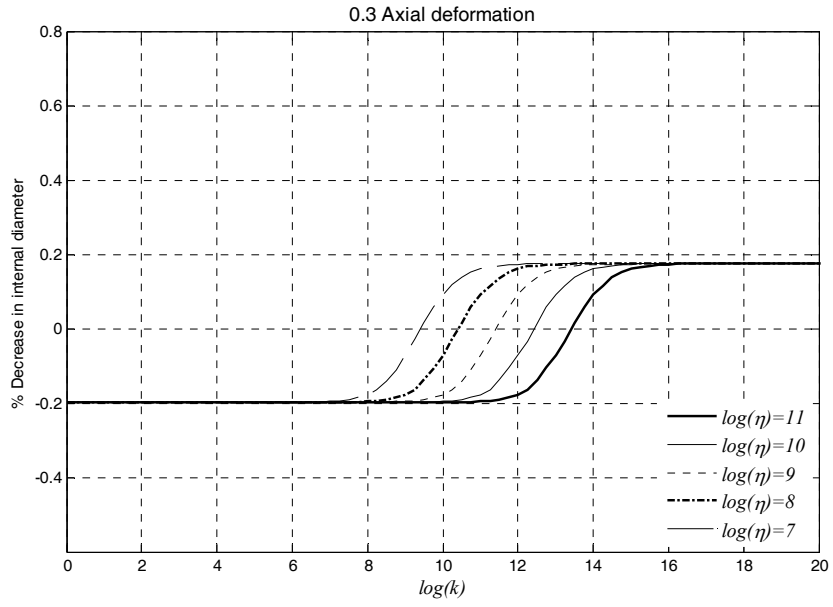
Figure 3. Percent decrease in internal diameter of the ring as a function of Log(k×m)/(Pa·s)) for Log(η/(Pa·s)) = 7, 8, 9, 10 and 11 for four different values of axial deformation.
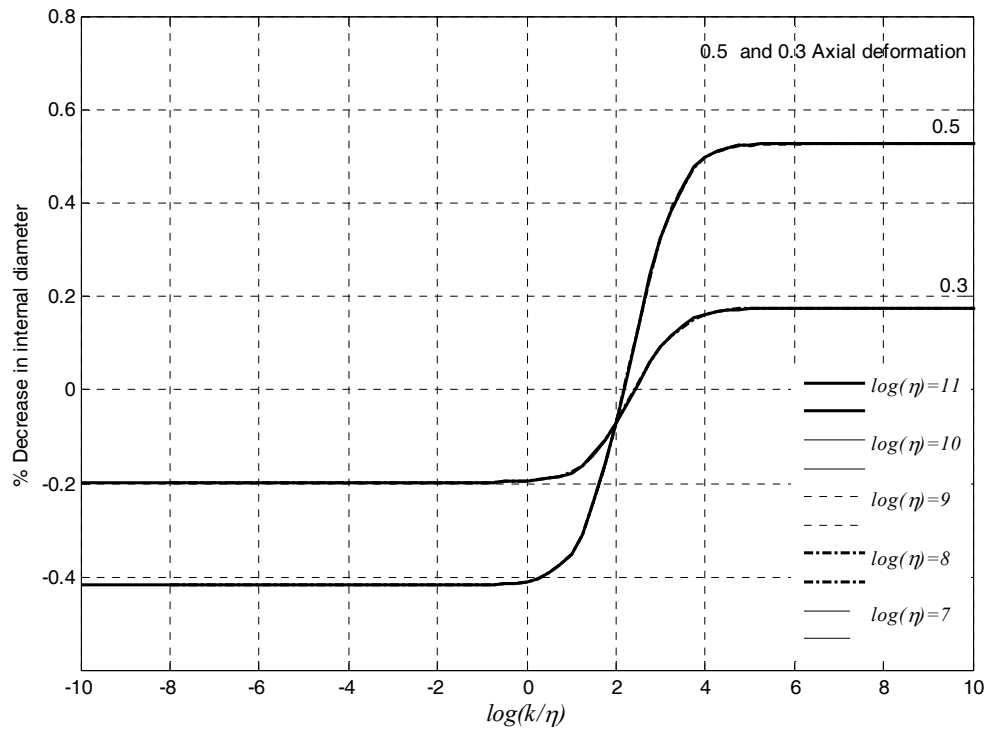
Figure 4. The two axial deformation cases from Figure 3 plotted using Log($k \times$m$/\eta$), which unifies the viscosity curves at each level of deformation.
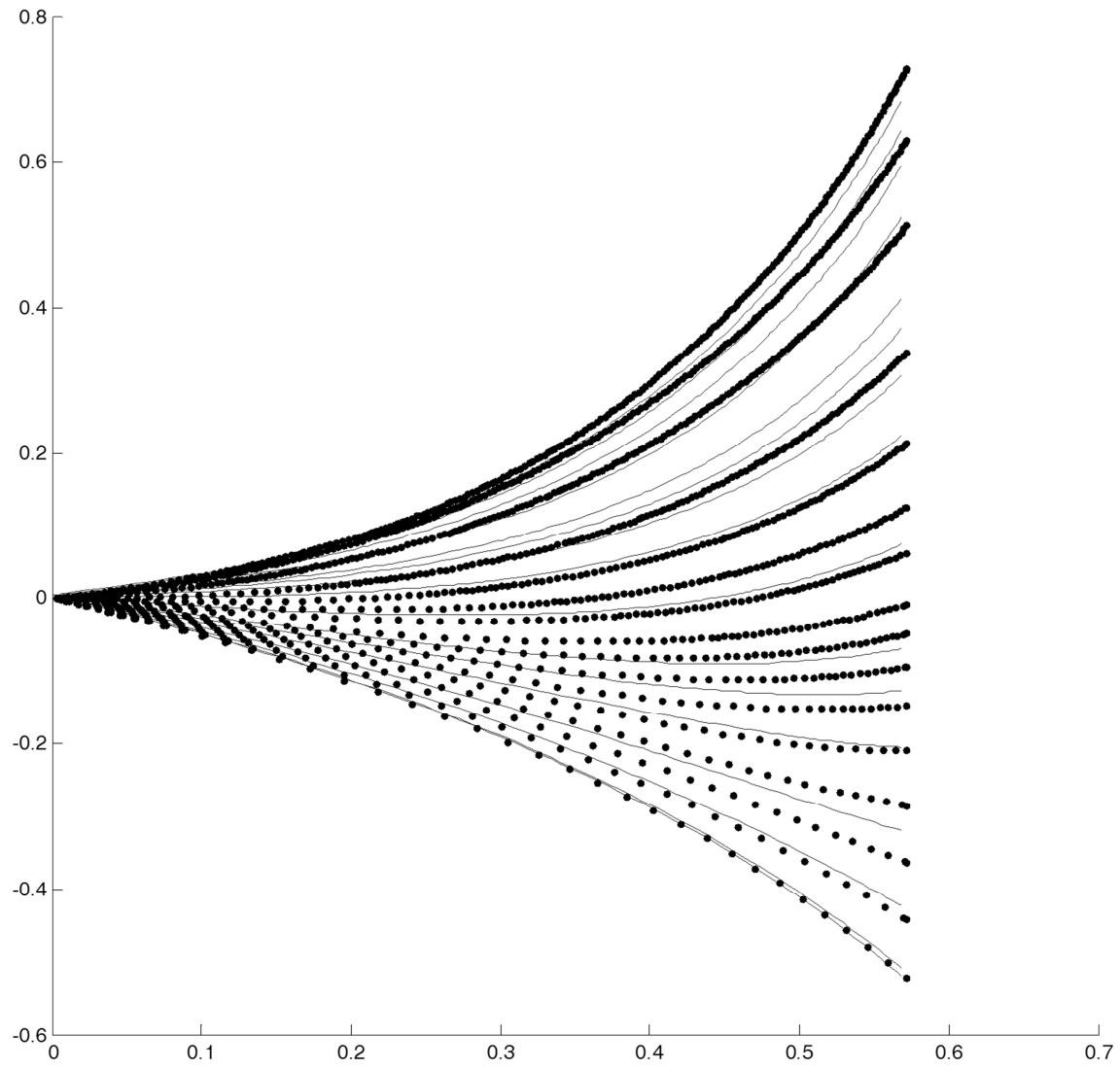
Figure 5. FCC using either the Navier model or the Coulomb model. See also Table 1.

Appendix D. Protective coatings
I. Luzinov and R. Burtovyy

In addition to the following report from the end of the third year, which was a final report for the topic of protective coatings, a journal paper draft has been prepared, which will soon be submitted, and is included is Appendix D1.

This report focuses on testing of uniformly deposited carbon coatings (CC) on actual glass samples, testing of the carbon coatings as release coatings for molds, feasibility of CC application for chalcogenide glass, feasibility studies of graphene oxide as a protective coating and evaluation of additional properties of CC. The major achievements are highlighted below.

At first, CVD-like uniformly deposited coating was tested for L-BAL35 and N-BK7 samples of cylindrical geometry with smooth top and bottom surfaces (**Section I**). The coating demonstrated excellent results with respect to minimization of adhesion/friction. The persistent issue of cracking of the coating was observed in this case. This issue is attributed to high cohesion inside the coating preventing its' adjustment to expending glass surface.

Secondly, our effort was directed toward reducing the cracking of the coating during the glass molding. Graphene oxide was tested as a possible candidate for a protective coating (**Section II**). Whereas it was able to reduced friction significantly the cracking issue was still present as indicated by analysis of the glass's surface after molding.

Then, trial molding experiments were performed using developed carbon coatings as release coatings deposited on the mold's surface (**Section III**). CVD-like deposited coating demonstrated the best results. Still, the coating was partially pilled off the mold's surface. It was related to additional stresses accumulated at the edges of the cylindrical sample. These stresses should be much smaller in case of actual glass pieces used in industrial molding process. Thus, it is feasible to use the coating for protecting the mold.

Next, polycarbonate was tested as a protective coating for chalcogenide glass (**Section IV**). It was shown to prevent direct glass-mold contact successfully. Because of soft/fluid nature of polycarbonate at the temperatures of molding no cracking issue was observed. Thus, polycarbonate and polycarbonate derived carbon materials can cover wide range of glasses used in molding process.

In additional, some fundamental properties and characteristics of the developed carbon coatings were studied (**Section V**). Namely, UV-Vis, IR and XPS spectra were collected and densities of some carbon coatings were determined.

The main direction of future development will be testing of the developed coating in actual glass molding process at a manufacture's facilities.

I.   Testing of uniformly deposited CC III (see previous report) on LBAL-35 and N-BK7 glasses

CC III was deposited following standard experimental procedure for CVD-like deposition process:

- the glass sample was positioned 3-5 mm above the surface covered with polycarbonate (PC) and placed in a quartz chamber;
- the chamber was heated up to 430-450 $^{\circ}$C in air at 10 $^{\circ}$Cmin^{-1};
- the deposition was carried out at 430-450 $^{\circ}$C for 1 hour;
- the chamber was removed from an oven and left to cool down.

The molding was performed at 570 $^{\circ}$C and 640 $^{\circ}$C for LBAL-35 and N-BK7 respectively. The results are presented in Figure 1 and Figure 2.
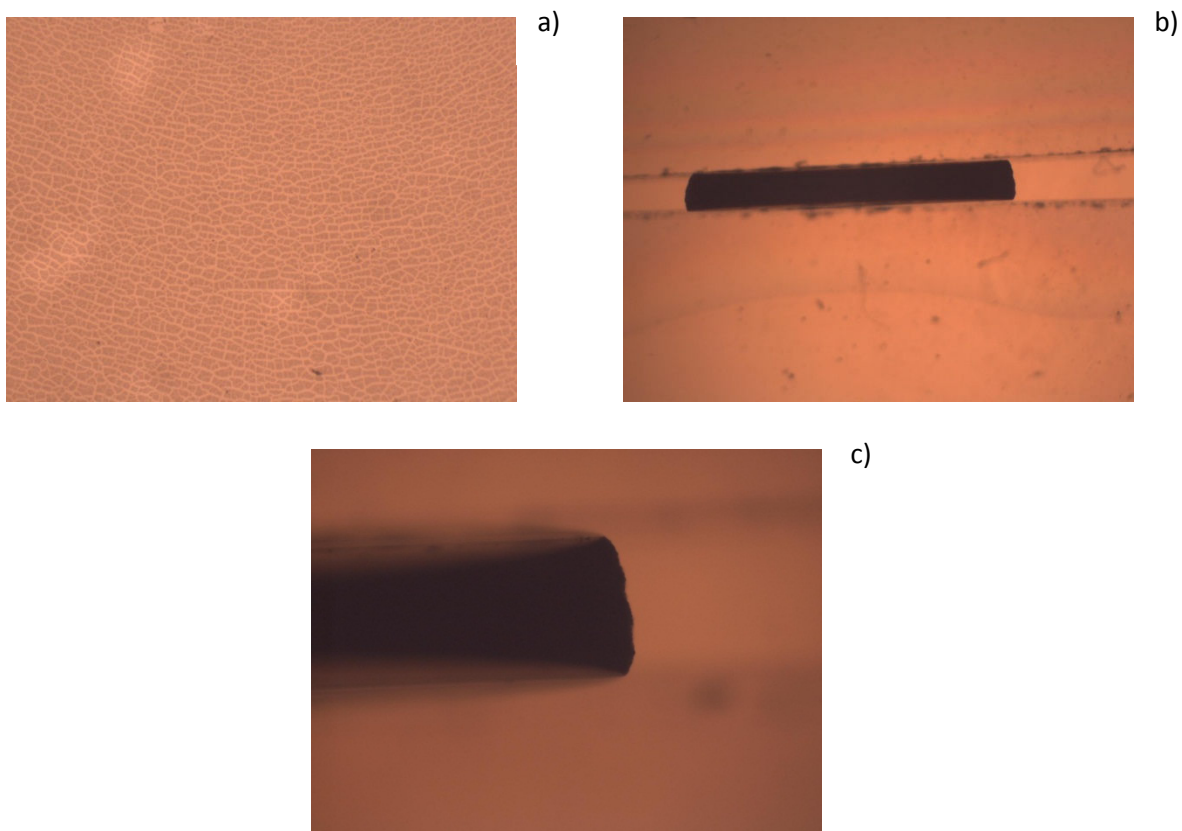
Figure 1. LBAl-35 glass with CC III after molding a) top view, b) side view and c) side view at higher magnification.
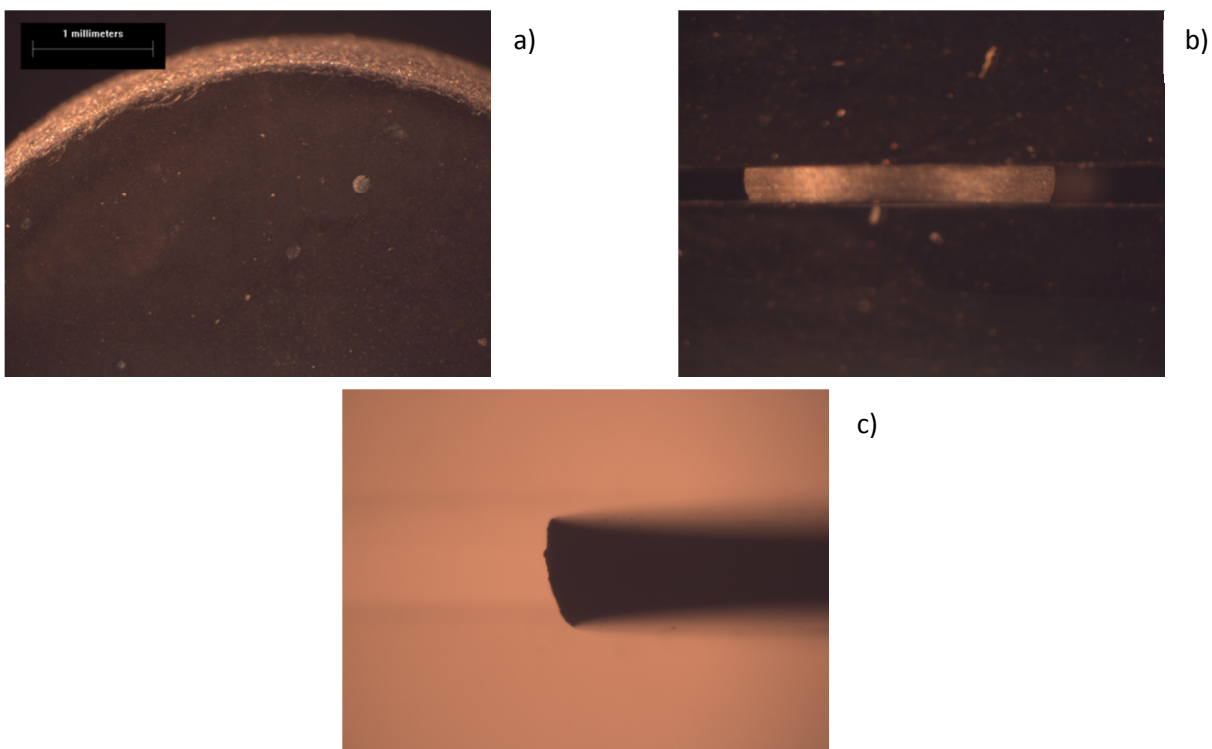
Figure 2. N-BK7 glass with CC III after molding a) top view, b) side view and c) side view at higher magnification.
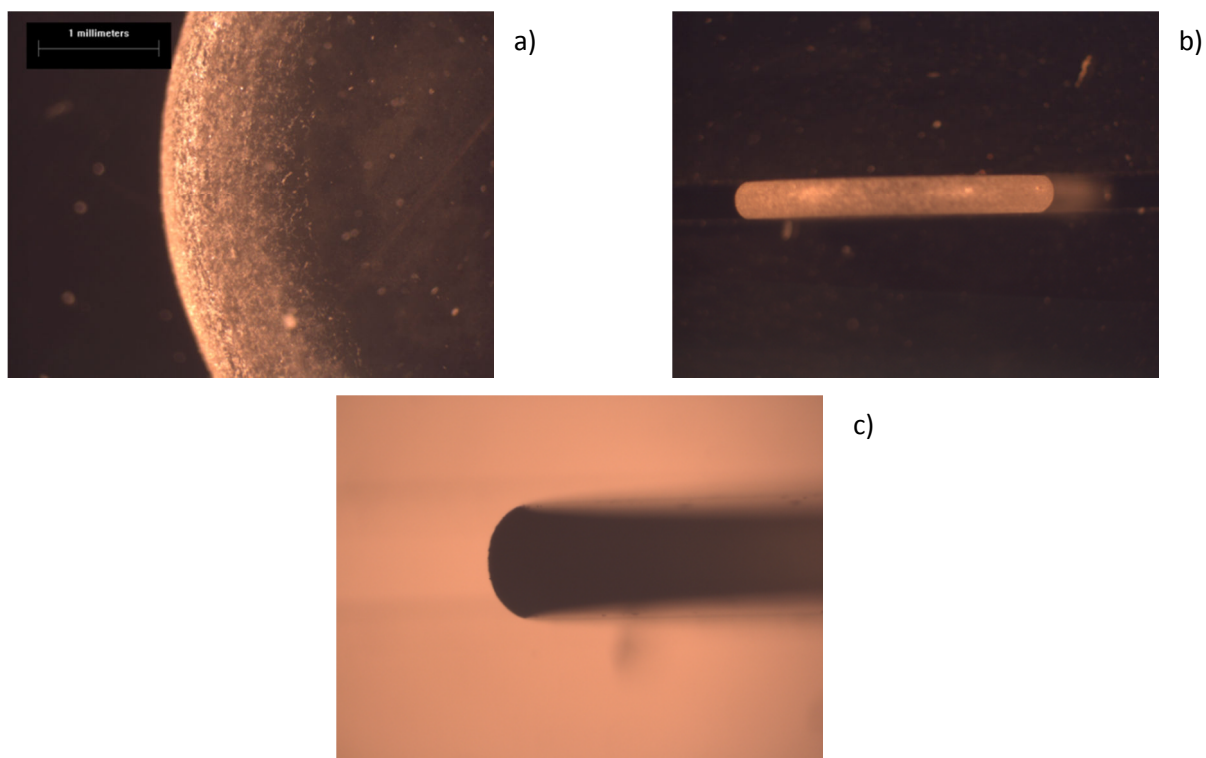
Figure 3. Original N-BK7 glass (without any coating) after molding a) top view, b) side view and c) side view at higher magnification.

For comparison the same images of original N-BK7 glass (without any coating) after molding are presented in Figure 3. The prominent difference of the coating's presence is visible clearly. Namely, friction is reduced to bare minimum (or virtually eliminated) as indicated by absence of an outer ring of rough surface (compare Figure 2a and 3a) as well as minimal bulging (compare Figure 1-2 b,c and 3b,c). The coating was very uniform and performed up to expectations. The significant internal coherency of the coating resulted in its' cracking upon expansion of the glass sample during the molding (Figure 1a for LBAL-35, identical surface was observed for N-BK7).

II.   Graphene oxide as a protective coating

In an attempt to overcome the cracking issue a graphene oxide (GO) was proposed as a protective coating. In essence, GO is oxidized graphene with various oxygen containing groups on the surface. It preserves a single-sheet structure of graphene and can be dispersed in water easily. According to an initial assumption the graphene sheets will have minimal internal friction and slide over each other under pressure during the molding (much like in a case of graphite). Since, it should prevent cracking of the coating as the coating will expend together with the glass.

The GO coating was prepared by direct deposition from 1 wt. % of GO suspension in water on one side of the glass sample (N-BK7). The thickness of the coating was varied by changing the amount of the drops deposited. For initial trial studies no thickness measurements were performed.

The results of the trial with GO are presented in Figure 4.
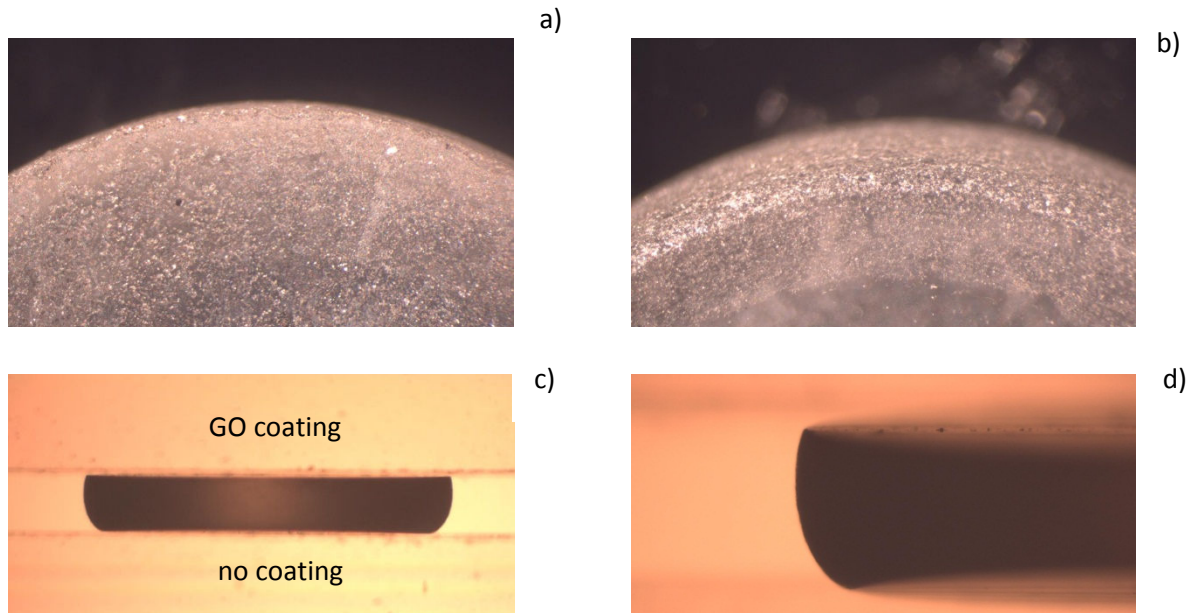
Figure 4. N-BK7 glass with thin GO coating after molding a) top view-coated side, b) top view-original side, c) side view and d) side view at higher magnification.

GO coating performed very well with respect to friction/adhesion (no outer rough ring and no bulging on the coating's side). But the same cracking issue was present, which manifested itself clearly in case of thicker GO coating (Figure 5).

Figure 4. N-BK7 glass with tick GO coating after.

.

III.   CC as a release coating for the mold

It was mentioned in the previous report that CC can be used on the mold substrate as release coatings based on its glass wettability properties. We performed several trial experiments with various CC deposited at different conditions. The mold was modified with CC deposited by spin-coating of PC (SCPC) and CVD-like process. Spin-coated PC was carbonized at 550 ^{o}C in nitrogen and CVD was performed at 450 ^{o}C in nitrogen as well. Only one piece of mold was coated, another one was kept in original unprotected condition. The results are depicted in Figure 5.
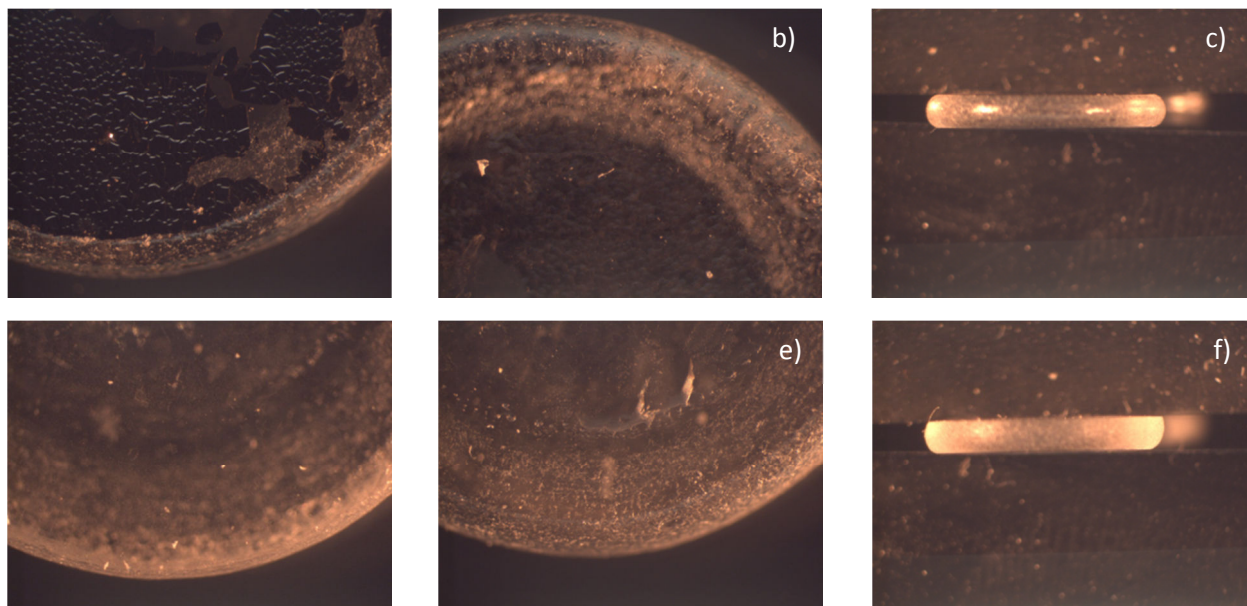
Figure 5. N-BK7 glass on the SCPC coated mold: a) top view-coating side, b) top view-original side, c) side view and CVD-coated mold: d) top view-coating side, e) top view-original side, f) side view (coating side on the top).

As it can be seen SCPC is not successful in minimizing adhesion/friction and large part of the coating is transferred from the mold to the glass. On contrary, CVD coating minimizes adhesion/friction. The surface quality of the coated mold piece demonstrates the difference between SCRC and CVD coatings (Figure 6).
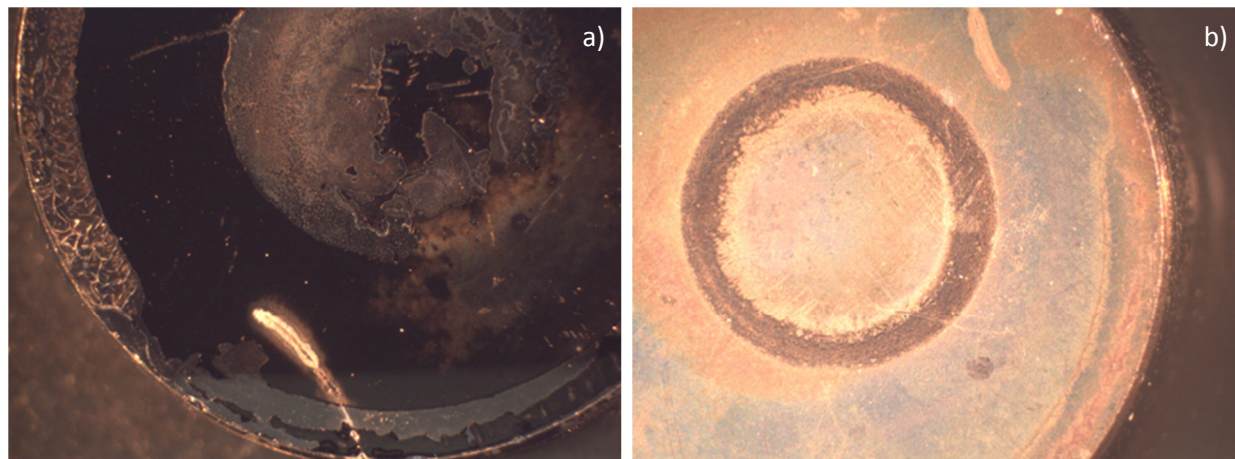
Figure 6. The mold substrate coated with a) SCRC and b) CVD-like coating.

Indeed, SCRC is almost delaminated at the place of direct contact between the glass and the mold. At the same time, delamination of CVD-coating is observed only around the perimeter of the glass sample. In former case the delamination process can be attributed to the poor mold-coating adhesion and rather strong glass-coating adhesion. In the later one the delamination might be caused by mechanical stressed accumulated at the edges of the glass sample.

IV.   Polycarbonate as a protective coating for chalcogenide glass

In general, chalcogenide glass is molded at temperatures much lower than oxide glasses. Thus, the carbon coatings cannot be created on the chalcogenide glass' surface from PC. But considering thermal properties of PC (Figure 7), the polymer itself can be used as a protective coating.
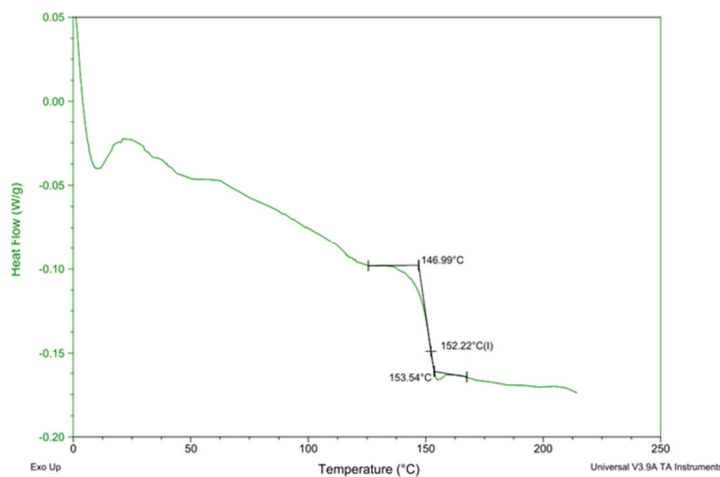
Figure 7. DSC scan of PC

PC has a glass transition temperature at 150 ^{o}C, melts at 270 ^{o}C and decomposes at 450 ^{o}C. Thus, in 150-450 ^{o}C temperature range it is soft and can deform under pressure during the molding process. In essence, soft liquid-like film of PC will prevent direct contact between a mold and glass. PC can be removed afterward by rinsing with an appropriate solvent.

Trial molding experiments were performed for $As_{30}Se_{70}$ glass at 157 ^{o}C. PC was deposited on the glass surface by drop casting from a solution in chloroform. For the trial no actions were undertaken to control thickness or uniformity of the PC film. The results are shown in Figure 8.
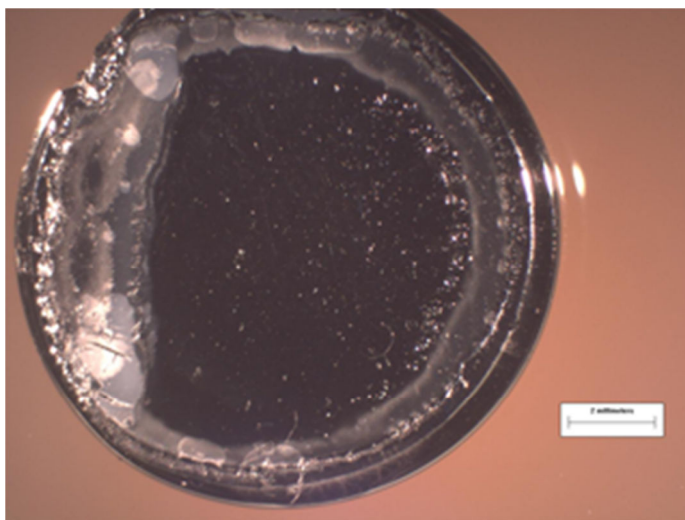
Figure 8. $As_{30}Se_{70}$ with PC coating on top after molding

As it can be seen PC layer expends together with expending glass sample shielding the glass from the mold.

V.   Properties of CC (IR, UV-Vis and XPS spectroscopy, density measurements

The thickness for UV-Vis spectroscopy was extended up to several microns (Figure 9).
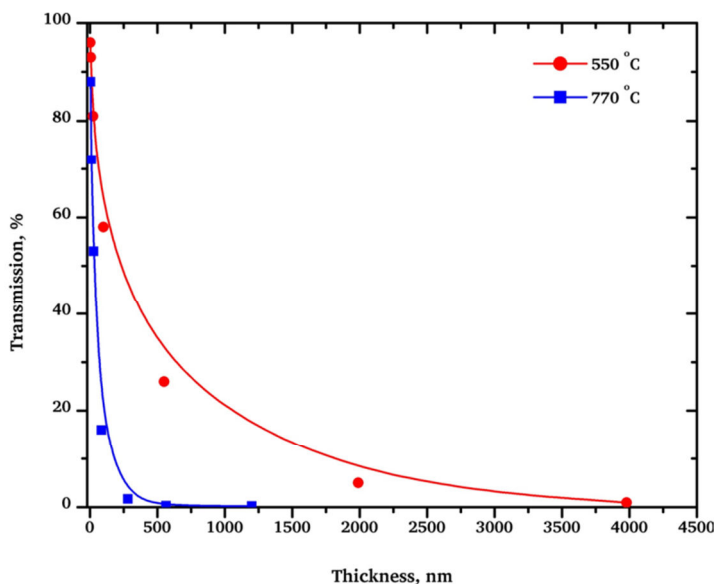
Figure 9. UV-Vis transmission of CC prepared at 550 ^{o}C and 770 ^{o}C (solid line is a guide)

For fully carbonized CC the transmission drops sharply with thickness and at 250 nm the coating is not transparent. On contrary, partially carbonized coating preserves its small but still noticeable transparency up to more than 1 μm of thickness.

IR spectra of the CC (Figure 10) confirm the coatings chemical nature. CC prepared at 550 ^{o}C is partially carbonized and, thus, still shows spectral lines corresponding to C-H, and C-C bonding. At the same time, fully carbonized sample (750 ^{o}C) does not show any identifiable lines.
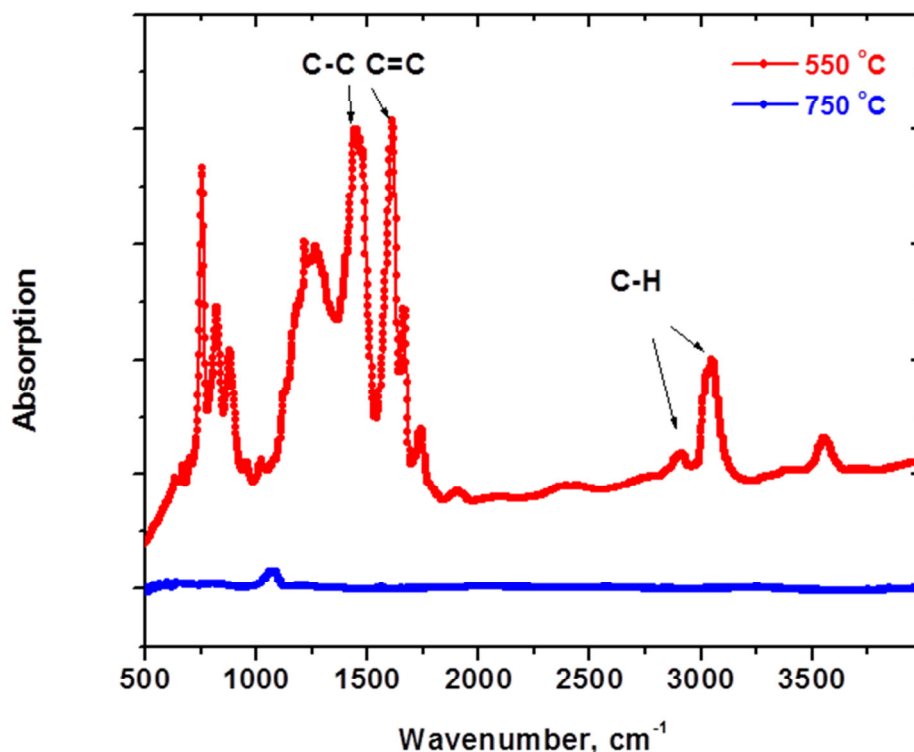
Figure 10. IR spectra of CC prepared at 550 ^{o}C and 750 ^{o}C.

Typical XPS spectra are presented in Figure 11. For coating were analyzed: 1) 550 ^{o}C, 2) 770 ^{o}C, 3) CVD at 550 ^{o}C, 4) CVD at 770 ^{o}C. All coatings are characterized by very similar spectra and contain up to 14 % of oxygen. It should be noticed that for coatings prepared at 770 ^{o}C the oxygen content is lower (estimated 7%). The high resolution spectra of carbon still have to be analyzed, but the preliminary conclusion is that all coatings are dominated by carbon with sp2 hybridization (similar to graphite). Accurate sp3:sp2 hybridization ratio still has to be determined.

Determination of the coatings' density is not a trivial matter considering their extremely small thickness. Following methodology was used to determine the density of two coatings (550 ^{o}C and 770 ^{o}C):

- PC was deposited on a silicon wafer's surface and its thickness was measured (by elipsometry);
- PC was carbonized using desired thermal protocol;
- final thickness of CC was measured (by AFM);
- the same thermal protocol was used to carbonized PC films inside TGA instrument;
- weight loss accompanied carbonization was obtained from TGA measurement;
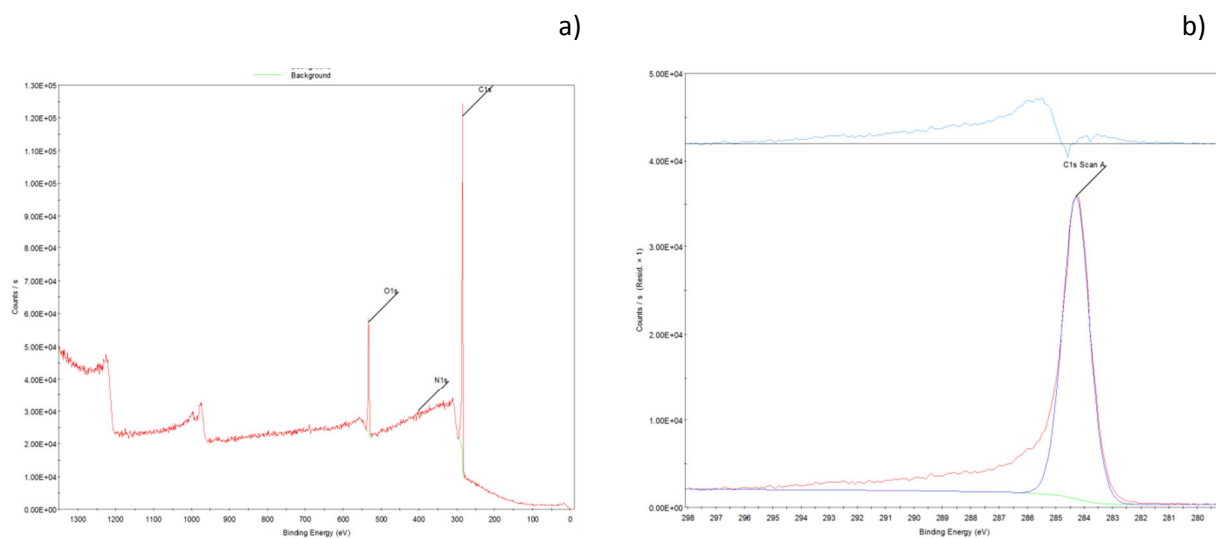- changes of volume (equal to changes of thickness), changes of films' weight as well as

118

Figure 11. Typical XPS spectra of CC coating a) overview scan and b) carbon high resolution scan.

density of pure PC (1.2 g*cm^{-3}) were utilized to calculate final density of CC.

The results are presented in Table 1.

Table 1. The results of the measurements of the density of CC

T$_{carb}$, °C	H$_{PC}$, nm	H$_{CC}$, nm	Residual weight, %	Density, g*cm^{-3}
550	252	37	20	1.7
770	256	20	17	2.6

The results presented in Table 1 confirm the nature of the particular CC (partially and fully carbonized polymer).

Appendix D1 (Paper DRAFT)
Carbon nanocoating via decomposition of poly(bis-phenol A carbonate)

R. Burtovyy[1], B. Gleason[1], I. Luzinov[1], K.C. Richardson[1]

[1]Department of Materials Science and Engineering, Clemson University, Clemson, SC 29634

Abstract

The article describes the preparation of different types of carbon nano-coating via decomposition of poly(bis-phenol A carbonate). The polycarbonate is characterized by apparent single-stage decomposition process yielding about 25 wt. % of carbonous material. Three distinct types of the coating can be prepared. C1 coating obtained at 550 ^{o}C is non-conductive and semi-transparent up to a micron thickness, whereas C2 coating (>550 ^{o}C) is conductive and virtually non-transparent and C3 – non-conductive with increased surface roughness, all coatings are amorphous. A practical utilization of lubricating and anti-adhesive action of carbon coating prepared via the polycarbonate decomposition is demonstrated for high temperature-high pressure precision glass molding process.

Keywords: polycarbonate, decomposition, carbon coatings.

Introduction

Carbonous materials and coatings have gained a widespread usage granting their excellent anti-adhesive and lubrication properties[1-3]. The majority of the coatings used is of a macro- or micro-size and sold as preformulated slurries/mixtures. Just recently nano-coatings have started finding their ways from a laboratory environment into practical usage areas. Their rather slow adaptation is not to the small extend reasoned by the methods used to prepare them[4,5]. Majority if not all of the standard ones require quit specific and costly equipment (plasma generation, vacuum, high energy beams etc), that is not always economically viable.

On contrary manufacturing of bulk carbon goods (carbon fibers) through thermal decomposition of polycarylonitrile (PAN) is going full steam. Surprisingly enough there is virtually no reports published on preparation of carbon nano-coatings via polymer decomposition process. One of the major obstacles in this case is a low yield of the final carbon material (PAN yields 50 % of carbon by weight). Amount most abundant polymers next in this respect is poly(bis-phenol A carbonate) (PC), which can produce about 25 wt. % of carbon material[6]. Up to date the decomposition process of PC has been almost exclusively considered from the point of view of the polymer's flame retardation properties[7-11] with emphasis put on its mechanism[12-18]. The only PC-carbon related publications are dedicated to preparation of bulk char/carbon samples[19-22] without real focus on obtained carbon properties.

Considering abundance of PC and utilization related problems for used products additional prospective usages of the polymer are more than desirable. Present article describes preparation of different types of carbonous coatings via thermal decomposition of PC. A practical implementation of the above mentioned method is exemplified for precision glass molding process.

Experimental

Materials

Poly(bis-phenol A carbonate) (PC) (M_w=60 kDa) purchased from Sigma-Aldrich was used as a primary material. Silicon wafers and quartz slides (Quartz Scientific Inc) were used as substrates for PC. NBK-7 glass samples (cylindrical samples 1 mm in height and diameter of 5 mm) were purchased from Newport Inc.

Procedures

Silicon wafer and quartz substrates were cleaned applying standard procedure for piranha treatment. PC was deposited on the substrate from the solution in chloroform by dip-coater able to operate at variable withdrawing speed. By adjusting withdrawing speed as well as using the solution of an appropriate concentration desired thickness of the PC film was obtained.

The thickness of the polymer films was measured by COMPEL automatic ellipsometer (InOmTech, Inc.) at a 70° angle of incidence and atomic force microscope (AFM). AFM thickness measurements as well as the films' morphology study were performed on Dimension 3100 microscope equipped with Nanoscope IIIa controller. The area of the film was scanned in Tapping Mode at 1Hz using NSC-16 (MikroMasch Inc) tip. Final thickness of the carbon coating was measured by AFM as well.

Carbonization of PC was carried out in ultrahigh pure nitrogen environment in a quartz tube. The samples were heated at 10 ^{o}Cmin^{-1} up to desired temperature and held there for 1 hour.

Thermal gravimetric analysis (TGA), infared (IR) and UV-Vis spectroscopy measurements were carried out on TA Instruments Q5000 TGA, Thermo 6700 FTIR and Shimadzu 3101-PC UV-Vis-NIR Spectrometer repectively. High resolution TEM (HD-9500, Hitachi Inc) was used for evaluation of crystal structure of the obtained carbon nanocoatings.

NBK-7 glass samples were pressed on precision glass molding machine at 640 ^{o}C temperature.

Due to the brittleness of the coatings electrical properties results were obtained by gluing two stripes of conductive glue on opposite side of the coating deposited on a quartz slide and measuring resistivity. The conductivity was calculated based on the measured value and length of the stripes and thickness of the coating.

Results and discussion

In order to evaluate the thermal stability of PC in different environments series of TGA measurements were performed (Figure 1).
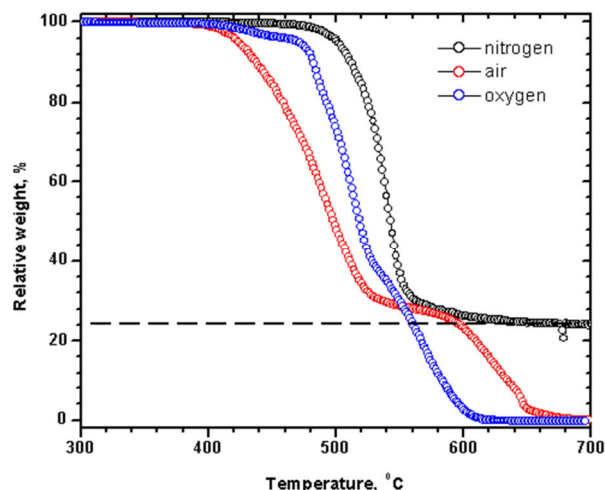
Figure 1.TGA graphs for PC decomposition in different environments

The results reveal single step decomposition process in inert (nitrogen) environment with about 500 ^{o}C on-set temperature and the majority of PC material already decomposed at 550 ^{o}C. Slow decomposition process continuous up to higher temperatures of 700 ^{o}C resulting in about 25 % of black residual material (presumably carbon). Surprisingly enough the on-set decomposition temperature can be lowered by 100 ^{o}C when the process is performed in air flow. Approximately the same amount of the residual material is left at 600 ^{o}C before it is burned completely at higher temperatures. The lower on-set temperature in air offers a possibility to achieve the same final product result at lower temperature and in open air environment. This particular feature is very desirable for industrial purposes as it will be demonstrated latter in the article for glass molding process. Indeed, when PC decomposed in TGA furnace using the protocol incorporating heating to 450 ^{o}C following by isothermal step for 1 hour at this temperature the same results can be achieved (Figure 2).
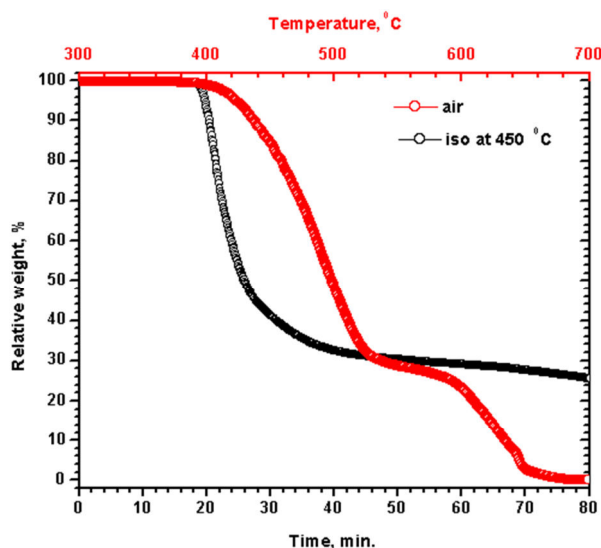
Considering the two stage decomposition processes in nitrogen (fast decomposition 520-560 ^{o}C, slow decomposition above 560 ^{o}C) two different products are expected to be obtained when the process is quenched in corresponding temperature regions. Thus, the PC carbonization in the oven followed two different protocols: 1- heat up at 10 ^{o}Cmin^{-1} to 550 ^{o}C and 1 hour isothermal hold, 2- heat up at 10 ^{o}Cmin^{-1} to 750 ^{o}C and 1 hour isothermal hold.

In fact, quite significant difference manifested itself in resulting thicknesses of carbon layers. Namely, for protocol 1 the final product thickness as measured by AFM was about 15 % of the initial thickness of PC, whereas, it was about 8 % for protocol 2. The thin films of PC decomposed in TGA equipment using the same protocols resulted in 21 wt. % and 17wt. % of residual carbon respectively. Using above mentioned results and density of the original PC (1.2 gcm^{-3}) it is possible to estimate density of both materials, which yields 1.7 gcm^{-3} and 2.6 gcm^{-3} for 550 ^{o}C (C1) and 750 ^{o}C (C2) carbon respectively. It is evident, that the materials obtained should be of completely different in nature.

The difference is not observed in structure of the materials. Both C1 and C2 were proven to be amorphous as evidenced by TEM high resolution images (Figure 3).
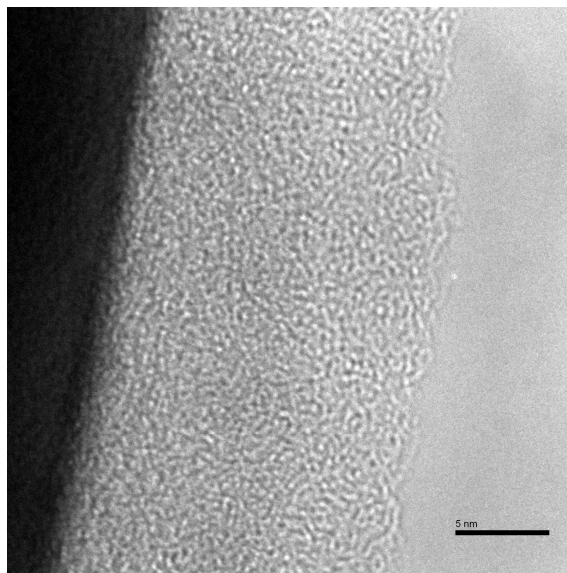

Figure 3. TEM image of C1 coating (C2 is the same).

The same properties were observed with respect to surface morphology of the obtained nanofilms as determined by AFM (Figure 4). The two protocols produced smooth homogeneous surface with the roughness value of 0.2 nm.
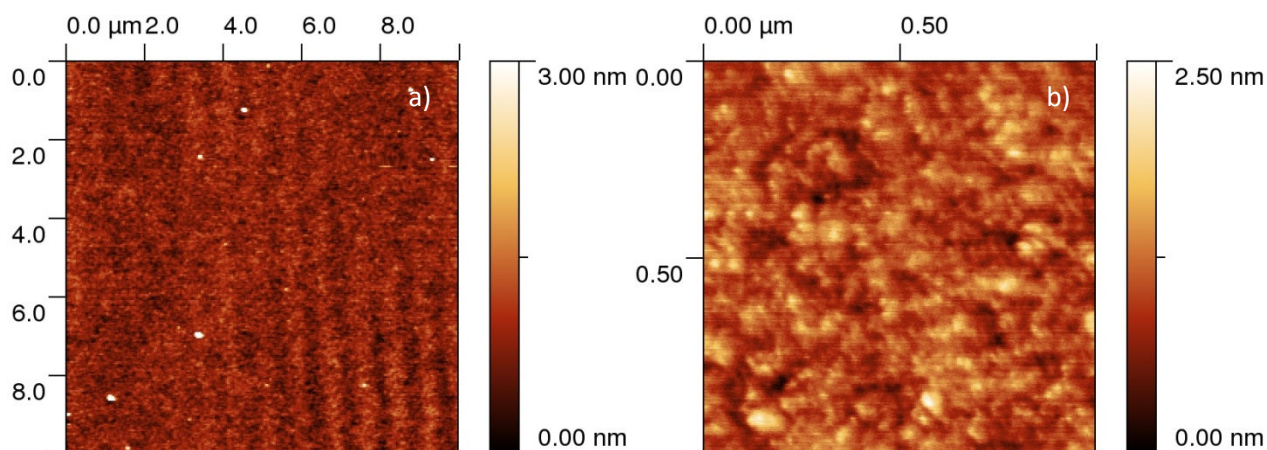
Figure 4. AFM images of C1 coatin (C2 is the same).

However, the sticking difference was observed for spectroscopic results. FTR-IR as well as UV-Vis spectra demonstrate a sharp contrast between two films (Figure 5).
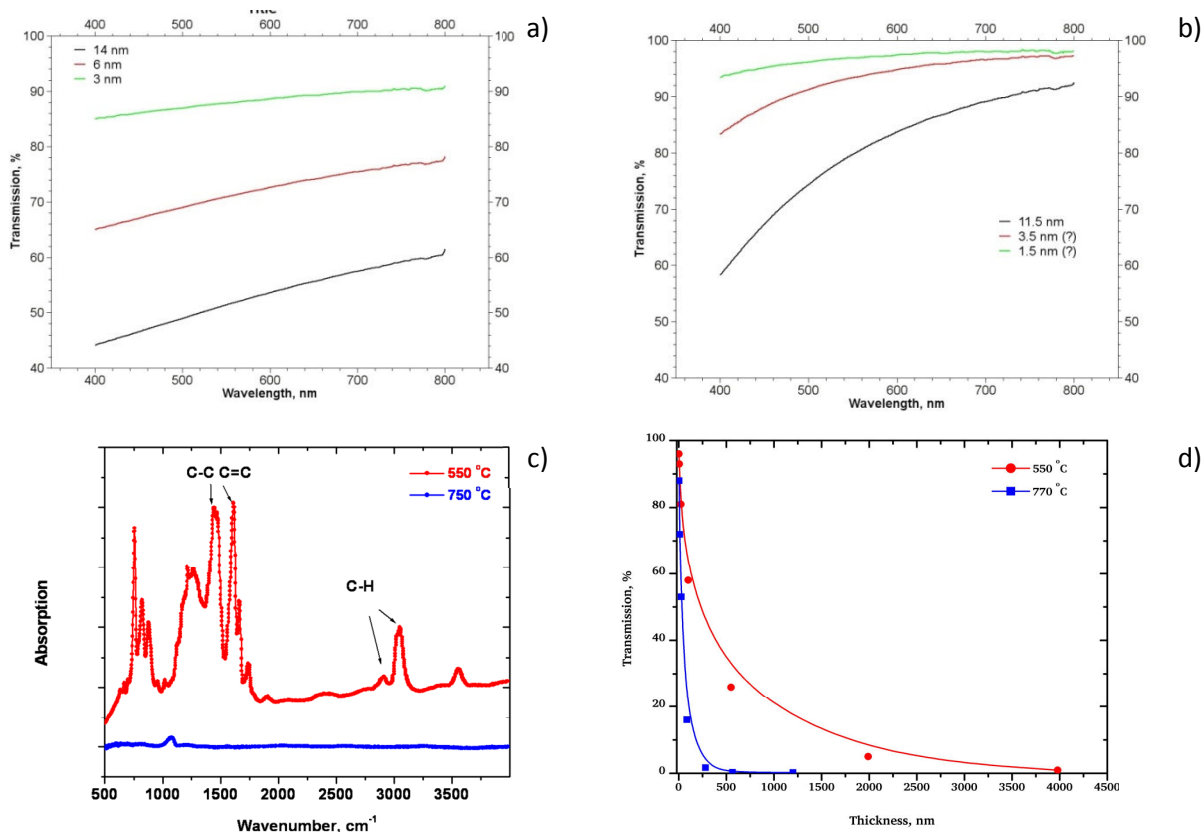

Figure 5. UV-VIS spectra for a) C1 and b) C2 coatings, c) IR spectra and d) average transmission in UV-Vis region

As the IR spectra suggest C1 is a partially decomposed polymer with presumably quite significant content of hydrogen. At the same time C2 can be assumed to be amorphous carbon

124

which can be proved by virtually non-existent IR spectrum as well as high density of the material. Transmission data back this statement. C1 material is transparent in visible region up at least 1 μm thickness. At the same time the transmission drops sharply for C2 and is already very low at about 100 nm thickness indicating high density and possibly conductive material.

The last characteristic of C2 was confirmed by electrical conductivity measurements. C1 materials was found to be insulator while C2 can conduct electricity with resistivity value of about $1*10^{-3}$ Ωm, which very close to the values observed for conductive amorphous carbon thin films prepared by different methods[23].

PC was found to be very versatile material serving as a source for preparation of carbon thin film. In fact, third type of the material (C3) can be obtained by decomposition of the polymer. In this particular case C3 is deposited on the objects situated above the PC film during its decomposition at high temperatures. The way C3 is produced resembles chemical vapor deposition (CVD) process. The resulting remarkable advantage is the ability to obtain thin uniform C3 nanofilms on the objects of complex geometry (like glass molding performs etc.) in one simple step.

Granting the small amount of the substance that can be deposited determination of its properties is a challenging task. It can be stated with confidence that the material is dielectric and the surface morphology is different from the smooth one of C1 and C2 (Figure 6).
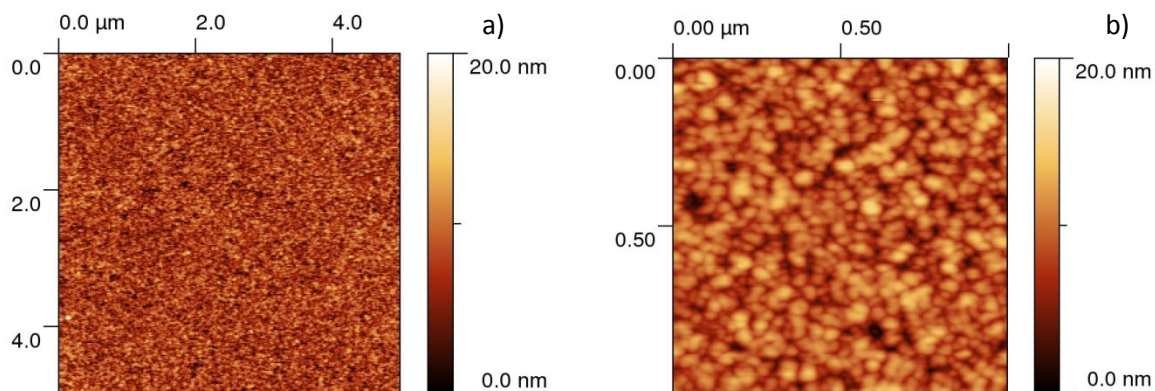

Figure 6. AFM images of C3 coating.

The surface roughness was about 2 nm. Taking into account the AFM images it might be assumed that C3 consists of spherical particles.

In order to demonstrate practical applicability of the nanofilms pressing of the NBK-7 glass samples was performed. Original glass samples (without any coating) and coated with C1 and C3. Due to the fact that temperature to obtain C2 coating is higher than the softening temperature of the glass the coating was not used in the applicability trials. We departed from standard mold protecting paradigm (coating is deposited on the mold surface) and coated the glass performs themselves.

The effectiveness of the coating in glass molding process is determined by its ability to lower friction between glass and a mold. The friction can be assessed qualitatively by observing bulging of the glass (curvature of the side surface). More bulging (larger curvature) indicates higher friction between the surfaces. Both coatings demonstrated identical excellent performance (Figure 7).
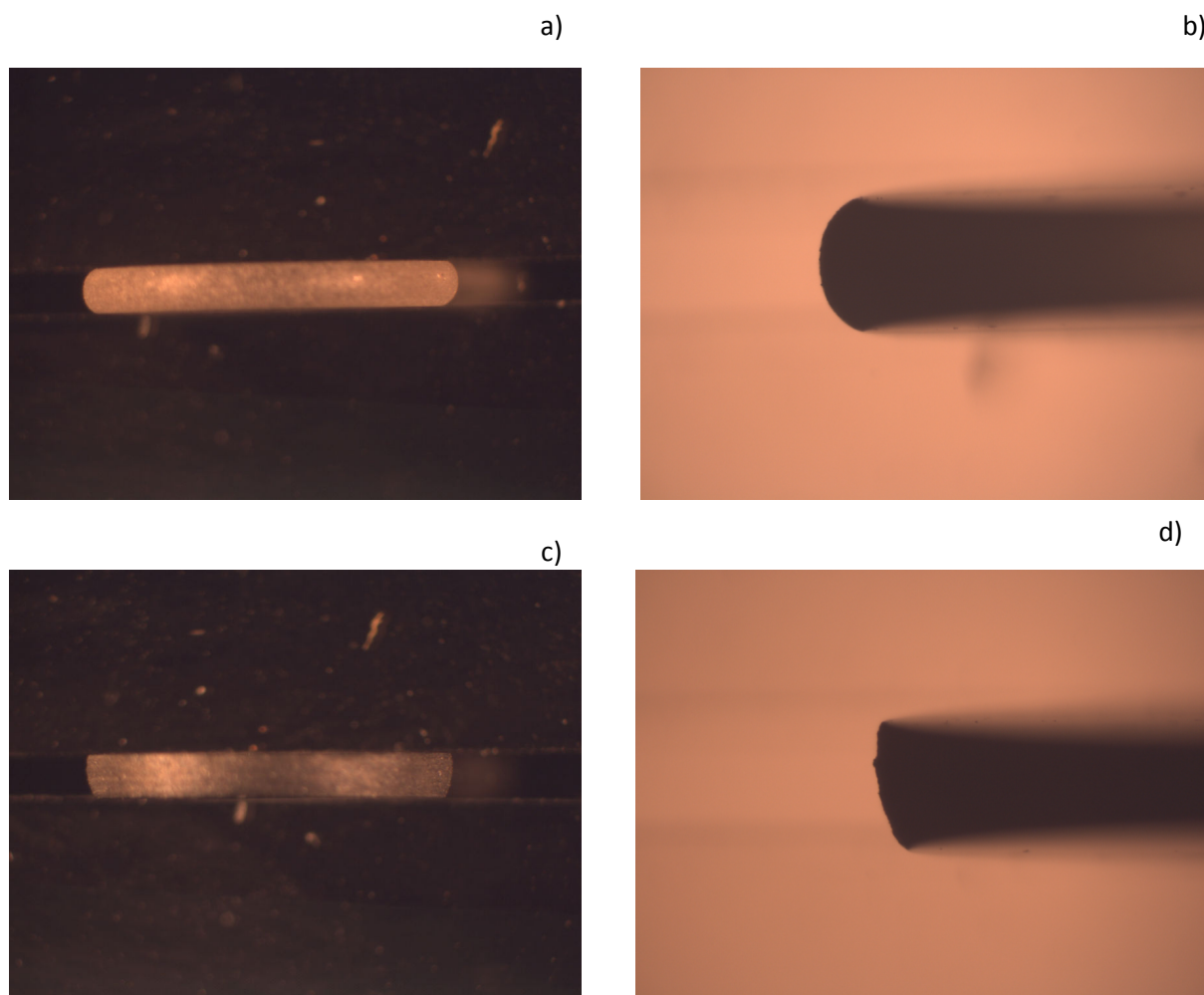
Figure 7. Optical images of a, b) bare and c), d) coated glass samples after molding.

It should be noted that the bulging is extremely small in case of coated samples comparing to the uncoated sample demonstration an excellent lubrication properties of the coating.

Conclusions

Polycarbonate was found to be a versatile material for preparation of different types of carbon coatings. Depending on final decomposition temperature (coatings C1 and C2) and methodology of preparation (coating C3) the resulting coating can contain hydrogen or be of pure carbon, conductive or insulating, smooth or posses certain roughness, transparent or non-transparent for visible light. Such variation in properties originated from a single polymeric material creates opportunities for its practical application that was readily demonstrated for precision glass molding process.

References

(1)   Camino, D.; Jones, A. H. S.; Mercs, D.; Teer, D. G. *Vacuum* **1999**, *52*, 125-131.

(2)   Roy, R. K.; Lee, K.-R. *Journal of Biomedical Materials Research Part B: Applied Biomaterials* **2007**, *83B*, 72-84.

(3)   Lettington, A. H. *Carbon* **1998**, *36*, 555-560.

(4)   Richter, F.; Bewilogua, K.; Kupfer, H.; Mühling, I.; Rau, B.; Rother, B.; Schumacher, D. *Thin Solid Films* **1992**, *212*, 245-250.

(5)   Bhushan, B. In *Springer Handbook of Nanotechnology*; 2 ed.; Bhushan, B., Ed.; Springer Berlin Heidelberg: New York, 2007, p 1339-1378.

(6)   Li, X.-G.; Huang, M.-R. *Polym. Int.* **1999**, *48*, 387-391.

(7)   Bozi, J.; Czegeny, Z.; Meszaros, E.; Blazso, M. *J. Anal. Appl. Pyrolysis* **2007**, *79*, 337-345.

(8)   Karrasch, A.; Wawrzyn, E.; Schartel, B.; Jaeger, C. *Polym. Degrad. Stab.*, *95*, 2534-2540.

(9)   Montaudo, G.; Carroccio, S.; Puglisi, C. *J. Anal. Appl. Pyrolysis* **2002**, *64*, 229-247.

(10)   Pikacz, E.; Seefeldt, H.; Schartel, B.; Braun, U.; Karrasch, A.; Jaeger, C. *Proc. Annu. Conf. Recent Adv. Flame Retard. Polym. Mater.* **2009**, *20th*, 243-253.

(11)   Wang, J.; Xin, Z. *Front. Chem. Eng. China* **2009**, *3*, 167-171.

(12)   Arulmozhiraja, S.; Coote, M. L.; Kitahara, Y.; Juhasz, M.; Fujii, T. *J. Phys. Chem. A*, *115*, 4874-4881.

(13)   Montaudo, G.; Puglisi, C. *Polym. Degrad. Stab.* **1992**, *37*, 91-6.

(14)   Onbattuvelli, V. P.; Rochefort, W. E.; Simonsen, J.; Park, S.-J.; German, R. M.; Atre, S. V. *J. Appl. Polym. Sci.*, *118*, 3602-3611.

(15)   Puglisi, C.; Samperi, F.; Carroccio, S.; Montaudo, G. *Polym. Prepr. (Am. Chem. Soc., Div. Polym. Chem.)* **2000**, *41*, 680-681.

(16)   Erickson, K. L. *Proc. NATAS Annu. Conf. Therm. Anal. Appl.* **2006**, *34th*, 049.23.844/1-049.23.844/12.

(17)   Davis, A.; Golden, J. H. *J. Chem. Soc. B* **1968**, 45-7.

(18)   McNeill, I. C.; Rincon, A. *Polym. Degrad. Stab.* **1993**, *39*, 13-19.

(19)   Hilado, C. J.; Casey, C. J. *J. Fire Flammability* **1979**, *10*, 227-39.

(20)   Politou, A. S.; Morterra, C.; Low, M. J. D. *Carbon* **1990**, *28*, 529-38.

(21)   Mendez-Linan, L.; Lopez-Garzon, F. J.; Domingo-Garcia, M.; Perez-Mendoza, M. *Energy Fuels*, *24*, 3394-3400.

(22)   Hilado, C. J.; Casey, C. J. *J. Fire Flammability* **1979**, *10*, 140-67.

(23)   Rebollo-Plata, B. L.-M., R. ; Palomino-Merino, R. ; Davila-Pintle, J. A. ; Portillo-Moreno, O. ; Zelaya-Angel, O. ; Jimenez-Sandoval, S. *Advances in Technology of Materials and Materials Processing* **2005**, *7*, 97-100.